UCLouvain

FACULTE DES SCIENCES

Faculté des sciences

Variability of the Arctic sea ice volume at the regional scale: a study based on the PIOMAS-20C reanalysis

Author: **Christophe MAIER**
Supervisors: **Thierry FICHEFET, Leandro PONSONI**
Readers: **François MASSONNET, Francesco RAGONE**
Academic year 2022–2023
Master [120] en sciences physiques

Acknowledgements

I would like to thank Thierry Fichefet and Leandro Ponsoni for their advices on structuring the thesis and help on establishing an appropriate methodology for the model validation and analysis. I would also like to thank them for having taken the time to review various versions of this paper and for their suggestions on some of the articles used throughout this thesis. Finally, I thank Guillian Van Achter for his help on the choice of the wavelet function utilised in the wavelet analysis.

Abstract

An analysis of the regional impact of the Arctic Oscillation (AO), North Atlantic Oscillation (NAO), North Pacific Oscillation (NPO), Pacific Decadal Oscillation (PDO) and Atlantic Multidecadal Oscillation (AMO) on the Arctic sea ice volume (SIV) variability is performed using the reconstructed data of the PIOMAS-20C reanalysis. Our results confirm the findings of previous studies and highlight the importance of the AO and NAO in driving the SIV variability across the Arctic Ocean through their influence on the sea ice motion (SIM), surface air temperature (SAT) and sea surface temperature (SST) spatio-temporal distributions generated by AO/NAO-induced surface wind shifts. A thermodynamical influence of the AO also takes place in the Bering Sea, Sea of Okhotsk, Baffin Bay, Labrador Sea and Barents Sea, as a result of the significant wind speed changes leading to sensible surface heat fluxes (SSHF) and atmospheric heat transport alterations over these regions. The NAO is found to produce prominent thermodynamical effects in the Baffin Bay, Labrador Sea and Barents Sea through the same mechanisms, although its influence over the North Pacific Ocean is not as significant. Prevalent dynamic impacts related to the NPO are noticed in the Artic Ocean, with the footprint of the NPO being especially recognisable in the temporal SIV variability of the Chukchi Sea. While dynamic impacts driven by the PDO are observed in the Arctic Ocean, the main impact of this mode of variability (MOV) is felt thermodynamically in the Bering Sea. Finally, the AMO is shown to induce important changes in the Baffin Bay, Labrador Sea and Hudson Bay SIV through its important relationship with the SATs and SSTs in these regions.

Contents

1 Introduction **1**
- 1.1 **Sea ice variability** . . . 1
- 1.2 **Modes of variability** . . . 2
- 1.3 **Current understanding of the impacts of the AO, NAO, NPO, PDO and AMO** . 2
  - 1.3.1 **Arctic Oscillation and North Atlantic Oscillation** . . . 2
  - 1.3.2 **North Pacific Oscillation and Pacific Decadal Oscillation** . . . 3
  - 1.3.3 **Atlantic Multidecadal Oscillation** . . . 4
- 1.4 **Impacts of the sea ice on the climate system** . . . 4
- 1.5 **Objectives** . . . 5

2 Data description and validation **7**
- 2.1 **Descriptions of the reanalyses** . . . 7
  - 2.1.1 **PIOMAS-20C reanalysis** . . . 7
  - 2.1.2 **ERA-20C reanalysis** . . . 8
- 2.2 **PIOMAS-20C SIV data validation** . . . 9
  - 2.2.1 **Sea ice concentration** . . . 9
  - 2.2.2 **Sea ice area** . . . 9
  - 2.2.3 **Sea ice thickness** . . . 15

3 Methodology **17**
- 3.1 **ERA-20C and PIOMAS-20C datasets** . . . 17
- 3.2 **Data pre-processing** . . . 17
- 3.3 **Interpolation of the data, computation of the sea ice motion divergence and surface pressure gradients** . . . 19
- 3.4 **Empirical orthogonal functions** . . . 20
- 3.5 **Linear correlations** . . . 21
- 3.6 **Wavelet analysis** . . . 21
- 3.7 **Definitions of the indices** . . . 24

4 Results and discussion **25**
- 4.1 **Spatial analysis** . . . 25
  - 4.1.1 **Arctic Oscillation and North Atlantic Oscillation** . . . 25
  - 4.1.2 **North Pacific Oscillation and Pacific Decadal Oscillation** . . . 33
  - 4.1.3 **Atlantic Multidecadal Oscillation** . . . 43
- 4.2 **Temporal analysis** . . . 49
  - 4.2.1 **Arctic Oscillation and North Atlantic Oscillation** . . . 49
  - 4.2.2 **North Pacific Oscillation and Pacific Decadal Oscillation** . . . 54
  - 4.2.3 **Atlantic Multidecadal Oscillation** . . . 55
  - 4.2.4 **Lag-tests** . . . 56

5 Conclusions **61**

A Supplementary materials **68**

Chapter 1

Introduction

Sea ice is one of the many types of ice formations composing the cryosphere. It is defined as the ice resulting from the freezing of sea water and covers parts of the oceans in the polar regions. As a result of its impacts on the climate system, this ice formation is widely studied. Numerous papers have already analysed past reconstructed data to improve our understanding of the driving mechanisms leading to its variability, while others sought to uncover its influence on the climate system. Nevertheless, our knowledge of the topic is still incomplete, and more research is required, especially since our models continuously improve, and therefore the quality of the data employed as well. This thesis refines our comprehension of the naturally-induced changes in the Arctic sea ice volume (SIV), by analysing the regional impacts of different modes of variability (MOVs) such as the Arctic Oscillation (AO), North Atlantic Oscillation (NAO), North Pacific Oscillation (NPO), Pacific Decadal Oscillation (PDO) and Atlantic Multidecadal Oscillation (AMO).

1.1 Sea ice variability

The SIV depends on the sea ice thickness (SIT) and sea ice concentration (SIC). For this reason, variations in any of these two quantities lead to a change in the SIV. Such fluctuations continuously occur, and are caused by thermodynamic and dynamic processes. Thermodynamics-induced shifts in the SIT and SIC are for the most part driven by the surface air temperature (SAT) and sea surface temperature (SST). The influence of the SAT and SST is mostly straightforward, with positive SAT and SST anomalies leading to a decrease in the SIV. On the other hand, dynamic processes represented by the sea ice motion (SIM) are largely controlled by the atmospheric winds. The divergence and convergence of SIM affect the SIT, SIC and SAT [Rigor et al., 2002]. A convergence of SIM forces various packs of ice onto each other through important pressure constraints, consequently resulting in sea ice rubble fields, hummocks or ridges [Morales et al., 1997]. These ice formations are associated with a greater SIT and further intensify the isolation of the ocean from the atmosphere. As a consequence, the SAT decreases due to the lower ocean surface heat release, but the amount of radiation received by the ocean is reduced as well. Rather, a divergent SIM results in leads and polynyas, through the breaking up of the ice driven by the atmospheric forcing [Morales et al., 1997]. These leads and polynyas may then become factories for the production of new young thin ice, that is then sent into the rest of the ocean, thus promoting a widespread SIV decline. On top of this, the formation of this new ice releases latent heat into the atmosphere, and therefore, combined with the increased heat release from the ocean, an SAT increase is usually observed over regions associated with an SIM divergence. This heat release effect can persist even through the following seasons, and as a result the melting season can be extended over these regions [Rigor et al., 2002].

The underlying mechanisms leading to these thermodynamic and dynamic processes are of anthropogenic or natural origin. The human-induced impacts on the Arctic SIV are substantial and particularly visible around the end of the 20th century, when a steep multidecadal drop in the sea ice extent (SIE) and SIT is

present every month since the beginning of satellite observations in 1979 [Meredith et al., 2019]. However, this significant decline is not fully explained by the anthropogenic forcing. It is estimated that 40-50% of the decrease is caused by the internal natural climate variability [Ding et al., 2019]. Hence, this variability remains an important driver of the Arctic SIV, even through times of intense human-induced climate change, and consequently requires further examination.

1.2 Modes of variability

The MOVs are recurring spatio-temporal climatic structures oscillating non-periodically in time. They are associated with the changing, yet repeating, spatial patterns of one or more climatic variables such as the SST or sea level pressure (SLP). The variations in time, linked with these spatial patterns, can be described by various indices, with each corresponding to an intrinsic periodic scale. These spatio-temporal fluctuations are given rise to by complex climatic processes, and in certain cases by other MOVs directly or indirectly. Such connections between the modes can either be straightforward or intricate, and whilst some of these are known, others are yet to be revealed. Certain MOVs are an indispensable topic of study as their influence on the climate system is considerable, especially as a result of its chaotic behaviour. In particular, this study focuses on the impact of the AO, NAO, NPO, PDO and AMO on the Arctic SIV variability as to further improve our understanding of the underlying mechanisms leading to these variations.

1.3 Current understanding of the impacts of the AO, NAO, NPO, PDO and AMO

1.3.1 Arctic Oscillation and North Atlantic Oscillation

The AO is defined by the difference in SLP between the Arctic polar region and the mid-high latitudes over the Northern Hemisphere [Zheng et al., 2021]. The positive phase of the AO (AO+) is linked with a lower than usual SLP over the Arctic region, whereas a higher than usual SLP is present over the mid-high latitudes across the North Pacific Ocean and North Atlantic Ocean. On the contrary, a negative phase of the AO (AO-) is related to a more intense SLP over the Arctic, while a deeper SLP is found over the mid-high latitudes [Rebecca, 2009]. For visual purposes, the surface pressure (SP) spatial patterns northward of 20°N associated with AO+ and AO- are displayed in Figs. A.1a and A.1b.

The Arctic SIT and SIC variability was previously shown to be associated with the AO by Rigor et al. [2002] and Van Achter et al. [2020], among others. During AO+, the Beaufort High (BH) is weaker and displaced towards Alaska, whereas AO- is related to a stronger and more centrally positioned BH. Such changes in the intensity and location of the BH induce important shifts in the surface winds, which in turn lead to alterations of the SIM spatial patterns. Rigor et al. [2002] found that through AO-, the more pronounced Beaufort Gyre allows a thick multiyear sea ice transport from the western Arctic Ocean to the eastern Arctic Ocean, thus increasing the SIV in the latter region. For the duration of AO+, a weakened and coastward-displaced Beaufort Gyre does not allow such a transport, and instead results in a divergence and convergence of SIM in various regions. In particular, the East Siberian Sea and Laptev Sea are especially affected by an SIM divergence, thereby leading to an SIV decrease. On top of this, the Transpolar Drift Stream (TDS) mainly moves young thin ice, originating in leads, consequently resulting in a prevalent SIV drop south of the Fram Strait and along the southern coast of Greenland. The thick multiyear sea ice transport associated with AO-, instead leads to an SIV increase. Throughout AO+, the shift in the Beaufort Gyre disrupts the sea ice escape from the gyre, and hence lets the ice grow older and thicker. As a result, an SIV increase takes place in the Beaufort Gyre region.

Impacts of the AO on the Baffin Bay and Labrador Sea SIV have also been studied [Limoges et al., 2020]. During AO-, an intense BH leads to a thicker sea ice presence across the Arctic Ocean. This thicker ice, combined with the weaker surface winds over the Nares Strait, cause a blockage in the narrow passage of the strait, therefore impeding the passage of sea ice and low salinity surface waters into the Baffin Bay and Labrador Sea. Additionally, a contracted subpolar gyre associated with AO- increases the influx of salty warm waters towards these regions. Contrastingly, throughout AO+, thinner sea ice is prevalent across the Arctic Ocean. The presence of thinner ice, combined with the intensified winds over the Nares Strait, promotes the passage of sea ice and low salinity waters through the Strait. The lower SATs over the region as a result of the stronger westerlies and wider subpolar gyre, further promote the formation of sea ice.

The NAO is determined by the difference in SLP between the Icelandic Low (IL) and Azores High (AH). During its negative phase (NAO-), the difference is lower, whereas in its positive phase (NAO+), this value is higher [Rebecca Lindsey, 2009]. The SP distribution related with the MOV phases are shown in Figs. A.1c and A.1d. The NAO and AO are highly correlated as the NAO is often considered to be a local manifestation of the AO [Hamouda et al., 2021]. The influence of the NAO on the Atlantic Meridional Overturning Circulation (AMOC) has already been studied [Delworth and Zeng, 2016]. Through NAO+, the stronger westerly winds over the west North Atlantic Ocean amplify the ocean to atmosphere heat transfer, thus increasing the sea surface horizontal density gradient as a result of the lower than usual SSTs. This leads to an intensified AMOC and transport of warm lower-latitude water towards the Arctic Ocean. Subsequently, an SIC decline is observed in various Arctic regions, but especially across the North Atlantic Ocean [Mahajan et al., 2011; Dickson et al., 2000].

Spanning from 1981 to 1994, a period associated with NAO+, a deeper and eastward displaced Aleutian Low (AL) is shown to occur [Hurrell and Loon, 1997]. A sea ice decline in the Bering Sea was also reported during the same period [Mysak and Manak, 1989]. Finally, the NAO is significantly correlated with precipitation around Greenland [Appenzeller et al., 1998]. Negative correlations are found in the south of Greenland, whereas positive correlations are noticeable towards the east.

1.3.2 North Pacific Oscillation and Pacific Decadal Oscillation

The NPO is defined by the depth of the AL. While a positive NPO phase (NPO+) is related to a shallower AL, the negative phase (NPO-) corresponds to a deep AL. The SP spatial patterns linked with the NPO are depicted in Figs. A.1e and A.1f. In turn, the PDO is determined by the SST anomalies in the west, central and east North Pacific Ocean. Throughout its positive phase (PDO+), the west and central North Pacific Ocean are associated with negative SST anomalies, whereas the eastern North Pacific Ocean SST anomalies are positive, and vice versa for the negative phase (PDO-) [Deser and NCARS, 2016]. These SST patterns are displayed in Figs. A.2a and A.2b. An important relationship exists between the NPO and PDO [Newman et al., 2016]. Actually, the NPO, and consequently the intensity of the AL, is shown to be a strong driver of PDO-like SST patterns across the North Pacific Ocean. During NPO-, a profound AL promotes the movement of dry and cold northerly air masses towards the central North Pacific Ocean, thereby lowering the SSTs in the region. Inversely, warm and moist southerly winds are transported along the North American coast, thus resulting in warmer SSTs by the side of this coast.

During NPO-, warm southerly air masses are brought over the east of the Bering Sea [Linkin and Nigam, 2008]. An SAT increase over the Bering Sea was noted as well by Hurrell and Loon [1997], from 1981 to 1994, which was mainly linked with the same phase. Surprisingly, Linkin and Nigam [2008] found no impact on the SIC in this region. Mysak and Manak [1989] observed a sea ice area (SIA) drop in the Bering Sea spanning from 1977 to 1984, when an intense AL was present. Cold northerly air advection was explained to drive an increase in SIC around the western Bering Sea [Linkin and Nigam, 2008] during NPO-. Similarly, an SIC growth in the Sea of Okhotsk was revealed to be driven by an intensified westerly-northwesterly cold wind influx. Linkin and Nigam [2008] also found an SIM divergence away from the Russian coast

because of these winds. Such a relationship between the NPO and Sea of Okhotsk SIC was set forth by Parkinson [1990] as well, where a prominent AL and Siberian High were shown to increase the SIE in the region.

A sea ice loss across the Arctic Ocean was explained to be more important during PDO- than PDO+ [Screen and Francis, 2016]. This link is indirect and is driven by the atmospheric wind shifts associated with the AL position and depth changes. Throughout PDO-, a weaker AL is revealed to promote southerly winds advection towards the Arctic Ocean. As a result, air masses warmed over the sea ice edges in the Bering Sea and Sea of Okhotsk are then transported into the Arctic Ocean. As a consequence, an unusual SAT increase over a large part of the Arctic Ocean is observed. This phenomenon happens over the North Atlantic Ocean as well, where warm air masses from the Greenland Sea, Baffin Bay and Labrador Sea ice edges are brought towards the Arctic Ocean.

1.3.3 Atlantic Multidecadal Oscillation

The AMO is defined by the SST anomalies mean across the North Atlantic Ocean [Trenberth et al., 2021]. In its positive phase (AMO+), the mean SST anomaly is positive, whereas in its negative phase (AMO-), it is negative. The AMO-related SST spatial fields are shown in Figs. A.2c and A.2d. This MOV impacts the Arctic SIV through the fluctuations in the AMOC that are positively correlated with the SAT and negatively correlated with the SIC across most of the Arctic polar region, but especially in the Baffin Bay and Labrador Sea [Mahajan et al., 2011]. It was also shown to partially drive PDO-like SST anomalies across the North Pacific Ocean, as the AMO and PDO are revealed to be negatively correlated [Castruccio et al., 2019].

Finally, the AMO is explained to influence the low cloud coverage over the Arctic region [Castruccio et al., 2019]. An intensified influx of downward longwave radiation induced by re-emissions from the low clouds was observed. Consequently, an SAT increase can be found over various regions where the low cloud coverage is more important. Castruccio et al. [2019] showed that the most affected regions are the Central Arctic, Barents Sea, Kara Sea, East Siberian Sea and Beaufort Sea.

1.4 Impacts of the sea ice on the climate system

Sea ice acts as an insulating layer between the ocean and the atmosphere, since it reduces the exchanges between these two mediums [Vancoppenolle et al., 2009]. The momentum transfers between the atmosphere and ocean are lessened, as a portion of the transferred energy is absorbed by the sea ice. The ocean currents and climate processes associated with them are consequently affected. Additionally, the direct heat transfers between the ocean and atmosphere are modified because of the small thermal conductivity of sea ice. The mass exchanges are impacted as well, since the sea ice acts as an impermeable boundary. For instance, gases such as CO_2 are not absorbed as effectively by the ocean. Such impediments can lead to global carbon cycle changes, but may also alter other processes composing the climate system. Furthermore, bacteria and microscopic plants that play a role in the carbon cycle live in the ice, and therefore, alterations in the sea ice affect their population, and with it, the carbon cycle.

The radiative exchanges are impacted as well because of the differing albedos between the ocean surface and sea ice. While the ocean surface possesses a low albedo of about 0.06, sea ice, on the other hand, has a much greater albedo ranging from about 0.5 to 0.7 [NSIDC, 2020]. Consequently, the ocean absorbs less solar radiation if it is covered by ice, and this effect becomes even more prominent when a layer of snow covers the ice. Snow-covered sea ice has an albedo of about 0.9. This means that only 10% of the incoming solar radiation is absorbed by the surface [NSIDC, 2020]. Since sea ice extends the farthest and is mainly covered by snow in winter, it makes this season the most isolating for the polar region ocean. Contrastingly, in summer, the snow cover tends to melt, hence resulting in the creation of a new thin layer of water, with a

lower albedo than sea ice, over the surface [Morales et al., 1997].

Sea ice is an important driver of the sea surface salinity (SSS). The formation of sea ice releases salt into the ocean, while its melting mostly liberates freshwater. This process of salt and freshwater discharge influences the stratification of the ocean and AMOC [Vancoppenolle et al., 2009]. A decrease in the SSS at such high latitudes may disrupt the AMOC, as it is driven by density differences between the low- and high-latitude oceans [Rahmstorf et al., 2005]. Because of the meridional oceanic heat transport provided by the AMOC, an interruption or weakening of this circulation therefore results in smaller temperature differences between the high and low latitudes. On top of this, a larger SSS reduces the formation rate of new sea ice at the ocean surface.

Various feedbacks taking place in the polar regions are partially governed by sea ice. These feedbacks are overall less stabilising than around the tropics. Hence, when the climate is affected by a perturbation, the temperatures in the polar regions vary the most. This phenomenon is known as the polar amplification [Goosse et al., 2018]. Because of the contribution of sea ice, alterations in its distribution across the polar regions can either dampen or amplify this phenomenon.

Finally, remote impacts through teleconnections have been studied. Some recent papers have set forth potential impacts of the Arctic sea ice on the mid-latitude regions. Some of these studies have shown that, throughout certain periods, sea ice loss in the Barents Sea and Kara Sea could lead to cold weather in eastern Asia [Kim et al., 2014; Kretschmer et al., 2016]. Other articles suggest that sea ice anomalies in the Chukchi Sea and areas west of Greenland are linked with cold weather in eastern North America [Kug et al., 2015; Ballinger et al., 2018; Overland et al., 2019]. Such teleconnections are complicated to explain due to the chaotic behaviour of the climate system [Meredith et al., 2019]. This topic is consequently still under debate in the literature.

1.5 Objectives

The objectives of this thesis are to answer the following 3 questions for all 5 MOVs (AO, NAO, NPO, PDO and AMO):

- Which Arctic regions are particularly impacted by the MOV in question?
- How does the respective MOV affect the SIV in these regions?
- When has this effect been the most pronounced throughout the 20th century?

For this purpose, we consider the 13 Arctic regions represented in Fig. 2.1, where the regional borders are defined by the National Snow and Ice Data Center NSIDC [2022]. We carry out a spatio-temporal analysis of the monthly data, spanning from 1901 to 2010, provided by the Pan-Arctic Ice Ocean Modelling and Assimilation System 1901-2010 Arctic sea ice reconstruction (PIOMAS-20C) reanalysis [Schweiger et al., 2019] and its ECMWF 20th century reanalysis (ERA-20C) atmospheric forcing data [Poli et al., 2016; ECMWF, 2016]. First, the index corresponding to each MOV is built by using the ERA-20C datasets. The produced AO, NAO and NPO indices are based on the SP data, whereas the PDO and AMO indices are calculated by means of the SST data. Following this, a spatial analysis of the Arctic SIV distribution changes, and their relation to the dynamic and thermodynamic processes corresponding to each MOV, is performed. This step allows us to partially answer the first and second questions, although a temporal analysis is required for a complete solution. In this study, we carry out a wavelet analysis to identify the time frames and frequencies of the most important regional SIV impacts related to the various MOVs. In particular, the MOVs-associated dynamic and thermodynamic footprints in the SIV shifts of the regions are highlighted. Finally, lag-tests are computed to reveal the response-times of the regionally felt SIV impacts following the shifts in the

MOVs. These procedures fully answer the 3 questions at hand. By the end of this thesis, the dynamics- and thermodynamics-induced changes in the Arctic SIV associated with the various MOVs will be explained, with a distinction between the effects associated with and driven by the MOVs being established. The underlying mechanisms driving these processes, the time periods and frequency of their influence will be determined as well.

Chapter 2

Data description and validation

In this chapter, we first introduce the PIOMAS-20C and ERA-20C reanalyses utilised throughout our work [Schweiger et al., 2019; Poli et al., 2016]. We then validate the employment of the PIOMAS-20C SIV data by comparing the PIOMAS-20C SIC and SIT simulated data with the observations made available by the Exploitation of Meteorological Satellites Ocean and Sea Ice Satellite Application Facility (EUMETSAT OSI SAF) [Copernicus, 2020a] and Envisat satellite [Copernicus, 2020b].

2.1 Descriptions of the reanalyses

2.1.1 PIOMAS-20C reanalysis

The PIOMAS-20C reanalysis [Schweiger et al., 2019] is based on the Pan-Arctic Ice Ocean Modelling and Assimilation System (PIOMAS) model [Zhang and Rothrock, 2003]. The model was integrated over the 1901-2010 period forced by the European Centre for Medium-Range Forecasts (ECMWF) ERA-20C atmospheric reanalysis data [Poli et al., 2016]. This reconstructed atmospheric data gives the required boundary conditions to run the model throughout the period of interest. This model uses a curvilinear mesh, with the grid converging in Greenland, and averaging a grid-cell size of about 40 km. The domain of the model excludes some parts of the Sea of Okhotsk and Labrador Sea regions. Fig. 2.1 displays the domain covered by the PIOMAS model, the grid points and the regions studied in this work.

Two different calibrations were made for the PIOMAS-20C reconstruction [Schweiger et al., 2019]. The first was an SIM calibration aimed at minimizing the differences between the simulated SIM speeds and the observational data provided by drifting buoys from the International Arctic Buoy Program (IABP) [Zhang et al., 2012]. Secondly, a mean SIT calibration was applied. A melting sea ice surface albedo adjustment was implemented to minimize the differences between the model and observations available from the Unified Sea Ice Thickness Climate Data Record (ThickCDR) [Lindsay, 2010].

The PIOMAS-20C SIC is assimilated with the data provided by the HadISST version 2.1 (HadISST2) analysis [Titchner and Rayner, 2014] in the marginal zones. An optimal interpolation assimilation approach is utilised [Schweiger et al., 2019]. This method corrects the simulated SIC with observations by using a weighting factor:

$$\hat{C}^{mod} = C^{mod} + \mathbf{K}(\mathbf{C^{obs}} - \mathbf{C^{mod}})^T,$$

where T is the transpose, $\hat{C}^{mod}$ the corrected model SIC at a given location, C_{mod} the model SIC first estimate for that location, $\mathbf{C^{obs}} = (C_1^{obs}, ..., C_N^{obs})$ the observed SIC vector containing the observed concentration in

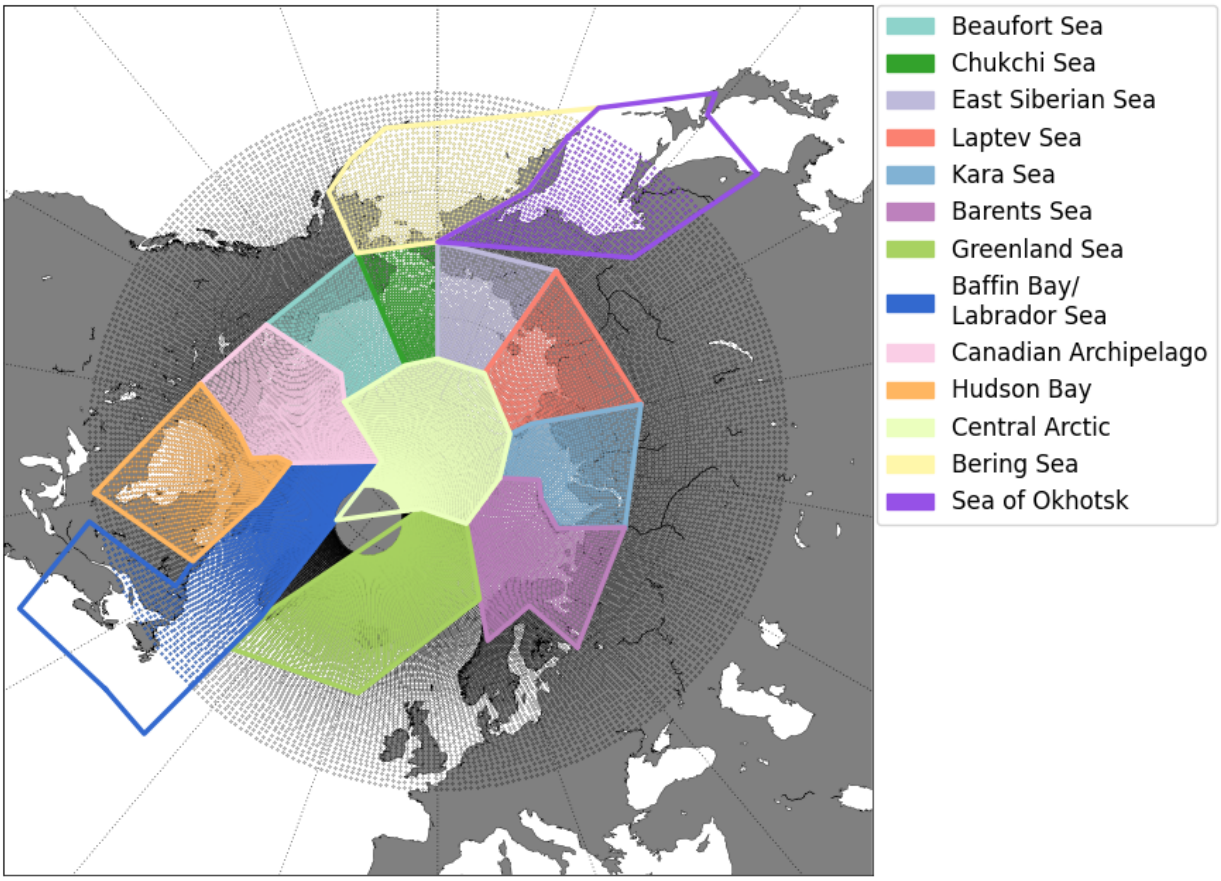


Fig. 2.1 – The grid points (**black points**) of the PIOMAS-20C reconstruction and the 13 different Arctic regions considered in this study. The Labrador Sea and Sea of Okhotsk are not fully covered by the domain of the model. The PIOMAS-20C grid points can be found at PSC [2019], whereas the Arctic regions boundaries are provided by NSIDC [2022].

N different locations, $\mathbf{C^{mod}} = (C_1^{mod}, ..., C_N^{mod})$ the same vector for the model simulated concentration and $\mathbf{K} = (K_1, ..., K_N)$ the weighting factor for the N different locations. More details on how this assimilation method determines the weighting factors can be found in Zhang et al. [2003].

2.1.2 ERA-20C reanalysis

The ERA-20C atmospheric forcing data which drives the PIOMAS model [Poli et al., 2016] consists of downwelling longwave and shortwave fluxes, 10-m wind speeds, SATs, humidities, SSTs, and ocean-atmosphere exchanges, with a daily resolution [Schweiger et al., 2019]. The provided SST dataset is based on the HadISST2 analysis. The ERA-20C reanalysis went through assimilation for both the SP and marine 10-m wind speeds.

The performance of this reanalysis over the Arctic sea ice was assessed by comparison with data from other reanalyses and observations [Schweiger et al., 2019]. The comparison was done for the downwelling radiative fluxes, 10-m wind speeds and SATs, for which the observations were provided by the Surface Heat Budget of the Arctic Experiment (SHEBA), Maud expedition and former Soviet Union North Polar (NP) stations. After careful assessment, Schweiger et al. [2019] decided that it was the best suited atmospheric

dataset for the period of interest.

2.2 PIOMAS-20C SIV data validation

To validate the PIOMAS-20C SIV data employed in this study, we need observations covering the entire Arctic region. We thus base our validation over the 1979-2010 period, during which global satellite observations exist. Here, we verify the PIOMAS-20C SIC and SIT products used to create the SIV dataset.

2.2.1 Sea ice concentration

We first assess the simulated SIC data by comparing it with the EUMETSAT OSI SAF observations [Copernicus, 2020a]. This gridded satellite dataset is based on a polar projection grid, with a resolution of 25 km. The EUMETSAT OSI SAF product was chosen due to its consistency throughout the 1979-2010 period. For convenience, we interpolate this data onto the PIOMAS-20C mesh as to ease the visual comparison and allow the computation of the differences between the model and observations. We compare the mean SIC between the simulation and observations in March and September [Fig. 2.2]. The model especially overestimates the concentration close to the marginal zone, but not as much in it as a result of the SIC data assimilation constraining the model in this area. Both in March and September, close to the marginal zone, the difference between the model and observations reaches up to 50% in SIC, whereas across the other regions, the difference is barely noticeable. This SIC overestimation seems to be caused by the presence of thinner ice, which is more prone to melt, and as a result, more vulnerable to noisy variability.

2.2.2 Sea ice area

We now compare the pan-Arctic SIA mean seasonal cycles between the simulation and observations [Fig. 2.3]. The model overestimates the SIA every month, due to the SIC overestimation near the marginal zone [Fig. 2.2]. The simulation and observations comparison in the various Arctic regions is displayed in Fig. 2.4. Again, the model tends to overestimate the SIA. This overestimation appears and disappears in many regions, depending on the seasons, because of the movement of the sea ice front.

Next, we compare the pan-Arctic SIA anomalies for the months of March and September [Fig. 2.5]. The anomaly is computed by removing the mean of the data, for the 1979-2010 period, from the data itself. Both the simuations and observations are close, and exhibit a downward trend that is particularly noticeable in September. This is an important outcome since this study focuses on the sea ice variability. Tables 2.1 and 2.2 show the correlations between the simulation and observations, the simulation linear trend and observation linear trend for the pan-Arctic region. Overall, the correlation is high and the trends are similar in both months. The correlation in March is lower than September, whereas the trends are closer. To explain these results, we must consider the regional comparison between the simulation and observations. The results are especially alike across most regions in September [Fig. 2.6b]. In March [Fig. 2.6a], the observations display greater SIA anomalies than the model in numerous regions (Beaufort Sea, Chukchi Sea, East Siberian Sea, Laptev Sea, Kara Sea, Canadian Archipelago, Hudson Bay and Central Arctic). The differences between the linear trends of the simulation and observations are noticeable in these regions as well [Tables 2.1 and 2.2]. In September, both the correlations and trends of the model are more accurate than in March. The SIA overestimation in Figs. 2.3 and 2.4 does not appear in Figs. 2.5 and 2.6, since the anomalies suppress it.

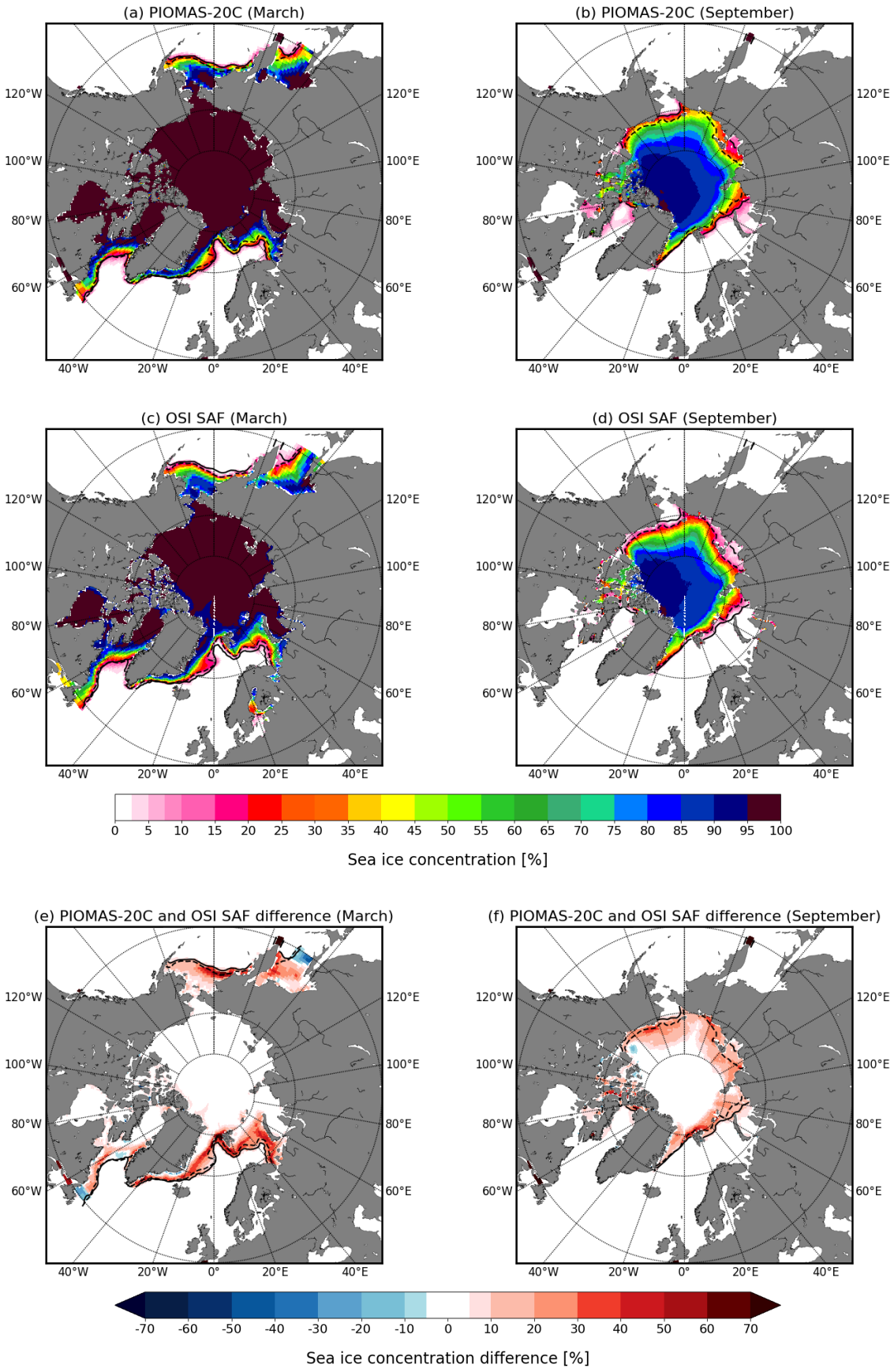


Fig. 2.2 – Simulated (PIOMAS-20C) mean SIC for the 1979-2010 period for the months of (a) March and (b) September. Observed (OSI SAF) mean SIC for the 1979-2010 period for the months of (c) March and (d) September. Absolute SIC difference between the simulated and observed 1979-2010 mean SIC for the months of (e) March and (f) September. Positive values in (e) and (f) indicate a model overestimation. In all panels, the black solid (PIOMAS-20C) and dashed (OSI SAF) contours represent the mean simulated and observed 15% SIC level for the period of interest, respectively.

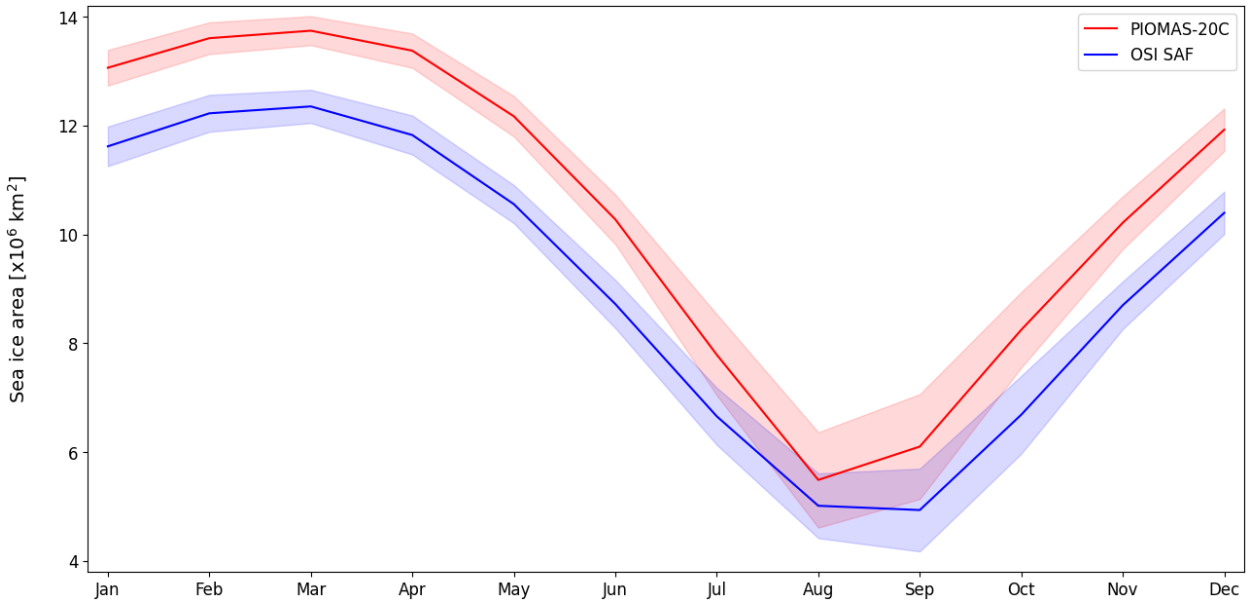


Fig. 2.3 – Simulated (PIOMAS-20C; **red**) and observed (OSI SAF; **blue**) mean seasonal cycles for the pan-Arctic SIA for the 1979-2010 period. Error bars represent the one standard deviation for the 1979-2010 period.

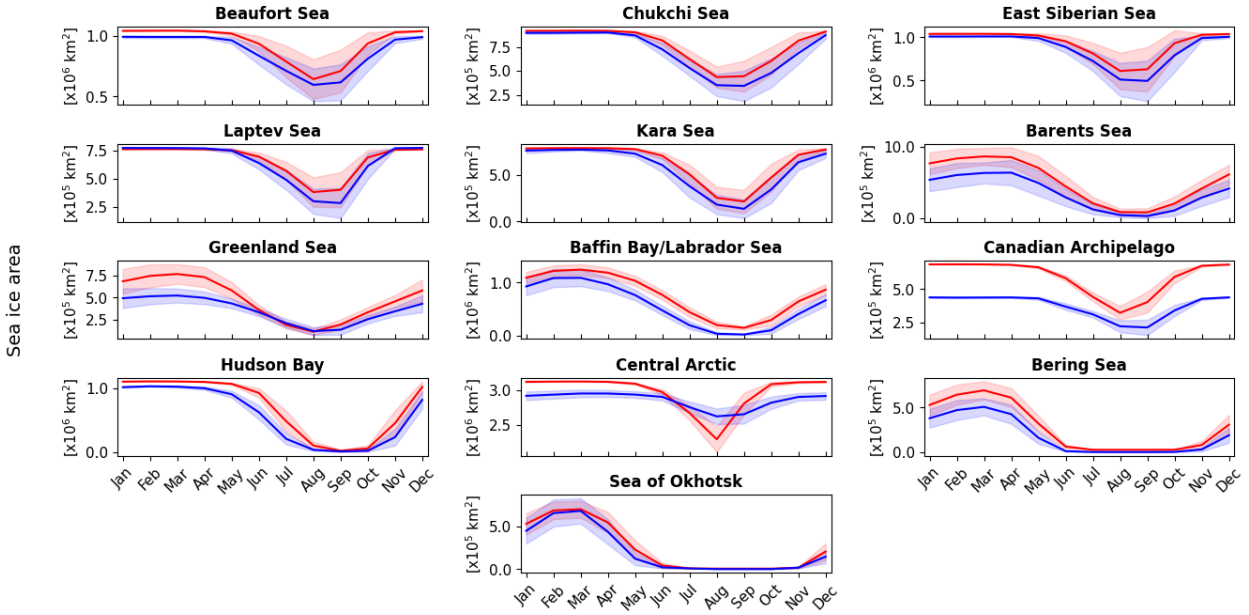


Fig. 2.4 – Simulated (PIOMAS-20C; **red**) and observed (OSI SAF; **blue**) mean seasonal cycles for the Arctic regions SIA for the 1979-2010 period. Error bars represent the one standard deviation for the 1979-2010 period. Note that the y-axis range is not the same for all the regions.

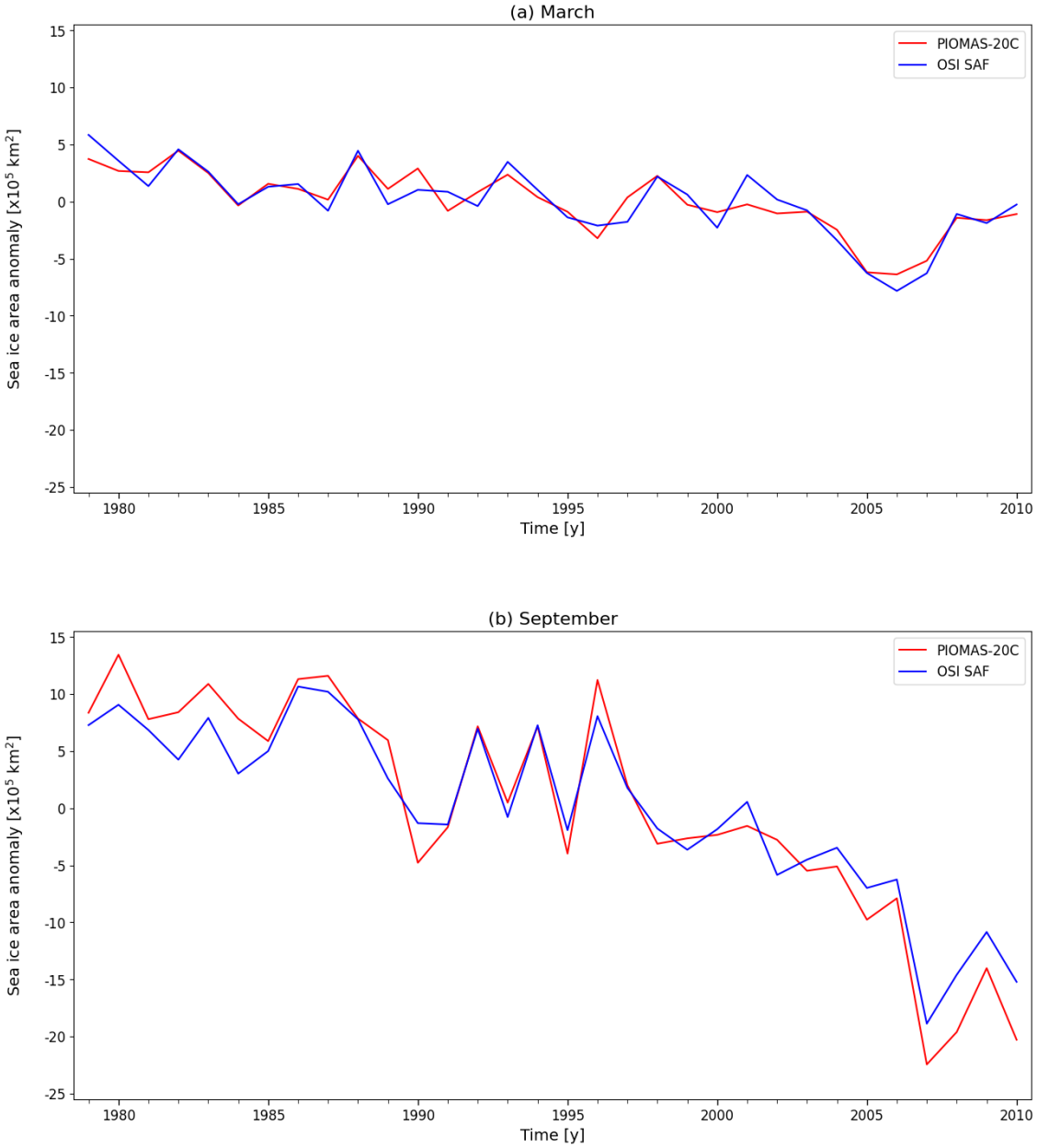


Fig. 2.5 – Simulated (PIOMAS-20C; **red**) and observed (OSI SAF; **blue**) pan-Arctic SIA anomalies spanning from 1979 to 2010 for the months of (a) March and (b) September.

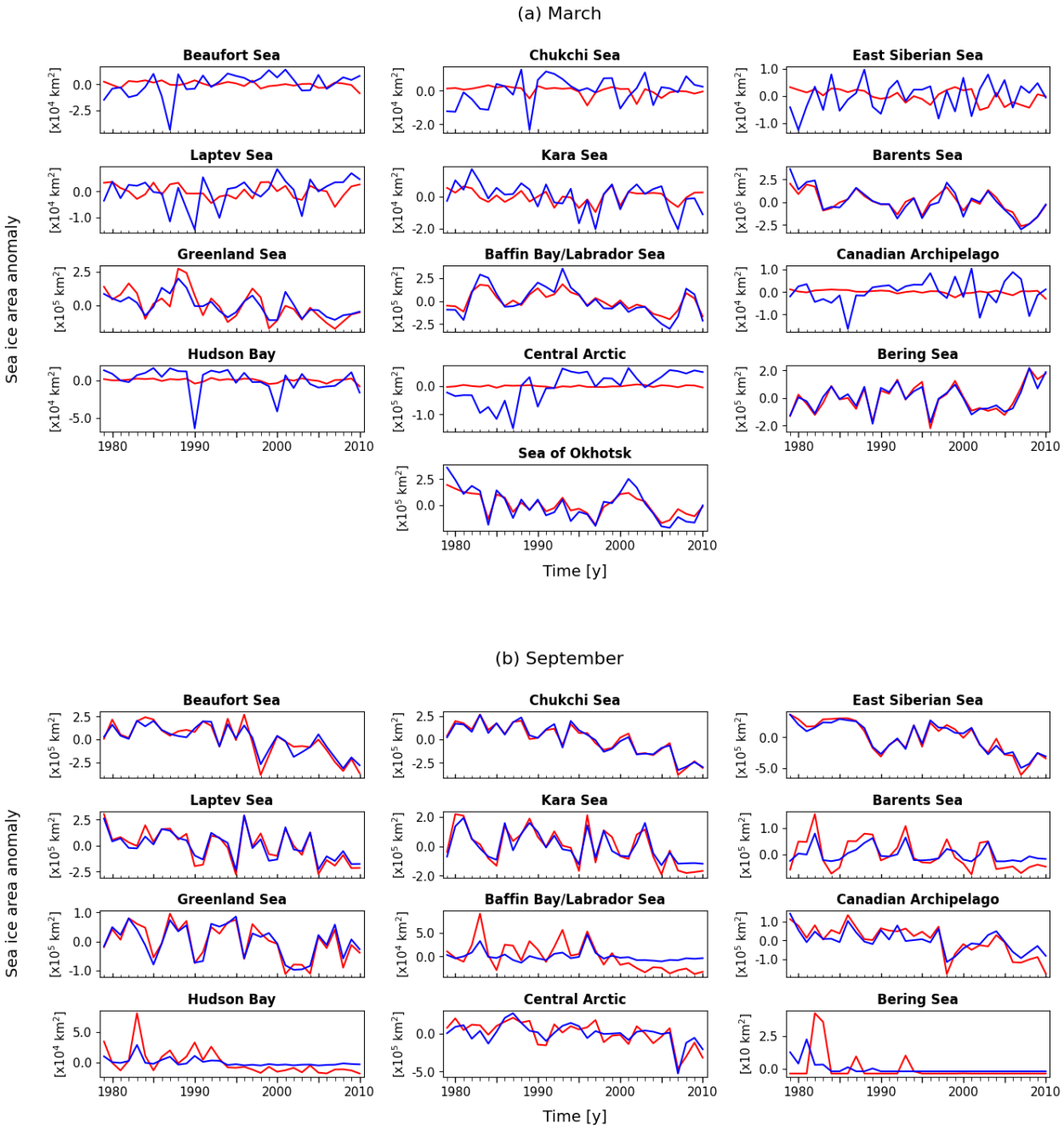


Fig. 2.6 – Simulated (PIOMAS-20C; **red**) and observed (OSI SAF; **blue**) SIA anomalies for the Arctic regions spanning from 1979 to 2010 for the months of (a) March and (b) September. Note that the y-axis range is not the same for all the regions.

Table 2.1 – Pearson correlation coefficients (r) estimated between the model and observations, linear model trends (t_{mod}) and linear observation trends (t_{obs}) for the month of March, as shown in Figs. 2.5a and 2.6a. Significant correlations (p-value $\leq$ 0.01) are highlighted in bold.

Region	r	t_{mod} $[km^2/dec]$	t_{obs} $[km^2/dec]$
Pan-Arctic	**0.93**	-1.95 x 10^5	-2.04 x 10^5
Beaufort Sea	-0.26	-1.17 x 10^3	4.6 x 10^3
Chukchi Sea	0.1	-1.12 x 10^3	2.71 x 10^3
East Siberian Sea	-0.26	-1.32 10^3	1.4 x 10^3
Laptev Sea	0.1	-4.14 x 10^2	1.51 x 10^3
Kara Sea	**0.7**	-6.06 x 10^2	-3.45 x 10^3
Barents Sea	**0.96**	-6.03 x 10^4	-7.89 x 10^4
Greenland Sea	**0.87**	-6.51 x 10^4	-4.29 x 10^4
Baffin Bay/Labrador Sea	**0.97**	-4.15 x 10^4	-5.51 x 10^4
Canadian Archipelago	-0.41	-4.53 x 10^2	8.47 x 10^2
Hudson Bay	**0.69**	-8.1 x 10^2	-4.55 x 10^3
Central Arctic	0.07	1.09 x 10^2	3.7 x 10^4
Bering Sea	**0.97**	2.73 x 10^4	1.95 x 10^4
Sea of Okhotsk	**0.96**	-5.01 x 10^4	-7.05 x 10^4

Table 2.2 – Pearson correlation coefficients (r) estimated between the model and observations, linear model trends (t_{mod}) and linear observation trends (t_{obs}) for the month of September, as shown in Figs. 2.5b and 2.6b. Significant correlations (p-value $\leq$ 0.01) are highlighted in bold.

Region	r	t_{mod} $[km^2/dec]$	t_{obs} $[km^2/dec]$
Pan-Arctic	**0.98**	-8.11 x 10^5	-6.27 x 10^5
Beaufort Sea	**0.96**	-1.2 x 10^5	-1.03 x 10^5
Chukchi Sea	**0.99**	-1.31 x 10^5	-1.27 x 10^5
East Siberian Sea	**0.98**	-1.84 x 10^5	-1.65 x 10^5
Laptev Sea	**0.97**	-8.28 x 10^4	-6.46 x 10^4
Kara Sea	**0.95**	-6.29 x 10^4	-4.44 x 10^4
Barents Sea	**0.91**	-2.31 x 10^4	-7.59 x 10^3
Greenland Sea	**0.94**	-2.49 x 10^4	-1.66 x 10^4
Baffin Bay/Labrador Sea	**0.77**	-1.63 x 10^4	-3.09 x 10^3
Canadian Archipelago	**0.88**	-5.68 x 10^4	-3.31 x 10^4
Hudson Bay	**0.95**	-1.16 x 10^4	-3.48 x 10^3
Central Arctic	**0.79**	-9.73 x 10^4	-5.9 x 10^4
Bering Sea	0.13	-3.76	-2.63

2.2.3 Sea ice thickness

Finally, we compare the SIT dataset provided by the PIOMAS-20C reanalysis with observations spanning from 2002 to 2010. These are derived from measurements performed by the Envisat satellite [Copernicus, 2020b]. The gridded satellite data is based on a polar projection grid, with a resolution of 25 km. The SIT observational data is interpolated into the PIOMAS-20C mesh for visualisation and comparison purposes. Limitations of this product lie on the fact that it only covers a small portion of the desired period (1979-2010), and reliable measurements are only available in the colder months. Another problem arises from the fact that the orbit of the satellite is not completely polar, and thus does not cover regions beyond a certain latitude. Consequently, we only compare the mean SIT provided by the model and observations over the 2002-2010 period, in March, and for grid points to the south of 87°N. The results are shown in Fig. 2.7. The model overestimates the SIT up to around 1 m towards the 80°N-85°N, 120°W-120°E region. An SIT underestimation of the simulation is also noticeable along the eastern coast of Greenland. Differences, although not as remarkable, are observed in other parts of the Arctic region as well.

In this section, we have validated the PIOMAS-20C SIC and SIA dataset for the 1979-2010 period, by comparing it with the observational data provided by the EUMETSAT OSI SAF satellite. Following this, a comparison of the PIOMAS-20C SIT product with the Envisat satellite SIT observational data, spanning from 2002 to 2010, was performed. Overall, the the PIOMAS-20C reanalysis is sufficiently reasonable for a regional study of the Arctic SIV variability to be carried out.

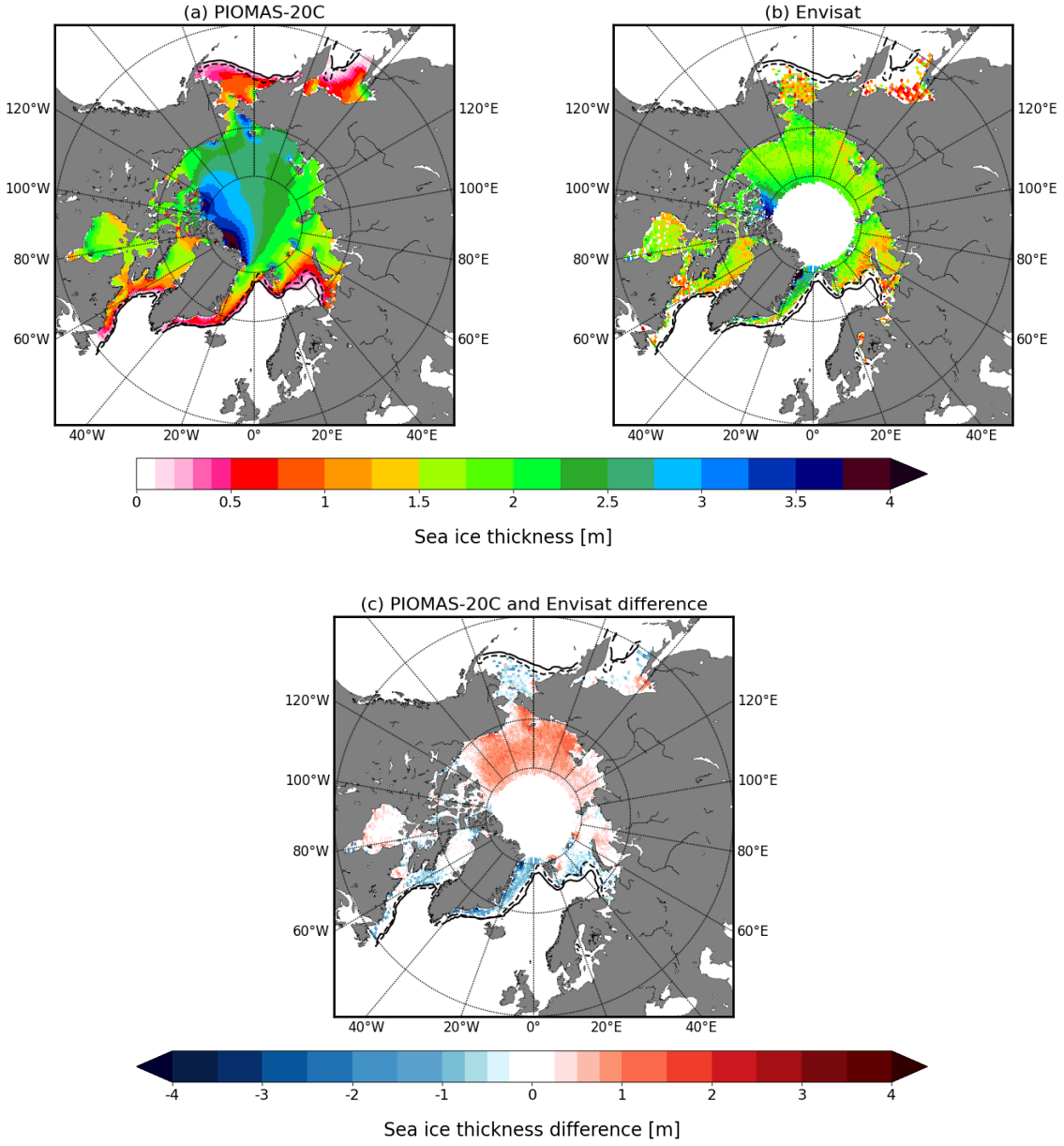


Fig. 2.7 – (a) Simulated (PIOMAS-20C) mean SIT for the 2002-2010 period for the month of March. (b) Observed (Envisat) mean SIT for the 2002-2010 period for the month of March. (c) SIT differences between the simulated and observed mean SIT for the month of March. Positive values in (c) indicate an SIT model overestimation compared to the observations. In all panels, the black solid (PIOMAS-20C) and dashed (Envisat) contours represent the mean simulated and observed 15% SIC level for the period of interest, respectively.

Chapter 3

Methodology

In this chapter, we present the methodology used to study the Arctic SIV spatio-temporal variability as provided by the PIOMAS-20C reanalysis. We first introduce the datasets employed in this work as well as the pre-processing methods applied to them. Following this, an explanation of the performed data interpolation and SIM divergence computation is conducted. Next, the various mathematical tools utilised in the course of this thesis are described and explained. Finally, we define the indices used throughout the rest of the paper.

3.1 ERA-20C and PIOMAS-20C datasets

We make use of numerous datasets provided by the ERA-20C atmospheric and PIOMAS-20C reanalyses. The SP [ECMWF, 2018c], 10-m wind zonal component [ECMWF, 2018d], 10-m wind meridional component [ECMWF, 2018e], instanteneous surface sensible heat flux (SSHF) [ECMWF, 2019], vertically integrated thermal energy flux divergence (ITEFD) [ECMWF, 2018f], SAT [ECMWF, 2018a] and SST [ECMWF, 2018b] ERA-20C datasets [ECMWF, 2016] are employed. The SSHF depicts the transfer of sensible heat between the surface of the Earth and the atmosphere at a given point in time. Consequently, this flux does not take into account the latent heat transfers. The positive values associated with this variable indicate the presence of an atmosphere to ocean sensible heat transfer, and a ocean to atmosphere sensible heat transfer for the negative values. The ITEFD data is produced by computing the divergence of the vertically integrated thermal energy flux. The thermal energy flux is integrated vertically from the surface of the Earth to the top of the atmosphere. This quantity indicates the regions above which the vertically integrated thermal energy is increased by convergence or decreased by divergence. Negative values of the ITEFD imply a convergence of thermal energy flux, whereas positive values depict a divergence of thermal energy flux. Therefore, this variable determines the regions over which an overall influx or outflux of atmospheric heat transport takes place. The SP and 10-m winds illustrate the driving mechanisms leading to the various dynamical processes, although they are employed for the explanation of the thermodynamical processes as well. The SAT and SST spatio-temporal distributions are used to investigate the thermodynamic influence on the Arctic SIV, while the SSHF and ITEFD partially explain the underlying mechanisms leading to such patterns. The PIOMAS-20C SIC, SIT and SIM datasets [Schweiger et al., 2019] are used to produce the SIV data and to deduce the spatio-temporal dynamic impacts induced by the SIM shifts.

3.2 Data pre-processing

The SIV dataset displays important multidecadal linear trends throughout the 20th century. These include a noticeable downtrend from 1901 to 1935, an uptrend spanning from 1935 to 1970 and a steep downtrend from 1979 to 2010. Unfortunately, these significant and long-lasting linear trends lead to complications in the

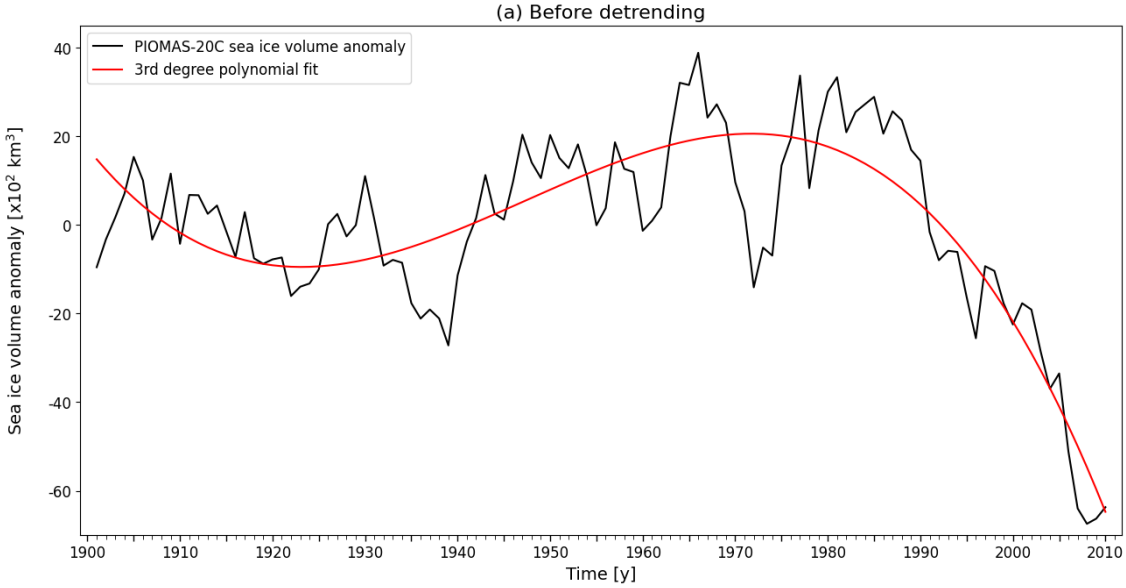
data processing. As a matter of fact, the wavelet analysis interprets these trends as important low frequency signals that conceal the additional weaker and higher frequency variabilities of interest. Furthermore, these low frequency signals cannot be analysed reliably, as a result of the dataset time span limitations. To avoid such hurdles, an adequate detrending approach is essential. Here, we follow a three-step procedure:

- For every month individually, a 3rd degree polynomial fit is calculated for the SIV anomaly time series in each grid-cell. Throughout this thesis, the anomaly is calculated by subtracting the time series mean from the time series values. Fig. 3.1a shows the September pan-Arctic SIV anomaly time series and its 3rd degree polynomial fit as an illustration.

- The SIV anomaly time series in each grid-cell is then detrended by the 3rd degree polynomial fit. Fig. 3.1b displays the detrended time series shown in Fig. 3.1a.

- We then construct the detrended monthly time series of each grid-cell by combining the detrended time series of all months. This leads to a new SIV dataset containing the monthly detrended time series of the SIV anomaly in all grid-cells.

We also apply a 3-year moving average on the corresponding grid-cells SIV time series to remove any variabilities of lower periods than 3 years, as they are not targeted by this study. From now on, the detrending and 3-year smoothing is applied on all the analyses employed in this thesis for consistency. Thus, henceforth all datasets and time series utilised span from mid-1902 to mid-2009.



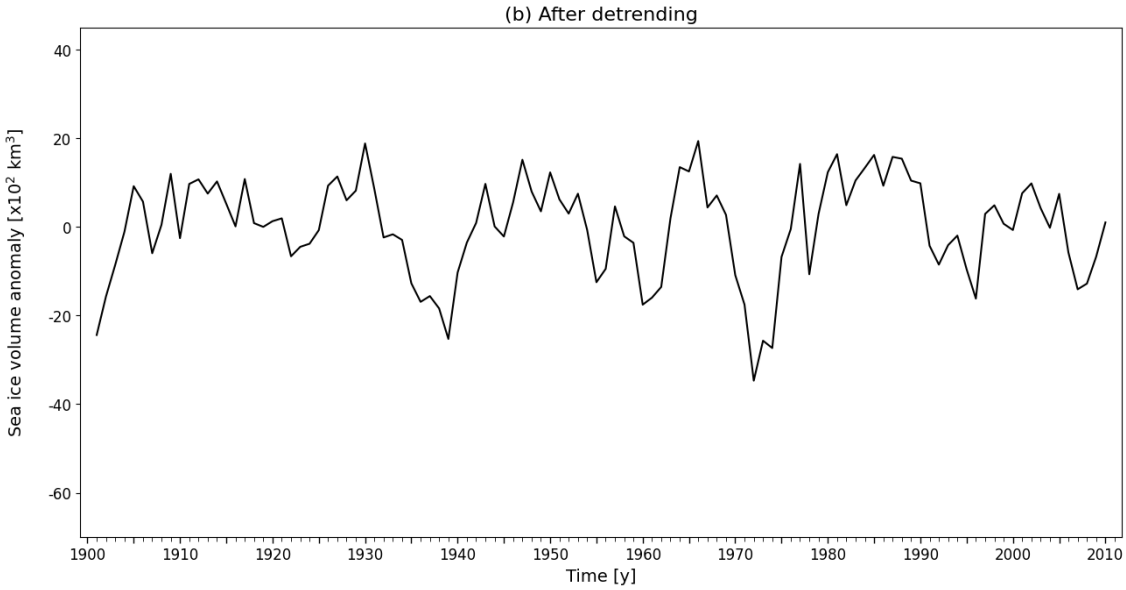


Fig. 3.1 – Illustration of the detrending procedure applied to the datasets. (a) PIOMAS-20C pan-Arctic SIV anomalies for the month of September (**black**) and the 3rd degree polynomial fit (**red**). (b) PIOMAS-20C pan-Arctic SIV anomalies for the month of September detrended with the 3rd degree polynomial fit. This figure only demonstrates the detrending process as it depicts the pan-Arctic SIV anomalies, whereas only the time series corresponding to each grid point is detrended.

3.3 Interpolation of the data, computation of the sea ice motion divergence and surface pressure gradients

The ERA-20C data is interpolated onto the PIOMAS grid. This guarantees an easier comparison and analysis of the results. The PIOMAS mesh is chosen due to its greater resolution across the Arctic polar region. Because of its spatial limitations, as it is only defined northward of 50°N, the construction of the various MOVs indices is based on the original non-interpolated ERA-20C data. The ERA-20C grid is global and possesses a spatial resolution of 1° along both the latitudes and longitudes.

The computation of the SIM divergence is inspired by Vomero et al. [2021], and is given as follows:

$$(\boldsymbol{\nabla} \cdot \boldsymbol{v}_{ice})_{i,j} \approx \frac{u_{ice}(i, j+\frac{1}{2}) - u_{ice}(i, j-\frac{1}{2})}{\cos\left(lat(i,j)\right) R\left(lon(i, j+\frac{1}{2}) - lon(i, j-\frac{1}{2})\right)} + \frac{v_{ice}(i+\frac{1}{2}, j) - v_{ice}(i-\frac{1}{2}, j)}{R\left(lat(i+\frac{1}{2}, j) - lat(i-\frac{1}{2}, j)\right)}, \tag{3.1}$$

where R is the average radius of the Earth, lon and lat are the longitudes and latitudes in radiants, respectively, $\boldsymbol{v}_{ice} = (u_{ice}, v_{ice})$ is the sea ice velocity vector and i, j are the latitudinal and longitudinal iterations, respectively. Since the PIOMAS grid is centered on Greenland, it renders the calculation of the divergence fields complicated. Hence, we interpolate the PIOMAS-20C SIM fields onto a grid centered on the North Pole, with a resolution of 0.25° along the latitudes and 1° along the longitudes, covering the region 50°N-90°N,0°E-359°E. Afterwards, a second similar but shifted grid, with the same resolution and covering 50.125°N-89.875°N,0.5°E-359.5°E, is created. Finally, the SIM divergence field is produced on the second grid using the interpolated SIM data. The SP gradient vectors are calculated using a similar shifted two-gridded method.

3.4 Empirical orthogonal functions

The Empirical Orthogonal Function (EOF) analysis allows us to find spatial patterns of various variables, and how they change with time. The objective of this method is to produce two matrices T and U that represent and differentiate the most important temporal variances of a given dataset. To achieve this, a sequence of steps is carried out [François, 2021]:

- A matrix M of dimensions $(i \times j \times n)$ containing the values of the variable at hand in $(i \times j)$ grid points and for n time iterations is required. M is then flattened as to result in a $(m \times n)$ matrix X with $m = i \times j$.
- X may then be rotated appropriately, with a $(m \times m)$ matrix R, as to produce the desired matrix T:

$$\begin{bmatrix} T_{11} & T_{12} & \dots & T_{1m} \\ T_{21} & T_{22} & & \vdots \\ \vdots & & \ddots & \vdots \\ T_{n1} & \dots & \dots & T_{nm} \end{bmatrix} = \begin{bmatrix} X_{11} & X_{12} & \dots & X_{1m} \\ X_{21} & X_{22} & & \vdots \\ \vdots & & \ddots & \vdots \\ X_{n1} & \dots & \dots & X_{nm} \end{bmatrix} \cdot \begin{bmatrix} R_{11} & R_{12} & \dots & R_{1m} \\ R_{21} & R_{22} & & \vdots \\ \vdots & & \ddots & \vdots \\ R_{m1} & \dots & \dots & R_{mm} \end{bmatrix}. \tag{3.1}$$

- R can be found by calculating the covariance matrix C of X:

$$\begin{bmatrix} C_{11} & C_{12} & \dots & C_{1m} \\ C_{21} & C_{22} & & \vdots \\ \vdots & & \ddots & \vdots \\ C_{m1} & \dots & \dots & C_{mm} \end{bmatrix} = \frac{1}{n-1} \begin{bmatrix} X_{11} & X_{12} & \dots & X_{1m} \\ X_{21} & X_{22} & & \vdots \\ \vdots & & \ddots & \vdots \\ X_{n1} & \dots & \dots & X_{nm} \end{bmatrix}^{Tr} \cdot \begin{bmatrix} X_{11} & X_{12} & \dots & X_{1m} \\ X_{21} & X_{22} & & \vdots \\ \vdots & & \ddots & \vdots \\ X_{n1} & \dots & \dots & X_{nm} \end{bmatrix},$$

  where Tr is the transpose.
- Since C is symmetric, we can diagonalise it to deduce its invertible matrix U containing the orthogonal eigenvectors:

$$\begin{bmatrix} C_{11} & C_{12} & \dots & C_{1m} \\ C_{21} & C_{22} & & \vdots \\ \vdots & & \ddots & \vdots \\ C_{m1} & \dots & \dots & C_{mm} \end{bmatrix} = \begin{bmatrix} U_{11} & U_{12} & \dots & U_{1m} \\ U_{21} & U_{22} & & \vdots \\ \vdots & & \ddots & \vdots \\ U_{m1} & \dots & \dots & U_{mm} \end{bmatrix} \cdot \begin{bmatrix} \Lambda_{11} & \Lambda_{12} & \dots & \Lambda_{1m} \\ \Lambda_{21} & \Lambda_{22} & & \vdots \\ \vdots & & \ddots & \vdots \\ \Lambda_{m1} & \dots & \dots & \Lambda_{mm} \end{bmatrix} \cdot \begin{bmatrix} U_{11} & U_{12} & \dots & U_{1m} \\ U_{21} & U_{22} & & \vdots \\ \vdots & & \ddots & \vdots \\ U_{m1} & \dots & \dots & U_{mm} \end{bmatrix}^{Tr},$$

  with Λ a diagonal matrix containing the eigenvalues of C.
- We then use U as R in Eq. 3.1 to rotate X. We thus get the final relation:

$$\begin{bmatrix} X_{11} & X_{12} & \dots & X_{1m} \\ X_{21} & X_{22} & & \vdots \\ \vdots & & \ddots & \vdots \\ X_{n1} & \dots & \dots & X_{nm} \end{bmatrix} = \begin{bmatrix} T_{11} & T_{12} & \dots & T_{1m} \\ T_{21} & T_{22} & & \vdots \\ \vdots & & \ddots & \vdots \\ T_{n1} & \dots & \dots & T_{nm} \end{bmatrix} \cdot \begin{bmatrix} U_{11} & U_{12} & \dots & U_{1m} \\ U_{21} & U_{22} & & \vdots \\ \vdots & & \ddots & \vdots \\ U_{m1} & \dots & \dots & U_{mm} \end{bmatrix}^{Tr}. \tag{3.2}$$

In Eq. 3.2, the first lines of U^{Tr} describe the spatial patterns, or modes, associated with the most important variances, whereas the first columns of T represent the variations in time of the amplitude of the associated spatial patterns and are called the principal components (PCs). For the purpose of this work, EOFS are used to build some of the MOVs indices. To do this, we employ the Python module "eofs" [Dawson, 2016], which produces the EOF modes and associated PCs of a given dataset.

3.5 Linear correlations

Linear correlations indicate the degree of association between two sets of data. To be more precise, they depict the strength of linear relationship between two variables. In this thesis, we employ the Pearson correlation to compute a coefficient r. We use the Python module "scipy" to produce these coefficients [Scipy, 2022]. The coefficient values are real and range from -1 to 1, with -1 indicating a perfect negative linear relationship and 1 representing a perfect positive linear relationship. Given two sets of data x and y, their Pearson correlation coefficient r is computed as follows:

$$r = \frac{\sum_{i=1}^{N}(x_i - \overline{x})(y_i - \overline{y})}{\sqrt{\sum_{i=1}^{N}(x_i - \overline{x})^2}\sqrt{\sum_{i=1}^{N}(y_i - \overline{y})^2}},$$

where N is the data sample size, x_i are the values of x, $\overline{x}$ is the mean of x, y_i are the values of y and $\overline{y}$ is the mean of y. A significance level of 99% (p-value ≤ 0.01) is chosen in this work. The null hypothesis test assumes a normal distribution for both variables. Finally, it is important to explain how correlation maps are produced. For two sets of data of size $(i \times j \times n)$, with $m = i \times j$ being the number of grid points, and n being the number of time iterations, the Pearson correlation coefficients and associated p-values are calculated in all grid-cells between the two sets of data. This results in a spatial distribution of Pearson correlation coefficients r, with the regions associated with the significant correlations being displayed. Correlation maps allow us to understand the relationship between two variables during a time span $t = dt \times n$ and how these relationships vary in space. In this thesis, correlation maps are employed for quantitative purposes as to compute the regional mean correlations involving various variables. Having said that, it is important to recall that correlations between two variables do not necessarily indicate a causation. The underlying mechanisms must therefore be addressed to determine whether such a causation is present, if it is not or if we do not know. It is also important to mention that a positive or negative correlation between two variables, even if significant, does not necessarily indicate a similar or opposite trend, respectively. For instance, a positive correlation between the SIV and AO index does not necessarily mean that an increase of the index is associated with an increase of the SIV. We therefore additionally compute the difference between the mean value of the variable during the positive and negative phase of the various MOVs.

3.6 Wavelet analysis

The temporal analysis is performed via wavelet analysis. This method produces a wavelet power spectrum (WPS) that depicts the frequencies affecting the time series at distinct time spans. Various mathematical tools can be employed to analyse a time series in terms of identifying significant variabilities. The wavelet analysis was chosen because of the non-stationarity of the signals composing the various time series analysed in this study. Wavelet analysis involves many steps including the computation of the WPS, identification of the cone of influence and significant peaks of variability. To calculate the WPS, we first need to determine the wavelet transform (WT) for each iteration of the time series. The value of the WT depends on the wavelet function used. Various functions exist [Fig. 3.2], and the choice depends on multiple factors, including its shape, orthogonality, and whether the function is real or complex [Torrence and Compo, 1998]. In this work, we utilise the Morlet function. The choice is justified by its vast use in geophysical settings such as the one

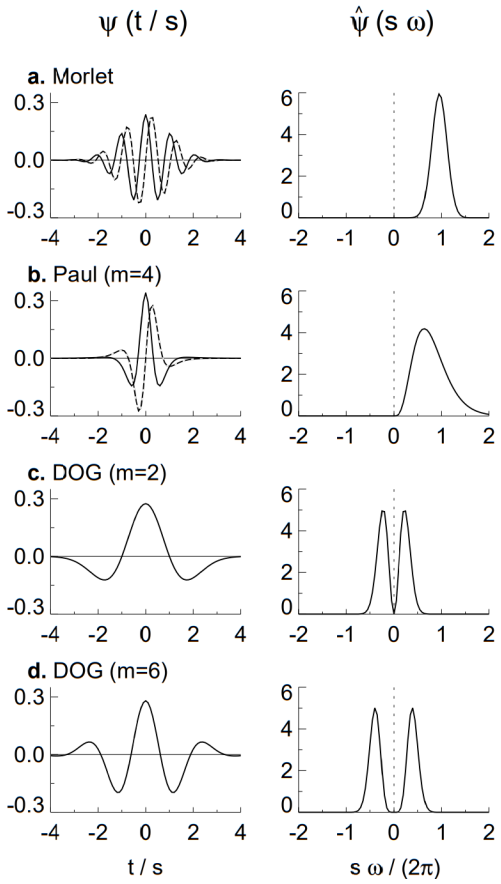


Fig. 3.2 – Examples of different wavelet functions. Left plots shows the real part (solid) and imaginary part (dashed) of the wavelet functions in the time domain. Right plots show the wavelet functions in the frequency domain. Figure is from Torrence and Compo [1998].

being studied here, as the shape of the Morlet function is similar to this kind of data [Wilks, 2011]. The set of scales being used must all be chosen. The scale is directly related with the period of the variability, and their relationship depends on the wavelet function employed. In our case, this relationship is as follows Torrence and Compo [1998]:

$$\lambda(s) = \frac{4\pi s}{\omega_0 + \sqrt{2 + \omega_0^2}},$$

with λ the Fourier wavelength, s the scale and ω_0 the frequency associated with the Morlet function ($\omega_0 = 6$ in our case). Here, we have a relation of $\lambda = 1.03s$ and, consequently, the scales and periods are strongly related. The WT is calculated for many scales. A minimum scale s_0 must be specified to produce the required set of scales following Eq. 3.1 [Torrence and Compo, 1998].

$$\begin{cases} s_j = s_0 2^{j\delta j} \quad j = 0, 1, ..., J \\ \\ J = \delta j^{-1} \log_2 (N\delta t / s_0), \end{cases} \tag{3.1}$$

where J is the iteration of the largest scale, δt is the time interval between each time series value, N is the total amount of values in the time series and δj determines the difference between s_0 and the highest scale,

while also controlling the space between each element of the set. For the Morlet function, a δj of about 0.5 is the largest value that still gives adequate sampling in scale [Torrence and Compo, 1998]. In our case, we choose a value $s_0 = 3$ years and $\delta j = 0.01$. The choice of s_0 is justified by the 3-year moving average applied on the data, which removes any variability of a period lower than 3 years. The value $\delta j = 0.01$ is used to achieve a high resolution in the computed WPSs. As a matter of fact, the lower δj, the higher the resolution in the frequency space, but the computational cost is increased. After selecting the wavelet function and scales, we can finally compute the WT of a discrete sequence x_n, as demonstrated by Torrence and Compo [1998]:

$$W_n(s) = \sum_{n'=0}^{N-1} x_{n'} \Psi^* \left[\frac{(n'-n)\delta t}{s} \right], \tag{3.2}$$

where n is the time iteration, x_n are the values of the time series and Ψ^* is the complex conjugate of the normalised wavelet function Ψ, given as follows [Torrence and Compo, 1998]:

$$\Psi \left[\frac{(n'-n)\delta t}{s} \right] = \left(\frac{\delta t}{s} \right)^{\frac{1}{2}} \Psi_0 \left[\frac{(n'-n)\delta t}{s} \right],$$

where Ψ_0 is the Morlet function in our case. Although we could determine the WT using Eq. 3.2, the calculation is faster in the Fourier space. For this, we need the discrete Fourier transform of x_n, given in Eq. 3.3, and the Fourier transform $\hat{\Psi}$ of Ψ.

$$\hat{x}_k = \frac{1}{N} \sum_{n=0}^{N-1} x_n e^{-2\pi i k n / N}, \tag{3.3}$$

where k is the frequency index. The resulting continuous WT in the Fourier space is [Torrence and Compo, 1998]:

$$W_n(s) = \sum_{k=0}^{N-1} \hat{x}_k \hat{\Psi}^*(s\omega_k) e^{i\omega_k n \delta t},$$

where ω_k is the angular frequency. Furthermore, we require the WT for every scale previously defined. The WPS is then computed with $|W_n(s)|^2$. Once the WPS is determined, the cone of influence must be calculated and represented. If the support of the wavelet function, for a given scale and time iteration, is not a subset of the time series domain, then the associated region in the WPS is deemed unreliable. The larger the scale, the more prevalent this problem becomes. The region of the WPS hindered by this issue is called the "cone of influence" and is depicted by a hatched region in the plots. We may also calculate the WPS time-mean to produce the global power spectrum. This power spectrum shows the overall importance of the signals across the entire time domain.

Finally, not every peak found in the WPS is "significant". The peaks of variability can be a result of the randomness of the background noise. To differentiate noise from signal, we need to model the background noise and then apply a null hypothesis test, to discern the "significant" from noisy peaks. In this study, we represent the background noise as red noise. We use the univariate lag-1 autoregressive equation [Eq. 3.4] to model this red noise [Torrence and Compo, 1998]:

$$x_n = \alpha x_{n-1} + z_n, \tag{3.4}$$

with x_n the simulated time series for the red noise, α the lag-1 autocorrelation and z_n a random value taken from a Gaussian distribution. Here, we utilise a value $\alpha = 0.72$ as in Torrence and Compo [1998]. After simulating a red noise time series provided by Eq. 3.4, we deduce its associated normalised discrete Fourier power spectrum (FPS) given by Eq. 3.5 [Torrence and Compo, 1998]:

$$P_k = \frac{1-\alpha^2}{1+\alpha^2-2\alpha\cos\left(2\pi k/N\right)}. \tag{3.5}$$

We repeat this process a large amount of times to generate a mean FPS of the red noise. This power spectrum is low for high frequencies but increases for the lower frequencies. It is different from the mean white noise FPS that is constant with respect to the frequencies. The reason for the choice of the red noise model is due to the usual background noises found in climatic FPSs. Most climate variables tend to show an increase in background noise as frequencies decrease, similar to the form of the red noise mean FPS, hence justifying the choice of the model. With the red noise mean power spectrum, we can conduct a null hypothesis test to find the "significant" peaks. Given the mean FPS of the red noise, we assume that any peak that is above its 99% confidence level is "significant" and thus related to a signal. In our study, we utilise the Python module "pycwt" to compute all of the previous steps [PyCWT, 2022].

3.7 Definitions of the indices

The MOVs indices used in this study are based on the ERA-20C atmospheric reanalysis data [ECMWF, 2016]. The AO and NAO indices are given by the normalised PC of the first EOF mode of the SP anomalies poleward of 20°N and over the region 20°N-90°N, 80°W-40°E, respectively, from mid-1902 to mid-2009. The PDO is provided by the normalised PC of the first EOF mode of the SST anomalies over the region 20°N-67°N, 100°E-100°W during the same time frame. The NPO and AMO indices are constructed by calculating the normalised area-weighted mean SP anomalies over the region 30°N-65°N,160°E-140°W and SST anomalies over the North Atlantic Ocean, respectively, spanning from mid-1902 to mid-2009. The NPO index is multiplied by -1, with the intent that NPO+ depicts a deeper AL.

For the temporal analysis, we introduce 4 more indices: the regional SIV (RSIV), SIM flux (RSIMF), SAT (RSAT) and SST (RSST). The RSIV is based on the normalised regional total SIV anomaly. The SIV anomalies, corresponding to all grid-cells contained in the region, are summed to produce the regional total SIV time series. The RSIMF is given by the normalised regionally integrated SIM divergence field anomaly. Hence, this index depicts the evolution of the total SIM border flux anomaly for a given region. Finally, the RSAT and RSST are built by computing the normalised regional area-weighted mean SAT and SST anomalies, respectively. It must be specified that only the grid-cells where sea ice is present (SIC > 0), at a given point in time, are taken into account for the RSAT and RSST computations. Thus, the RSAT and RSST are only defined by the SATs and SSTs directly affecting the regional SIV. These indices consequently describe the evolution of the mean SAT and SST anomalies, where sea ice exists, in a given region. All indices span from mid-1902 to mid-2009 and are normalised by their own standard deviation.

Chapter 4

Results and discussion

In this chapter, we analyse the effects on the Arctic SIV imposed by the SIM, SAT and SST shifts associated with the MOVs. First, an analysis of the results is performed spatially, where the dynamic and thermodynamic impacts are evaluated regionally, and an explanation of their origin is given. Following this, a wavelet analysis is performed to identify the main time periods of influence of the MOVs and their corresponding frequency. Finally, the lag-times between the MOVs and their impacts on the regions SIV is determined.

4.1 Spatial analysis

In this section, the dynamics-induced regional effects are studied by computing the SIM divergence fields, but their driving factors are explained as well. The mean SP, 10-m wind and SIM spatial patterns, related to the various MOVs phases, are provided to unveil the origin of the SIM divergence alterations. Instead, the thermodynamic influence is analysed by comparing the SAT and SST patterns, while their triggering mechanisms are illustrated via the use of the SP and 10-m wind fields, but the ITEFD and SSHF spatial distributions are utilised as well.

4.1.1 Arctic Oscillation and North Atlantic Oscillation

The mean Arctic SIV anomalies fluctuation between the phases of the AO and NAO are shown in Figs. 4.1a and 4.1b. A noticeable dipole, between the North American and Eurasian hemispheres, associated with the NAO is visible. Such a dipole is less noticeable for the AO, although similarities between the two maps are still present. The resemblance is explained by the important relationship between the two MOVs. This can be understood when examining the SP patterns of both MOVs [Figs. 4.2a, 4.2b, A.6a and A.6b], displaying a more pronounced AL and BH during their positive phase, while a deeper IL is noticeable in the negative phase. As a result of this relationship, the AO and NAO indices are significantly correlated at $r = 0.77$.

As depicted in Table 4.1, important regional decreases of SIV from the negative to positive phase of both MOVs take place in the East Siberian Sea, Laptev Sea, Barents Sea and Sea of Okhotsk. Meanwhile, the opposite is true in the Beaufort Sea and Baffin Bay/Labrador Sea. Important changes are also present for the AO or NAO, but not both, in the Chukchi Sea, Canadian Archipelago, Hudson Bay and Bering Sea. These results set forth a plausible relevant regional impact driven by the AO and NAO. However, to confirm such conclusions, the underlying mechanisms must be addressed.

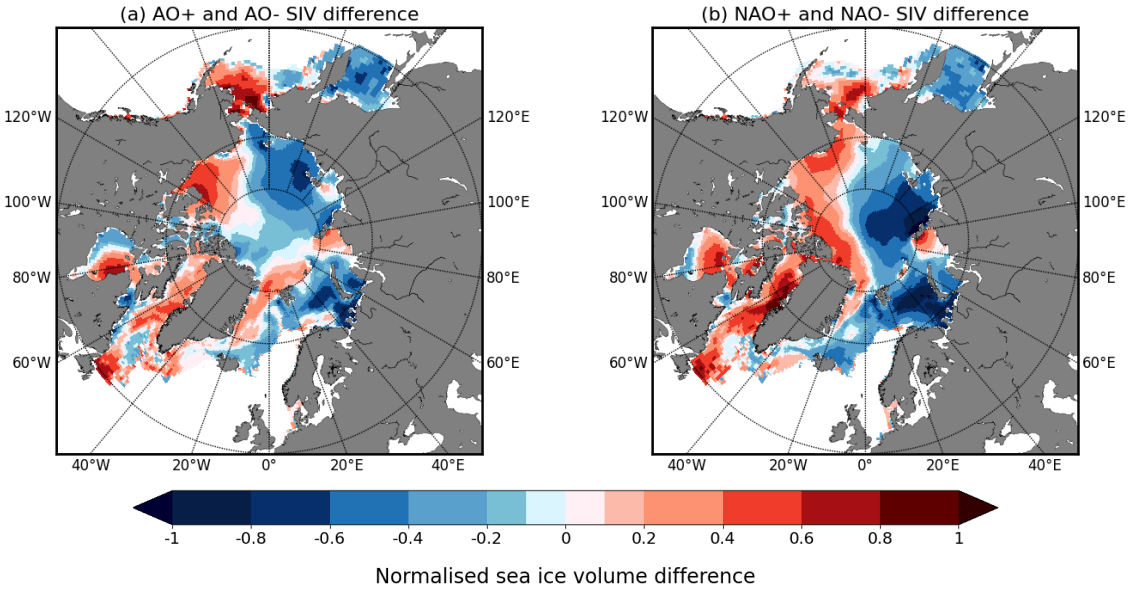


Fig. 4.1 – Difference in the mean of the PIOMAS-20C normalised SIV, from mid-1902 to mid-2009, between (a) AO+ and AO-, (b) NAO+ and NAO-. The SIV time series of all grid-cells employed are normalised by their own standard deviation as to represent the relative impacts.

Table 4.1 – Regional sum of the mean SIV absolute difference between the AO phases (AO+ - AO- SIV) and between the NAO phases (NAO+ - NAO- SIV), regional sum of the mean SIV difference between the AO phases and between the NAO phases relative to the regionally summed SIV variability and the area-weighted mean Pearson correlation coefficient (r) between the PIOMAS-20C SIV anomalies and the AO/NAO indices for each region. The relative SIV difference is computed by dividing the absolute value of the SIV difference with the 2 standard deviation of the regionally summed SIV time series. Values on the left are associated with the AO and values on the right with the NAO. Significant correlations (p-value ≤ 0.01) are highlighted in bold.

Region	**Difference** $[km^3]$ **AO; NAO**	**Relative difference** [%] **AO; NAO**	r **AO; NAO**
Beaufort Sea	95.56; 82.31	20.24; 17.43	**0.31**; **0.28**
Chukchi Sea	-61.42; 30.38	15.74; 7.79	**-0.12**; 0.05
East Siberian Sea	-249.52; -112	28.03; 12.59	**-0.36**; **-0.26**
Laptev Sea	-57.33; -124.15	19.1; 41.37	**-0.25**; **-0.46**
Kara Sea	-9.34; -8.06	5.26; 4.54	-0.02; **-0.08**
Barents Sea	-35.61; -60.8	21.78; 37.19	**-0.21**; **-0.34**
Greenland Sea	10.33; -11.43	7.22; 7.98	-0.02; **-0.14**
Baffin Bay/Labrador Sea	16.52; 38.19	14.03; 32.44	**0.14**; **0.23**
Canadian Archipelago	5.5; 18.25	3.16; 10.49	**0.07**; **0.13**
Hudson Bay	6.64; 15.67	7.74; 18.26	**0.09**; **0.18**
Central Arctic	-49.16; -77.07	7.18; 11.26	0.02; -0.06
Bering Sea	13.42; 9.64	31.6; 22.71	**0.13**; 0.06
Sea of Okhotsk	-9.1; -9.24	23.81; 24.19	**-0.25**; **-0.28**

Dynamic influence

The SP and 10-m wind patterns associated with the AO- and AO+ phases are displayed in Figs. 4.2a and 4.2b. During AO-, the more intense AL and BH lead to important SP gradients between the two pressure systems over the Arctic Ocean [Fig. A.3a]. Consequently, higher 10-m wind speeds are observed over the Beaufort Sea and Chukchi Sea [Fig. A.4a]. An increase in wind speeds, although to a lesser extent, is also present over the East Siberian Sea, Laptev Sea, Kara Sea, Barents Sea, Bering Sea and Sea of Okhotsk. Instead, the shallower IL and lower AH present during the negative phase [Fig. A.1b] lead to a significant decrease of SP gradients between the two pressure systems. Consequently, weaker 10-m wind speeds over the North Atlantic Ocean are observed during AO-. The same SP gradient patterns are not observed over the North Pacific Ocean due to the less prominent North Pacific High (NPH) pressure system during the deeper AL phase.

The resulting 10-m wind changes then give rise to SIM shifts as shown in Figs. 4.2c and 4.2d. As expected, the SIM speeds across most of the Arctic Ocean and North Pacific Ocean are higher during the negative phase [Fig. A.5a], while the opposite is true in the North Atlantic Ocean. This increase is especially pronounced in the Beaufort Sea and Chukchi Sea. It is also interesting to mention the displaced Beaufort Gyre as a result of the relocated BH. To fully comprehend the impact of the AO through its associated dynamic processes, we examine the SIM divergence field results depicted in Fig. 4.2e. A prevalent SIM divergence decrease takes place in the Chukchi Sea and East Siberian Sea during AO+, as displayed in Table 4.2. These results are driven by the Beaufort Gyre displacement and the important increase in SIM from the west to the east Arctic Ocean during this phase. The more northward-positioned Beaufort Gyre, in addition to the increased SIM speed, amplifies the influx of sea ice towards the eastern Chukchi Sea. The shifted Beaufort Gyre also impedes the export of sea ice away from the East Siberian Sea by narrowing its passage north of the New Siberian Islands. As a result, an important SIM convergence takes place in these regions during AO-, thus partially explaining the SIV increase observed in Fig. 4.1a and Table 4.1. Although changes in the regional SIM border flux take place in all regions, the impacts are not felt as much. As a matter of fact, most of the dynamically driven SIV fluctuations are localised and mostly situated along the coasts. The SIV increase, during AO+, near the north-western Canadian Archipelago, western Bering Sea, southern Bering Sea and eastern Kara Sea coasts is induced by an SIM divergence decrease. Contrastingly, the SIV decline by the side of the south-western Chukchi Sea, southern East Siberian Sea, eastern Wrangel Islands, eastern New Siberian Islands, eastern Taymyr Peninsula, eastern Franz Josef Land, southern Kara Sea and southern Barents Sea coasts is influenced by an SIM divergence increase. The previous results are largely related to the 10-m wind speed drop over the Arctic Ocean and North Pacific Ocean coastal areas during AO+. The SIV decrease along the west Labrador Sea is due to an SIM divergence increase driven by the 10-m wind shifts associated with the deeper IL. The SIM changes affect the SIV evolution in the open seas as well. This can be seen in the northern Greenland Sea, parts of the Central Arctic, Kara Sea, eastern Beaufort Sea and Laptev Sea on top of the previously mentioned Chukchi Sea and East Siberian Sea.

While the SP patterns associated with the NAO are similar, differences still persist [Figs. A.6a and A.6b]. The AL and BH SP difference between NAO+ and NAO- is smaller, whereas the IL and AH SP difference is greater [Figs. A.1c and A.1d]. Consequently, the SP gradients difference over the North Pacific Ocean and Arctic Ocean is not as pronounced [Fig. A.3b]. However, the opposite is true over the North Atlantic Ocean. This leads to less noticeable alterations in the 10-m winds, and therefore SIM vector fields in the North Pacific Ocean and Arctic Ocean, while larger changes are observed in the North Atlantic Ocean as depicted in Figs. A.4b, A.5b, A.6c and A.6d. The resulting SIM divergence and regional SIM border fluxes are displayed in Fig. A.6e and Table 4.3. During NAO+, regionally prevalent SIM divergence increases are found in the Chukchi Sea, East Siberian Sea and Laptev Sea, whereas a decrease is present in the Beaufort Sea. The results in the Beaufort Sea and Laptev Sea are not as significant for the AO [Fig. 4.2e and Table 4.2]. As a consequence, the SIV increase in these regions is more widespread and larger [Fig. 4.1b and Table 4.1] during NAO+. On the other hand, the smaller overall divergence taking place in the Chukchi Sea leads to less significant impacts on the region SIV.

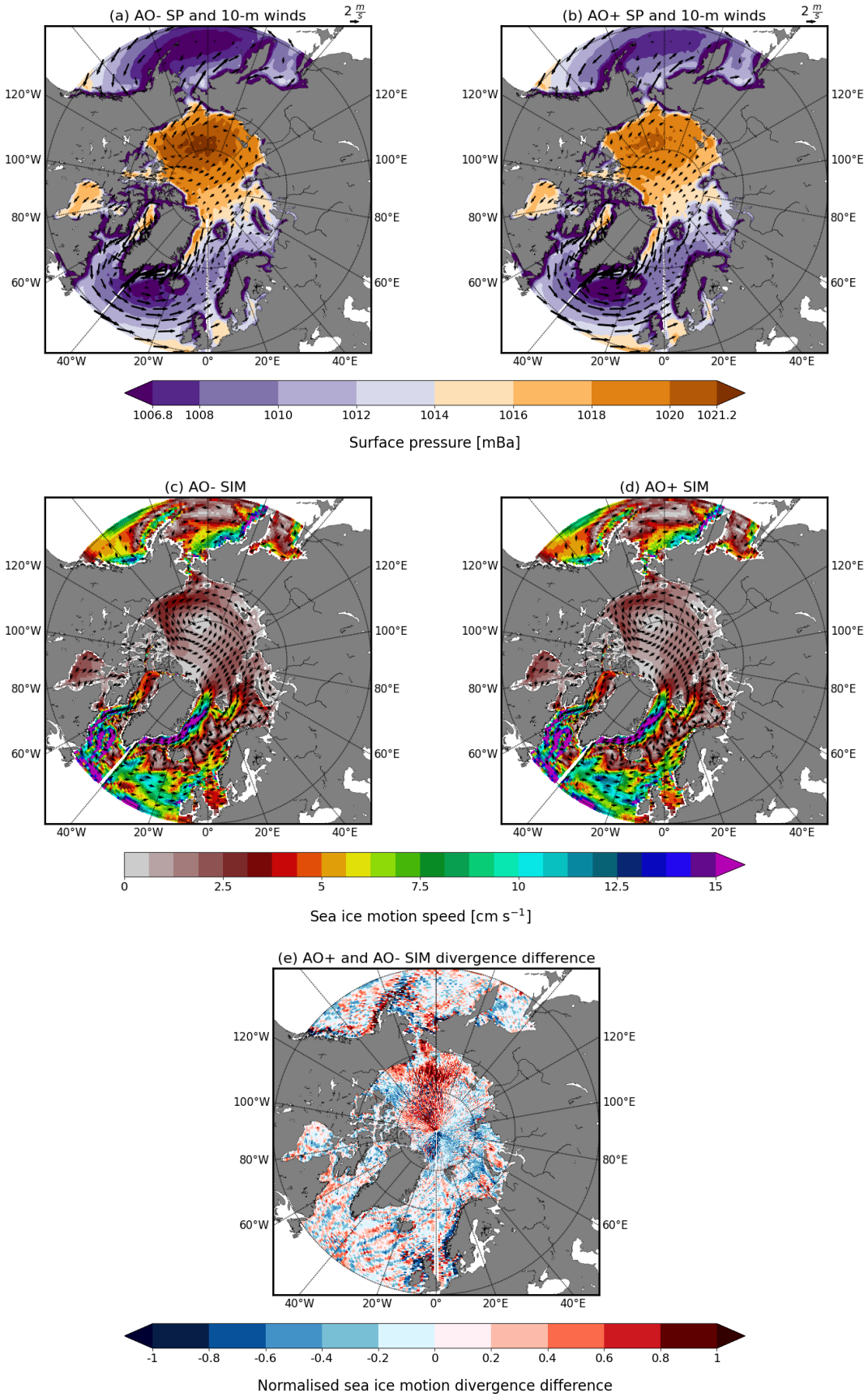


Fig. 4.2 – Dynamic processes spatial patterns associated with the AO spanning from mid-1902 to mid-2009. The ERA-20C mean SP and 10-m winds distributions during (a) AO- and (b) AO+. The PIOMAS-20C mean SIM distributions during (c) AO- and (d) AO+. (e) The difference in the mean of the computed normalised SIM divergence between AO+ and AO-. The SIM divergence time series of all grid-cells are normalised by their own standard deviation as to represent the relative impacts.

The local dynamic effects associated with the NAO are mostly explained the same way as for the AO. Nonetheless, we should point out the larger SIV decrease near the eastern coast of the Taymyr Peninsula and north of the New Siberian Islands during NAO+. This difference is driven by the greater presence of an SIM divergence increase over these areas compared to the AO.

Table 4.2 – Regional area integral of the mean SIM divergence (total SIM flux through the border) during AO- and AO+. Negative values indicate an overall influx, while positive values correspond to an overall outflux of sea ice through the border. The difference between the computed regional area integrals and the difference relative to the total regional area integral variability are also given. The relative difference is computed by dividing the absolute value of the difference with the 2 standard deviation of the total regional SIM border flux time series. Last column displays the area-weighted mean Pearson correlation coefficient (r) between the SIM divergence and the AO index for each region. Significant correlations (p-value $\leq$ 0.01) are highlighted in bold.

Region	**AO-** $[m^2/s]$	**AO+** $[m^2/s]$	**Difference** $[m^2/s]$	**Relative difference** [%]	r
Beaufort Sea	-1.88 x 10^3	-2.43 x 10^3	-5.55 x 10^2	8.22	0.01
Chukchi Sea	-1.44 x 10^4	-1.01 x 10^4	4.35 x 10^3	57.29	**0.25**
East Siberian Sea	-6.7 x 10^2	2.1 x 10^3	2.77 x 10^3	39.1	**0.16**
Laptev Sea	8.58 x 10^3	8.85 x 10^3	2.64 x 10^2	3.82	$\gtrapprox 0$
Kara Sea	1.04 x 10^4	9.14 x 10^3	-1.26 x 10^3	19.34	-0.02
Barents Sea	-4.69 x 10^3	-8.85 x 10^3	-4.16 x 10^3	27.13	-0.03
Greenland Sea	-7.18 x 10^4	-6.83 x 10^4	3.54 x 10^3	27.02	0.01
Baffin Bay/Labrador Sea	1.25 x 10^4	1.78 x 10^4	5.36 x 10^3	34.08	0.02
Canadian Archipelago	2.67 x 10^3	1.88 x 10^3	-7.86 x 10^2	34.98	-0.01
Hudson Bay	1.51 x 10^3	2.36 x 10^3	8.48 x 10^2	31.68	0.01
Central Arctic	1.78 x 10^4	1.75 x 10^4	-2.79 x 10^2	7.38	0.02
Bering Sea	6.47 x 10^3	3.19 x 10^3	-3.29 x 10^3	26.25	0.01
Sea of Okhotsk	8.84 x 10^3	7.1 x 10^3	-1.74 x 10^3	28.6	$\gtrapprox 0$

Table 4.3 – Regional area integral of the mean SIM divergence (total SIM flux through the border) during NAO- and NAO+. Negative values indicate an overall influx, while positive values correspond to an overall outflux of sea ice through the border. The difference between the computed regional area integrals and the difference relative to the total regional area integral variability are also given. The relative difference is computed by dividing the absolute value of the difference with the 2 standard deviation of the total regional SIM border flux time series. Last column displays the area-weighted mean Pearson correlation coefficient (r) between the SIM divergence and the NAO index for each region. Significant correlations (p-value ≤ 0.01) are highlighted in bold.

Region	**NAO-** $[m^2/s]$	**NAO+** $[m^2/s]$	**Difference** $[m^2/s]$	**Relative difference** [%]	r
Beaufort Sea	-1.36 x 10^3	-2.95 x 10^3	-1.59 x 10^3	23.57	**-0.09**
Chukchi Sea	-1.35 x 10^4	-1.13 x 10^4	2.22 x 10^3	29.18	**0.16**
East Siberian Sea	-3.5 x 10^2	1.6 x 10^3	1.95 x 10^3	27.53	**0.15**
Laptev Sea	7.67 x 10^3	9.81 x 10^3	2.14 x 10^3	31.04	**0.08**
Kara Sea	9.39 x 10^3	1.03 x 10^4	9.02 x 10^2	13.8	0.01
Barents Sea	-6.17 x 10^3	-7.05 x 10^3	-8.82 x 10^2	5.76	-0.01
Greenland Sea	-7.14 x 10^4	-6.9 x 10^4	2.42 x 10^3	18.52	0.01
Baffin Bay/Labrador Sea	1.05 x 10^4	1.96 x 10^4	9.14 x 10^3	58.1	0.02
Canadian Archipelago	2.38 x 10^3	2.23 x 10^3	-1.52 x 10^2	6.76	$\gtrapprox 0$
Hudson Bay	1.56 x 10^3	2.26 x 10^3	6.98 x 10^2	26.07	0.01
Central Arctic	1.81 x 10^4	1.71 x 10^4	-9.41 x 10^2	24.9	-0.01
Bering Sea	5.39 x 10^3	4.52 x 10^3	-8.79 x 10^2	7.02	0.01
Sea of Okhotsk	7.6 x 10^3	8.52 x 10^3	9.17 x 10^2	15.05	0.03

Thermodynamic influence

The 10-m wind patterns associated with AO- [Figs. 4.2a and 4.2b] increase the amount of cold northerly air masses brought over the Sea of Okhotsk and amplify the westerlies over the North Pacific Ocean. As a result, a larger ocean to atmosphere heat transfer, driven by the stronger and cold northerly 10-m winds, takes place over the Sea of Okhotsk Fig. 4.3b. Consequently, lower SSTs are observed, as shown in Fig. 4.3d. The resulting westerly winds transport the extracted heat towards the Bering Sea, thus increasing and decreasing the SATs over this region and the Sea of Okhotsk, respectively [Fig. 4.3c], although an SST increase is observed as well in the Bering Sea. A similar mechanism takes place over the North Atlantic Ocean during AO+. The stronger 10-m wind speeds [Fig. A.4a] amplify the influx of northerly cold air masses towards the Baffin Bay and Labrador Sea. Hence, a decrease of SSHF and an increase of ITEFD occurs during this phase [Figs. 4.3a and 4.3b]. The more prominent westerlies then transport the extracted heat towards the Barents Sea, therefore leading to higher SATs, although an SST increase is also present. An amplification of the AMOC, as explained by Delworth and Zeng [2016], on top of the atmosphere to ocean heat exchanges could contribute to the SST surge in the Barents Sea and parts of the Greenland Sea.

Overall, the SAT and SST spatial distributions exhibit a dipole between the North American and Eurasian hemispheres. Table 4.4 compares the regional mean SAT and SST between AO+ and AO- while also displaying the regional mean correlations. The important SAT and SST increases over the Barents Sea, Sea of Okhotsk and Laptev Sea lead to a prevalent SIV decline during AO+ [Fig. 4.1a and Table 4.1]. Contrastingly, the

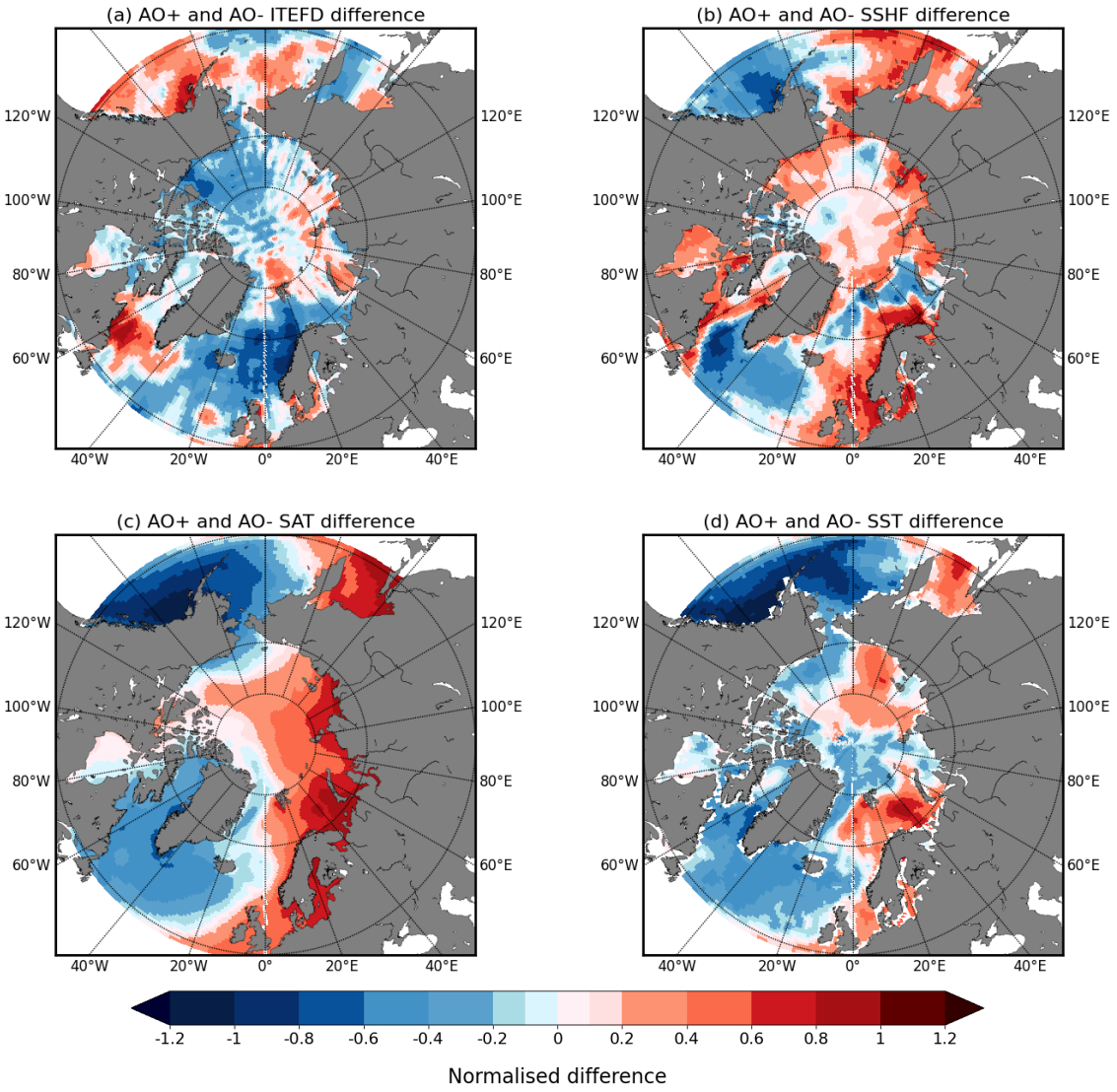


Fig. 4.3 – Difference between AO+ and AO-, from mid-1902 to mid-2009, in the mean of the ERA-20C normalised (a) ITEFD, (b) SSHF, (c) SAT and (d) SST. The various time series of all grid-cells employed are normalised by their own standard deviation as to represent the relative impacts.

lower SATs and SSTs over the Baffin Bay/Labrador Sea and Bering Sea give rise to an SIV increase.

The 10-m wind patterns associated with the NAO [Figs. A.6a and A.6b] lead to a similar SAT spatial distribution [Fig. A.7c]. Nevertheless, the ocean to atmosphere heat transfer and the following westerly atmospheric heat transport mechanism is not as pronounced over the North Pacific Ocean due to the smaller 10-m wind speeds difference between NAO+ and NAO- [Fig. A.4b]. Therefore, the SAT shifts related to the NAO are not as important over the North Pacific Ocean, while the SST changes are not as pronounced as well [Fig. A.7d]. Contrastingly, because of the more intense 10-m wind speed changes, SSHF and atmospheric heat transports from NAO+ to NAO- over the North Atlantic Ocean, the SAT and SST fluctuations are more striking [Figs. A.7a, A.7b, A.7c and A.7d]. The resulting thermodynamic impacts of the NAO on the Arctic SIV are mostly comparable to the AO. The regional influence of the SAT and SST associated with the NAO is particularly marked in the Barents Sea and Baffin Bay/Labrador Sea [Fig. 4.1b and Table 4.1], as a result of the prominent

SAT and SST increases [Table 4.5]. On the other hand, the Sea of Okhotsk and Bering Sea are not as impacted.

It is important to note that not all of the dynamic and thermodynamic processes associated with the NAO are triggered by this MOV. Since the NAO is defined by the IL and AH SP contrast, only the effects induced by the 10-m wind shifts, that are generated by these pressure systems, can be directly attributed to it. Nonetheless, possible teleconnections could uncover a causal link between the NAO and the thermodynamic and dynamic processes found in the North Pacific Ocean.

Table 4.4 – Mean SAT/SST absolute difference between the AO phases (AO+ - AO- SAT/SST), mean SAT/SST difference between the AO phases relative to the mean regional SAT/SST variability and the area-weighted mean Pearson correlation coefficient (r) between the ERA-20C SAT/SST anomalies and the AO index for each region. The relative SAT/SST difference is computed by dividing the absolute value of the SAT/SST difference with the 2 standard deviation of the mean regional SAT/SST time series. Values on the left are associated with the SAT and values on the right with the SST. Significant correlations (p-value ≤ 0.01) are highlighted in bold. Only the grid-cells where sea ice is present (SIC > 0) are used for the computation of the means. Thus, only the SATs and SSTs directly affecting the sea ice are taken into account.

Region	**Difference [K]** **SAT; SST**	**Relative difference [%]** **SAT; SST**	***r*** **SAT; SST**
Beaufort Sea	0.02; -0.01	3.28; 2.48	-0.04; **-0.1**
Chukchi Sea	-0.04; -0.02	5.98; 3.82	-0.07; **-0.09**
East Siberian Sea	0.07; 0.02	14; 3.75	**0.19**; **0.29**
Laptev Sea	0.11; $\gtrapprox$ 0	33.73; 0.61	**0.39**; **0.1**
Kara Sea	0.16; $\gtrapprox$ 0	33.81; 0.05	**0.35**; -0.04
Barents Sea	0.26; 0.06	39.03; 8.93	**0.45**; **0.28**
Greenland Sea	-0.05; -0.02	8.86; 4.72	-0.05; -0.03
Baffin Bay/Labrador Sea	-0.19; -0.06	25.65; 7.75	**-0.41**; **-0.24**
Canadian Archipelago	0.01; $\lessapprox$ 0	3.89; 0.91	**-0.1**; -0.07
Hudson Bay	-0.01; -0.01	2.96; 1.06	**-0.16**; **-0.08**
Central Arctic	0.11; $\lessapprox$ 0	16.7; 0.19	**0.16**; -0.04
Bering Sea	-0.12; -0.07	31.69; 20.02	**-0.21**; **-0.3**
Sea of Okhotsk	0.13; 0.03	37.35; 7.61	**0.42**; **0.27**

Table 4.5 – Mean SAT/SST absolute difference between the NAO phases (NAO+ - NAO- SAT/SST), mean SAT/SST difference between the NAO phases relative to the mean regional SAT/SST variability and the area-weighted mean Pearson correlation coefficient (r) between the ERA-20C SAT/SST anomalies and the NAO index for each region. The relative SAT/SST difference is computed by dividing the absolute value of the SAT/SST difference with the 2 standard deviation of the mean regional SAT/SST time series. Values on the left are associated with the SAT and values on the right with the SST. Significant correlations (p-value ≤ 0.01) are highlighted in bold. Only the grid-cells where sea ice is present (SIC > 0) are used for the computation of the means. Thus, only the SATs and SSTs directly affecting the sea ice are taken into account.

Region	**Difference [K]** **SAT; SST**	**Relative difference [%]** **SAT; SST**	r **SAT; SST**
Beaufort Sea	$\lessapprox 0; -0.02$	0.61; 17.18	0.02; **-0.19**
Chukchi Sea	-0.06; -0.05	9.83; 32.04	-0.04; **-0.22**
East Siberian Sea	0.08; 0.01	14.99; 15.17	**0.23**; **0.22**
Laptev Sea	$0.14; \gtrapprox 0$	43.68; 8.5	**0.46**; **0.11**
Kara Sea	$0.21; \lessapprox 0$	44.01; 3.45	**0.44**; -0.03
Barents Sea	0.36; 0.09	53.97; 45.99	**0.57**; **0.41**
Greenland Sea	$0.02; \lessapprox 0$	3.88; 1.88	**0.08**; **0.07**
Baffin Bay/Labrador Sea	-0.36; -0.08	50.41; 35.9	**-0.57**; **-0.31**
Canadian Archipelago	-0.04; -0.01	16.56; 19.12	**-0.2**; **-0.21**
Hudson Bay	$-0.08; \gtrapprox 0$	18.58; 2.36	**-0.3**; **-0.1**
Central Arctic	$0.28; \gtrapprox 0$	43.69; 8.11	**0.37**; **-0.08**
Bering Sea	-0.08; -0.04	21.8; 22.81	**-0.12**; **-0.14**
Sea of Okhotsk	0.08; 0.02	22.44; 18.38	**0.37**; **0.3**

4.1.2 North Pacific Oscillation and Pacific Decadal Oscillation

Similarities exist between the Arctic SIV variability related to the NPO and AO [Figs. 4.1a and 4.4a]. As a matter of fact, both MOVs are significantly correlated at $r = -0.7$, as a result of the connection between the depth of the AL and the AO/NPO [Figs. 4.2a, 4.2b, 4.5a and 4.5b]. Significant changes in SIV take place in the Beaufort Sea, Chukchi Sea, East Siberian Sea, Laptev Sea, Bering Sea and Sea of Okhotsk for the NPO, thereby hinting towards an important and widespread regional impact [Table 4.6]. However, the results found in the regions located in the North Atlantic Ocean are not as pronounced.

The spatial SIV variabilities corresponding to the NPO and PDO are alike [Figs. 4.4a and 4.4b], owing to the high correlation between these MOVs ($r = 0.67$). Such a relationship is further discussed in Newman et al. [2016]. The SIV decrease in the Bering Sea, during PDO+, is especially prominent, but an important SIV increase also takes place in the Canadian Archipelago [Fig. 4.4b and Table 4.6]. These results suggest a strong influence of the PDO in these regions. Having said that, relevant SIV changes are observed in most regions, thereby indicating a plausible impact as well.

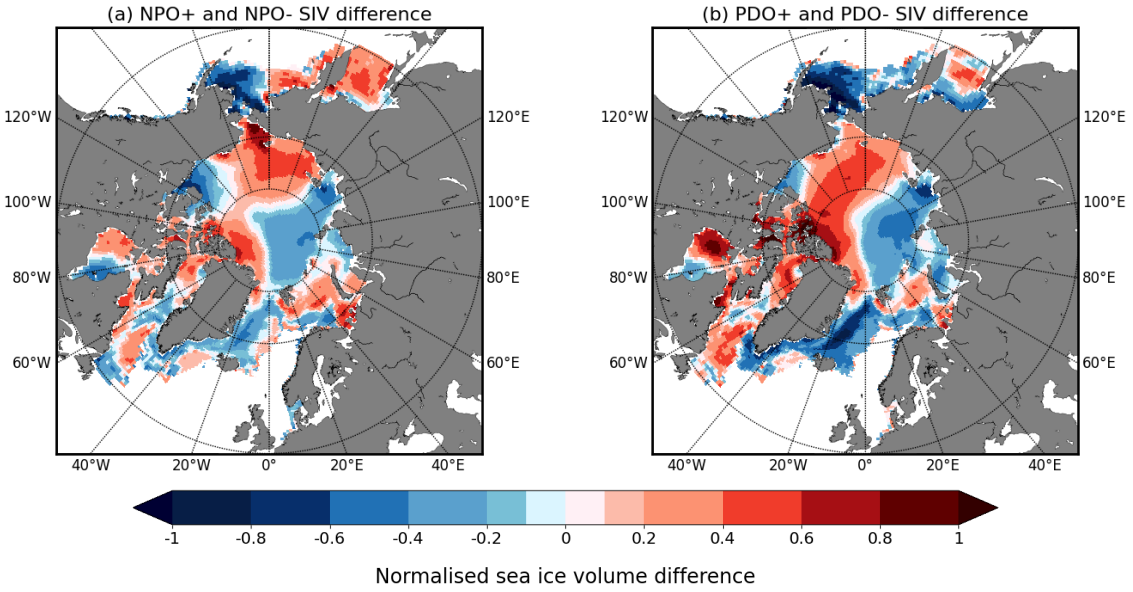


Fig. 4.4 – Difference in the mean of the PIOMAS-20C normalised SIV, from mid-1902 to mid-2009, between (a) NPO+ and NPO-, (b) PDO+ and PDO-. The SIV time series of all grid-cells employed are normalised by their own standard deviation as to represent the relative impacts.

Table 4.6 – Regional sum of the mean SIV absolute difference between the NPO phases (NPO+ - NPO- SIV) and between the PDO phases (PDO+ - PDO- SIV), regional sum of the mean SIV difference between the NPO phases and between the PDO phases relative to the regionally summed SIV variability and the area-weighted mean Pearson correlation coefficient (r) between the PIOMAS-20C SIV anomalies and the NPO/PDO indices for each region. The relative SIV difference is computed by dividing the absolute value of the SIV difference with the 2 standard deviation of the regionally summed SIV time series. Values on the left are associated with the NPO and values on the right with the PDO. Significant correlations (p-value ≤ 0.01) are highlighted in bold.

Region	**Difference** $[km^3]$ **NPO; PDO**	**Relative difference** [%] **NPO; PDO**	r **NPO; PDO**
Beaufort Sea	-33.1; 55.78	7.01; 11.81	**-0.16**; **0.1**
Chukchi Sea	105.22; 87.55	26.97; 22.44	**0.17**; **0.19**
East Siberian Sea	183.85; 117.93	20.65; 13.25	**0.18**; **0.14**
Laptev Sea	-44.68; -62.66	14.89; 20.88	**-0.16**; **-0.18**
Kara Sea	-3.15; -20.97	1.77; 11.81	$\lessapprox$ 0; **-0.09**
Barents Sea	19.91; 6.97	12.18; 4.26	$\lessapprox$ 0; 0.06
Greenland Sea	-15.13; -34.44	10.56; 24.05	-0.06; **-0.09**
Baffin Bay/Labrador Sea	11.21; 25.76	9.52; 21.89	-0.05; **0.12**
Canadian Archipelago	17.63; 72	10.13; 41.4	0.01; **0.28**
Hudson Bay	4.05; 21.89	4.72; 25.52	$\gtrapprox$ 0; **0.19**
Central Arctic	-9; 36.49	1.32; 5.33	$\gtrapprox$ 0; 0.07
Bering Sea	-11.2; -20.99	26.36; 49.42	**-0.14**; **-0.29**
Sea of Okhotsk	6.39; -3.85	16.71; 10.08	**0.08**; -0.07

Dynamic influence

The SP and 10-m wind spatial patterns corresponding to NPO+ and NPO- are displayed in Figs. 4.5a and 4.5b. The positive phase is associated with a deep AL, an intense BH and a slightly shallower IL. As a consequence, the steeper SP gradients lead to important 10-m wind speeds between the AL and BH [Figs. A.3c and A.4c]. Instead, the 10-m winds over the North Atlantic Ocean are marginally weaker, because of the smaller SP gradients. The resulting SIM vector fields are shown in Figs. 4.5c and 4.5d. The SIM speeds in the Arctic Ocean and North Pacific Ocean are mostly higher during NPO+, when the AL and BH are more pronounced [Fig. A.5c]. Inversely, the SIM speeds are slightly lower in the North Atlantic Ocean, as a result of the weaker 10-m wind speeds.

The SIM divergence shifts between NPO+ and NPO-, the corresponding regional mean correlations and the regional SIM border fluxes are given in Fig. 4.5e and Table 4.7. The regional SIM border flux shifts are especially pronounced in the Chukchi Sea, although important changes are also found in other regions. The influence of the dynamic processes in the East Siberian Sea and Laptev Sea is relevant and explains in part the results found in Fig. 4.4a and Table 4.6. The prevalent SIM divergence decrease in the Chukchi Sea, during NPO+, explains the pronounced SIV increase. More localised effects are also felt along various coasts. The SIV growth by the side of the south-western Chukchi Sea, northern Greenland, south-western Kara Sea and western Labrador Sea coasts is driven by an SIM divergence decline. Instead, the SIV decrease along the western Bering Sea, northern Bering Sea, northern Sea of Okhotsk, north-eastern Kara Sea and north-western Canadian Archipelago coasts is caused by an SIM divergence increase. The dynamic processes taking place near the Wrangel Island, New Siberian Islands and Franz Josef Land are the same as for the AO/NAO, with an SIM divergence decrease towards the eastern coasts and increase along the western coasts during the more intense AL and BH phase.

The PDO+ and PDO- SP and 10-m wind fields are displayed in Figs. A.8a and A.8b. These SP, and consequently 10-m wind patterns, are akin to the NPO [Figs. 4.5a and 4.5b], with a deep AL, elevated BH and slightly shallower IL, noticeable during PDO-. However, the difference in the depth of the AL between the two phases is smaller. This leads to a smaller SP gradient contrast between the AL and BH [Fig. A.3d], and thus the shift in 10-m wind speeds is less striking [Fig. A.4d]. The induced SIM vector fields are shown in Figs. A.8c and A.8d. The SIM speed changes across the Arctic Ocean and North Pacific Ocean are weaker than for the NPO [Fig. A.5d]. This is especially the case in the Beaufort Sea and Chukchi Sea, where the significant strengthening of the sea ice transport associated with the NPO [Fig. A.5c], from the western to the eastern Arctic Ocean, is not as prominent for the PDO.

The resulting SIM divergence shifts are illustrated in Fig. A.8e. Significant changes are found in the Chukchi Sea and Laptev Sea [Table 4.8]. These results explain the SIV increase and decrease in the Chukchi Sea and Laptev Sea, respectively, during PDO+ [Fig. 4.4b and Table 4.6]. The SIV increase across parts of the Beaufort Sea, Central Arctic, Chukchi Sea and to a lesser extent, East Siberian Sea is driven by a pronounced presence of SIM divergence decline in these areas. The SIM divergence increase in the Sea of Okhotsk causes, to a certain extent, the SIV drop found in this region. Finally, more localised effects driven by the PDO-related dynamic processes are similar to the NPO. However, because of the smaller sea ice transport shifts over the Arctic Ocean, these local impacts are not felt as much.

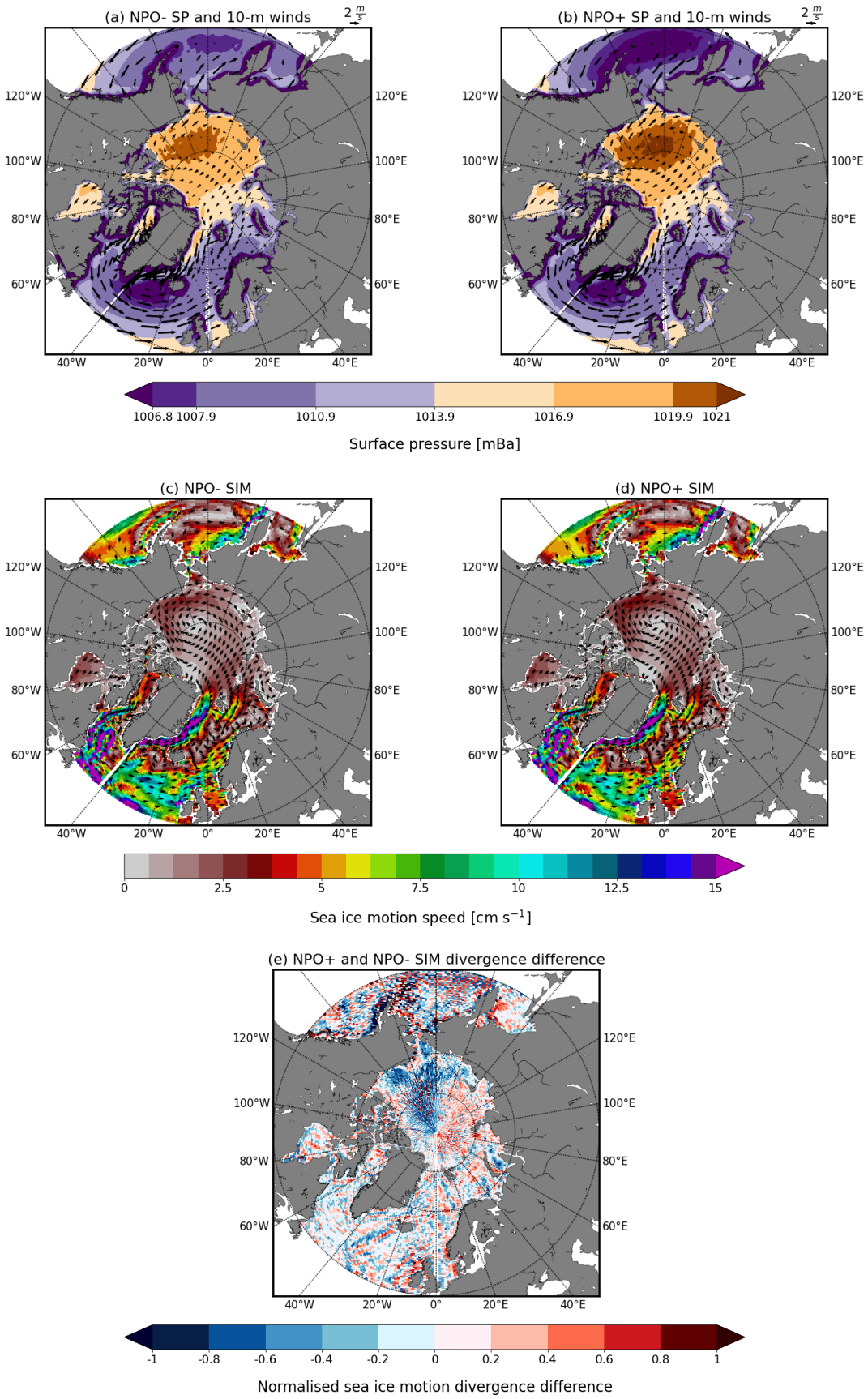


Fig. 4.5 – Dynamic processes spatial patterns associated with the NPO spanning from mid-1902 to mid-2009. The ERA-20C mean SP and 10-m winds distributions during (a) NPO- and (b) NPO+. The PIOMAS-20C mean SIM distributions during (c) NPO- and (d) NPO+. (e) The difference in the mean of the computed normalised SIM divergence between NPO+ and NPO-. The SIM divergence time series of all grid-cells are normalised by their own standard deviation as to represent the relative impacts.

Table 4.7 – Regional area integral of the mean SIM divergence (total SIM flux through the border) during NPO- and NPO+. Negative values indicate an overall influx, while positive values depict an overall outflux of sea ice through the border. The difference between the computed regional area integrals and the difference relative to the total regional area integral variability are also given. The relative difference is computed by dividing the absolute value of the difference with the 2 standard deviation of the total regional SIM border flux time series. Last column displays the area-weighted mean Pearson correlation coefficient (r) between the SIM divergence and the NPO index for each region. Significant correlations (p-value $\leq$ 0.01) are highlighted in bold.

Region	**NPO-** $[m^2/s]$	**NPO+** $[m^2/s]$	**Difference** $[m^2/s]$	**Relative difference** [%]	r
Beaufort Sea	-1.66 x 10^3	-2.54 x 10^3	-8.73 x 10^2	12.92	-0.07
Chukchi Sea	-1.04 x 10^4	-1.42 x 10^4	-3.84 x 10^3	50.51	**-0.15**
East Siberian Sea	1.18 x 10^3	9.4 x 10	-1.09 x 10^3	15.39	-0.04
Laptev Sea	7.97 x 10^3	9.34 x 10^3	1.37 x 10^3	19.89	0.07
Kara Sea	9.07 x 10^3	1.05 x 10^4	1.4 x 10^3	21.42	0.01
Barents Sea	-7.72 x 10^3	-5.63 x 10^3	2.1 x 10^3	13.68	0.01
Greenland Sea	-6.93 x 10^4	-7.1 x 10^4	-1.7 x 10^3	12.99	-0.01
Baffin Bay/Labrador Sea	1.63 x 10^4	1.37 x 10^4	-2.54 x 10^3	16.12	-0.01
Canadian Archipelago	1.87 x 10^3	2.69 x 10^3	8.2 x 10^2	36.49	0.02
Hudson Bay	2.22 x 10^3	1.62 x 10^3	-5.96 x 10^2	22.26	-0.01
Central Arctic	1.77 x 10^4	1.76 x 10^4	-9.23 x 10	2.44	-0.02
Bering Sea	3.15 x 10^3	6.52 x 10^3	3.37 x 10^3	26.92	-0.01
Sea of Okhotsk	6.39 x 10^3	9.46 x 10^3	3.07 x 10^3	50.36	0.04

Table 4.8 – Regional area integral of the mean SIM divergence (total SIM flux through the border) during PDO- and PDO+. Negative values indicate an overall influx, while positive values depict an overall outflux of sea ice through the border. The difference between the computed regional area integrals and the difference relative to the total regional area integral variability are also given. The relative difference is computed by dividing the absolute value of the difference with the 2 standard deviation of the total regional SIM border flux time series. Last column displays the area-weighted mean Pearson correlation coefficient (r) between the SIM divergence and the PDO index for each region. Significant correlations (p-value $\leq$ 0.01) are highlighted in bold.

Region	**PDO-** $[m^2/s]$	**PDO+** $[m^2/s]$	**Difference** $[m^2/s]$	**Relative difference** [%]	r
Beaufort Sea	-1.66 x 10^3	-2.68 x 10^3	-1.02 x 10^3	15.06	-0.07
Chukchi Sea	-1.15 x 10^4	-1.36 x 10^4	-2.12 x 10^3	27.86	**-0.07**
East Siberian Sea	4.93 x 10^2	7.18 x 10^2	2.25 x 10^2	3.18	0.01
Laptev Sea	7.64 x 10^3	9.95 x 10^3	2.32 x 10^3	33.57	**0.09**
Kara Sea	9.22 x 10^3	1.05 x 10^4	1.32 x 10^3	20.22	0.01
Barents Sea	-6.47 x 10^3	-6.74 x 10^3	-2.75 x 10^2	1.8	0.01
Greenland Sea	-6.92 x 10^4	-7.14 x 10^4	-2.19 x 10^3	16.72	$\lessapprox 0$
Baffin Bay/Labrador Sea	1.55 x 10^4	1.43 x 10^4	-1.16 x 10^3	7.37	-0.01
Canadian Archipelago	2.21 x 10^3	2.42 x 10^3	2.08 x 10^2	9.26	0.01
Hudson Bay	2.14 x 10^3	1.62 x 10^3	-5.24 x 10^2	19.57	0.01
Central Arctic	1.81 x 10^4	1.71 x 10^4	-1.03 x 10^3	27.21	-0.02
Bering Sea	3.53 x 10^3	6.65 x 10^3	3.12 x 10^3	24.91	-0.01
Sea of Okhotsk	6.8 x 10^3	9.51 x 10^3	2.71 x 10^3	44.41	0.04

Thermodynamic influence

As a result of the greater influx of northerly cold winds towards the Sea of Okhotsk during NPO+ [Figs. 4.5b and A.4c], the ocean to atmosphere heat transfer and following westerly atmospheric heat transport mechanism, already discussed for the AO/NAO, takes place over the North Pacific Ocean [Figs. 4.6a and 4.6b]. Hence, higher SATs are observed over the Bering Sea, but an increase in the SSTs is noticeable as well, whereas the opposite is true over the Sea of Okhotsk, as shown in Figs. 4.6c and 4.6d. During NPO-, the slightly more pronounced SP gradients over the North Atlantic Ocean lead to a marginal growth in the influx of northerly cold air masses towards the Baffin Bay and Labrador Sea [Fig. A.3c]. Consequently, the same heat transport mechanism occurs over the North Atlantic Ocean, although to a lesser degree due to the weaker 10-m wind speeds increase [Fig. A.4c]. Therefore, the SATs and SSTs over the Baffin Bay and Labrador Sea are mostly lower during NPO-, while they are mostly higher over the Barents Sea. The lower SATs

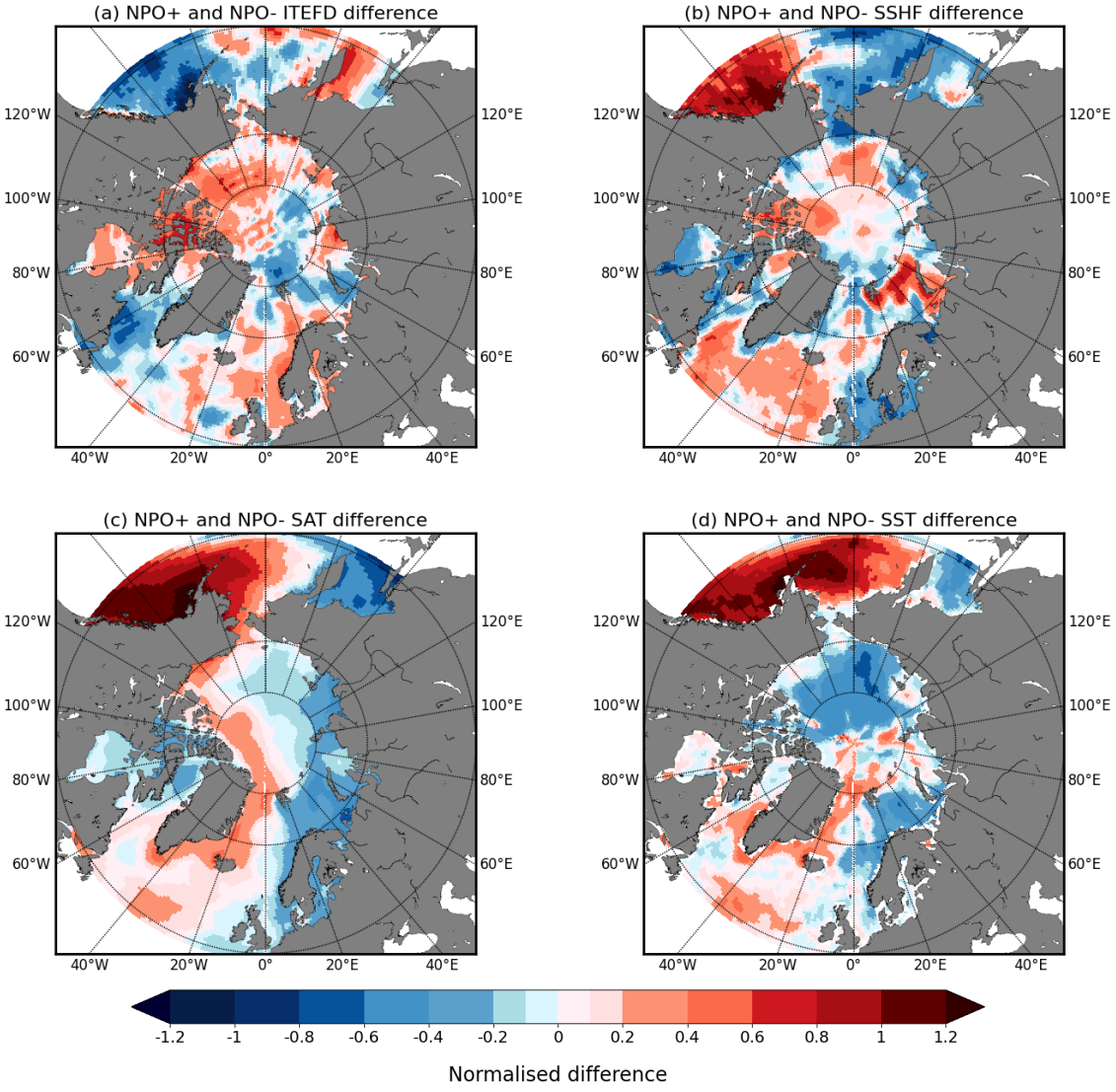


Fig. 4.6 – Difference between NPO+ and NPO-, from mid-1902 to mid-2009, in the mean of the ERA-20C normalised (a) ITEFD, (b) SSHF, (c) SAT and (d) SST. The various time series of all grid-cells employed are normalised by their own standard deviation as to represent the relative impacts.

and SSTs over the Greenland Sea seem to be driven by an intensification of the northerly cold air masses influx.

The prevalent SAT and SST decline over the Barents Sea and Sea of Okhotsk, during NPO+ [Table 4.9], results in a widespread SIV growth [Fig. 4.4a and Table 4.6]. On the other hand, the SAT and SST increases over the Greenland Sea and Bering Sea induce an SIV decrease. Although SAT and SST drops take place over the Laptev Sea, an SIV decrease is still observed due to the important regional dynamic impacts in this region [Table 4.7]. The East Siberian Sea SIV growth is driven by a combination of the SIM divergence and SAT and SST shifts, where in the east, the SIM divergence decrease and lower SSTs overwhelm the higher SATs, whereas in the west, the lower SSTs seem to lead to the observed SIV increase.

An increase in SST is present in the Bering Sea, during PDO+ [Fig. A.9d], as defined by the PDO. Nonetheless, the same SSHF and atmospheric heat transport mechanism is observed over the North Pacific Ocean as a result of the more important 10-m wind speeds during PDO+ [Figs. A.4d, A.9a and A.9b]. Consequently, the SATs over the Bering Sea are higher during this phase [Fig. A.9c], although a widespread ocean to atmosphere heat transfer intensification is noticeable as well. The PDO does not display an SAT and SST dipole between the west and east North Atlantic Ocean such as observed for the other MOVs, thus suggesting a weaker influence of the westerly atmospheric heat transport process. The SAT and SST distributions over the Arctic Ocean are mostly similar for the NPO and PDO.

Although differences in the thermodynamic impacts driven by the PDO and NPO exist, both MOVs display similar results. The higher SSTs and SATs over the Bering Sea, during PDO+ [Table 4.10], lead to an intense SIV reduction as shown in Fig. 4.4b and Table 4.6. Instead, the prevalent SAT and SST decreases over the Canadian Archipelago and Hudson Bay induce an SIV increase. The SIV drop in the Kara Sea is caused by an SST increase, while, along the northern coast of the Sea of Okhotsk, the SIV decrease is partially triggered by greater SSTs, although dynamic impacts are observed along the same coast as well [Fig. A.8e]. We should also mention the SIV growth in the northern Beaufort Sea, and the overall lesser prevalence of SIV decrease in the same region. This result is in part brought about by the larger SST decline during PDO+.

Let us recall that the NPO and PDO are defined by the AL depth and SST anomalies spatial patterns over the North Pacific Ocean, respectively. Consequently, the NPO/PDO-associated impacts on the SIV across the North Atlantic Ocean are, for the most part, not directly driven by these MOVs.

Table 4.9 – Mean SAT/SST absolute difference between the NPO phases (NPO+ - NPO- SAT/SST), mean SAT/SST difference between the NPO phases relative to the mean regional SAT/SST variability and the area-weighted mean Pearson correlation coefficient (r) between the ERA-20C SAT/SST anomalies and the NPO index for each region. The relative SAT/SST difference is computed by dividing the absolute value of the SAT/SST difference with the 2 standard deviation of the mean regional SAT/SST time series. Values on the left are associated with the SAT and values on the right with the SST. Significant correlations (p-value ≤ 0.01) are highlighted in bold. Only the grid-cells where sea ice is present (SIC > 0) are used for the computation of the means. Thus, only the SATs and SSTs directly affecting the sea ice are taken into account.

Region	**Difference [K]** **SAT; SST**	**Relative difference [%]** **SAT; SST**	$\boldsymbol{r}$ **SAT; SST**
Beaufort Sea	0.05; -0.01	10.04; 1.12	**0.18**; **-0.09**
Chukchi Sea	0.02; -0.02	3.5; 2.79	**0.16**; **-0.11**
East Siberian Sea	-0.03; -0.02	6.29; 4.49	0.07; **-0.19**
Laptev Sea	-0.05; $\lessapprox 0$	15.73; 0.74	**-0.1**; **-0.08**
Kara Sea	-0.06; $\lessapprox 0$	12.85; 0.58	**-0.13**; -0.01
Barents Sea	-0.13; -0.04	20.08; 5.68	**-0.17**; **-0.07**
Greenland Sea	0.08; 0.02	15.53; 4.35	**0.16**; **0.14**
Baffin Bay/Labrador Sea	0.01; 0.01	0.99; 1.95	**0.11**; **0.14**
Canadian Archipelago	-0.01; $\lessapprox 0$	3.39; 1.22	0.05; -0.06
Hudson Bay	-0.03; $\gtrapprox 0$	6.28; 0.82	-0.05; 0.05
Central Arctic	0.02; $\gtrapprox 0$	3.65; 0.09	**0.15**; -0.04
Bering Sea	0.1; 0.07	28.13; 19.96	**0.27**; **0.34**
Sea of Okhotsk	-0.11; -0.02	31.85; 5.54	**-0.27**; **-0.17**

Table 4.10 – Mean SAT/SST absolute difference between the PDO phases (PDO+ - PDO- SAT/SST), mean SAT/SST difference between the PDO phases relative to the mean regional SAT/SST variability and the area-weighted mean Pearson correlation coefficient (r) between the ERA-20C SAT/SST anomalies and the PDO index for each region. The relative SAT/SST difference is computed by dividing the absolute value of the SAT/SST difference with the 2 standard deviation of the mean regional SAT/SST time series. Values on the left are associated with the SAT and values on the right with the SST. Significant correlations (p-value ≤ 0.01) are highlighted in bold. Only the grid-cells where sea ice is present (SIC > 0) are used for the computation of the means. Thus, only the SATs and SSTs directly affecting the sea ice are taken into account.

Region	**Difference [K]** **SAT; SST**	**Relative difference [%]** **SAT; SST**	$\boldsymbol{r}$ **SAT; SST**
Beaufort Sea	0.04; -0.01	9.58; 2.47	**0.09**; **-0.2**
Chukchi Sea	0.1; -0.01	17.19; 2.07	**0.15**; **-0.18**
East Siberian Sea	0.02; -0.01	4.02; 2.11	0.07; **-0.13**
Laptev Sea	-0.04; $\lessapprox 0$	12.07; 0.04	**-0.09**; -0.07
Kara Sea	-0.01; 0.01	2.21; 2.8	-0.04; **0.11**
Barents Sea	-0.08; -0.03	12.38; 3.93	**-0.18**; **-0.15**
Greenland Sea	0.16; 0.04	30.54; 8.32	**0.17**; **0.09**
Baffin Bay/Labrador Sea	-0.07; $\lessapprox 0$	9.78; 0.06	**-0.07**; -0.04
Canadian Archipelago	-0.03; -0.01	12.6; 2.71	-0.07; **-0.22**
Hudson Bay	-0.13; -0.02	27.88; 3.2	**-0.29**; **-0.15**
Central Arctic	0.06; $\gtrapprox 0$	9.63; 0.47	**0.11**; -0.05
Bering Sea	0.17; 0.1	46.1; 26.39	**0.43**; **0.46**
Sea of Okhotsk	-0.02; 0.01	4.55; 1.7	0.01; 0.04

4.1.3 Atlantic Multidecadal Oscillation

The SIV changes associated with the AMO are shown in Fig. 4.7. During AMO+, a significant SIV decline takes place in the Baffin Bay/Labrador Sea and Hudson Bay [Table 4.11]. A prevalent SIV reduction, although less pronounced, is noticeable in the Greenland Sea, Kara Sea, Beaufort Sea and Bering Sea as well. Inversely, an overall SIV increase is observed in the Sea of Okhotsk, Central Arctic and East Siberian Sea.

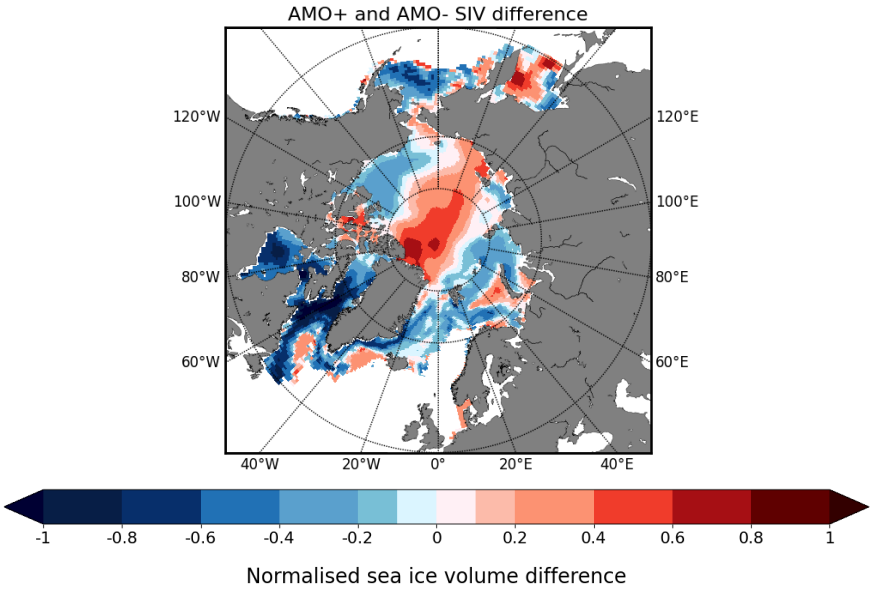


Fig. 4.7 – Difference in the mean of the PIOMAS-20C normalised SIV, from mid-1902 to mid-2009, between AMO+ and AMO-. The SIV time series of all grid-cells employed are normalised by their own standard deviation as to represent the relative impacts.

Table 4.11 – Regional sum of the mean SIV absolute difference between the AMO phases (AMO+ - AMO- SIV), regional sum of the mean SIV difference between the AMO phases relative to the regionally summed SIV variability and the area-weighted mean Pearson correlation coefficient (r) between the PIOMAS-20C SIV anomalies and the AMO index for each region. The relative SIV difference is computed by dividing the absolute value of the SIV difference with the 2 standard deviation of the regionally summed SIV time series. Significant correlations (p-value ≤ 0.01) are highlighted in bold.

Region	**Difference [km^3]**	**Relative difference [%]**	r
Beaufort Sea	-54.55	11.55	**-0.18**
Chukchi Sea	4.08	1.05	0.01
East Siberian Sea	107.39	12.07	**0.09**
Laptev Sea	2.25	0.75	-0.01
Kara Sea	-25.65	14.44	**-0.12**
Barents Sea	-8.92	5.45	$\gtrapprox 0$
Greenland Sea	-20	13.96	**-0.08**
Baffin Bay/Labrador Sea	-53.06	45.07	**-0.26**
Canadian Archipelago	9.51	5.47	0.03
Hudson Bay	-42.76	49.84	**-0.33**
Central Arctic	135	19.72	**0.11**
Bering Sea	-7.42	17.47	**-0.08**
Sea of Okhotsk	0.51	1.35	**0.07**

Dynamic influence

As depicted in Figs. 4.8a and 4.8b, the SP spatial patterns related to AMO- display a shallower AL, deeper IL and slightly more intense BH. This result differs from the SP patterns found for the other MOVs [Figs. 4.2a, 4.2b, A.6a, A.6b, 4.5a, 4.5b, A.8a and A.8b], where a deeper AL is associated with a more intense BH. Surprisingly, the change in the 10-m wind speeds between the two pressure systems, over the Arctic Ocean, is still significant for the AMO [Fig. A.4e]. This is because of the changes in the SP gradients driven by the shifts in the pressure systems [Fig. A.3e]. During AMO+, higher 10-m wind speeds are observed over the Arctic Ocean, while less intense speeds are found over the Bering Sea and North Atlantic Ocean as a result of the SP gradient patterns. The SIM speeds are therefore more pronounced in the Arctic Ocean, while being lower in the Bering Sea and North Atlantic Ocean [Figs. A.5e, 4.8c and 4.8d].

The SIM divergence shifts are shown in Fig. 4.8e. As supported by the regional quantified results of Table 4.12, the dynamic patterns are particularly noisy and no significant regionally widespread SIM divergence nor convergence takes place. Relatively important, although not significant, SIM divergence changes are nonetheless found in the Canadian Archipelago and Sea of Okhotsk. Localised effects are also noticeable. The SIV increase during AMO+ along the southern Chukchi Sea, eastern Wrangel Island, south-western Kara Sea, eastern Sea of Okhotsk and northern Greenland Sea coasts is partially driven by an SIM divergence reduction [Figs. 4.7 and 4.8e]. However, the SIV decline by the side of the western Wrangel Island, western New Siberian Islands, western Kara Sea, north-western Canadian Archipelago and western Sea of Okhotsk coasts is to some extent due to an SIM divergence increase. Although not significant, a prevalent SIM divergence increase occurs in the Beaufort Sea. This explains in part the SIV decrease during AMO+ found in this region. Overall, the dynamic influence associated with the AMO is not as regionally pronounced as for the other MOVs [Tables 4.2, 4.3, 4.7 and 4.8].

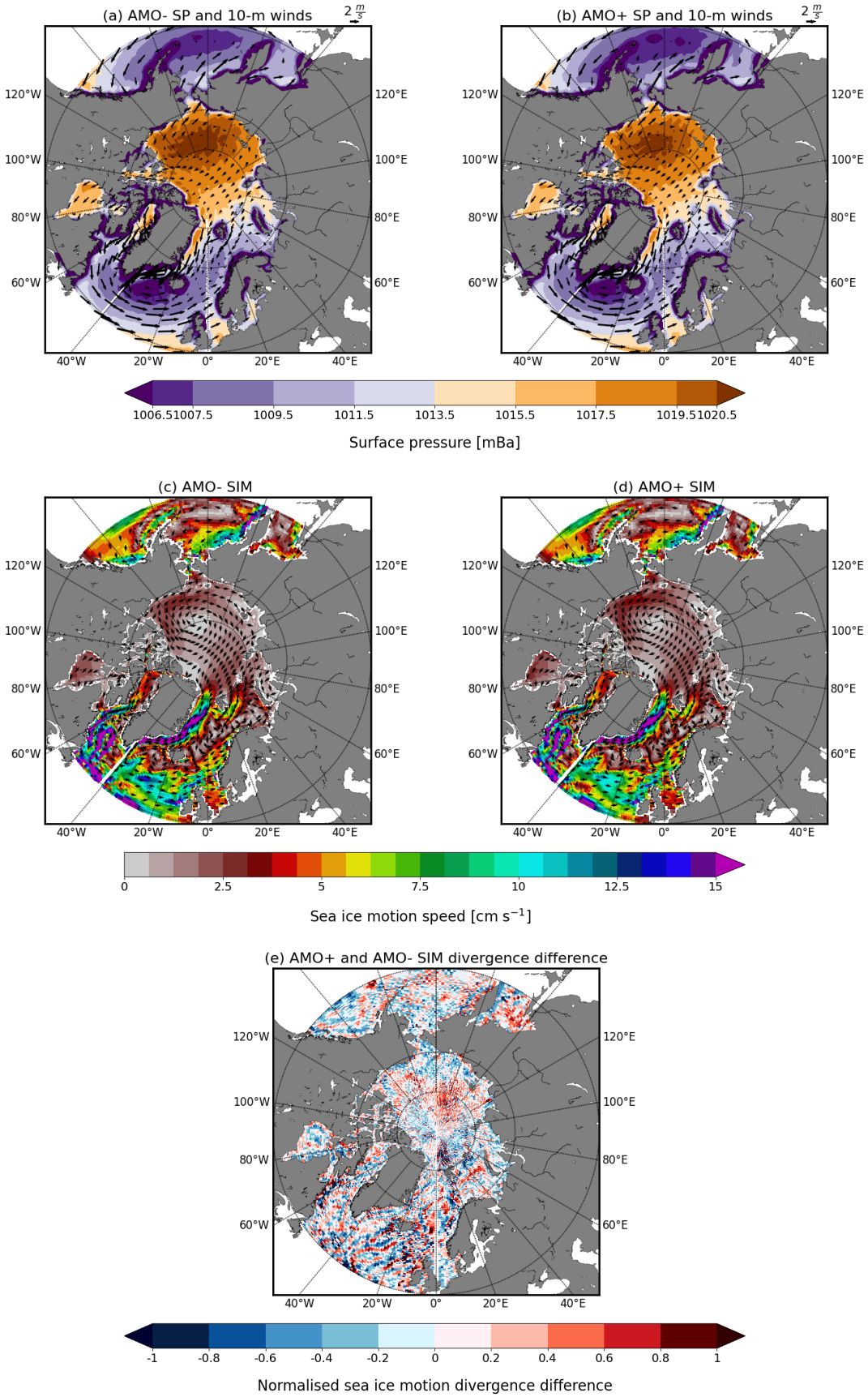


Fig. 4.8 – Dynamic processes spatial patterns associated with the AMO spanning from mid-1902 to mid-2009. The ERA-20C mean SP and 10-m winds distributions during (a) AMO- and (b) AMO+. The PIOMAS-20C mean SIM distributions during (c) AMO- and (d) AMO+. (e) The difference in the mean of the computed normalised SIM divergence between AMO+ and AMO-. The SIM divergence time series of all grid-cells are normalised by their own standard deviation as to represent the relative impacts.

Table 4.12 – Regional area integral of the mean SIM divergence (total SIM flux through the border) during AMO- and AMO+. Negative values indicate an overall influx, while positive values depict an overall outflux of sea ice through the border. The difference between the computed regional area integrals and the difference relative to the total regional area integral variability are also given. The relative difference is computed by dividing the absolute value of the difference with the 2 standard deviation of the total regional SIM border flux time series. Last column displays the area-weighted mean Pearson correlation coefficient (r) between the SIM divergence and the AMO index for each region. Significant correlations (p-value $\leq$ 0.01) are highlighted in bold.

Region	**AMO-** $[m^2/s]$	**AMO+** $[m^2/s]$	**Difference** $[m^2/s]$	**Relative difference** [%]	r
Beaufort Sea	-2.51 x 10^3	-1.86 x 10^3	6.51 x 10^2	9.64	0.04
Chukchi Sea	-1.18 x 10^4	-1.29 x 10^4	-1.07 x 10^3	14.12	-0.03
East Siberian Sea	1.69 x 10^2	9.16 x 10^2	7.47 x 10^2	10.55	0.02
Laptev Sea	8.32 x 10^3	8.99 x 10^3	6.73 x 10^2	9.76	0.03
Kara Sea	1.05 x 10^4	9.36 x 10^3	-1.08 x 10^3	16.57	-0.03
Barents Sea	-6.1 x 10^3	-6.96 x 10^3	-8.6 x 10^2	5.61	$\gtrapprox 0$
Greenland Sea	-7.02 x 10^4	-7.02 x 10^4	-2.26 x 10	0.17	$\gtrapprox 0$
Baffin Bay/Labrador Sea	1.57 x 10^4	1.44 x 10^4	-1.28 x 10^3	8.15	$\gtrapprox 0$
Canadian Archipelago	1.86 x 10^3	2.64 x 10^3	7.78 x 10^2	34.64	0.02
Hudson Bay	1.8 x 10^3	1.98 x 10^3	1.79 x 10^2	6.69	-0.02
Central Arctic	1.8 x 10^4	1.74 x 10^4	-6.28 x 10^2	16.62	0.01
Bering Sea	5.32 x 10^3	4.7 x 10^3	-6.21 x 10^2	4.96	$\lessapprox 0$
Sea of Okhotsk	6.96 x 10^3	8.85 x 10^3	1.89 x 10^3	31.03	0.03

Thermodynamic influence

As a result of the AMO definition, a prominent and widespread SST increase is observed in the North Atlantic Ocean [Fig. 4.9d] during AMO+. A prevalent SSHF decrease takes place over most of the North Atlantic Ocean [Fig. 4.9b], thus leading to an increase in SATs [Fig. 4.9c]. It is also important to mention the intensification of the ocean to atmosphere heat transfer and westerly atmospheric heat transport mechanism over the North Atlantic Ocean due to the higher wind speeds during AMO-. Indeed, an ITEFD increase is noticeable over the western North Atlantic Ocean, while a decline occurs over the eastern North Atlantic Ocean [Fig. 4.9a]. The SAT and SST dipole over the North Atlantic Ocean present for the AO, NAO and NPO does not appear for the AMO. Nonetheless, such a dipole exists over the North Pacific Ocean. An important and widespread SAT increase is observed over the Arctic Ocean during AMO+, while instead, the SSTs are mostly lower.

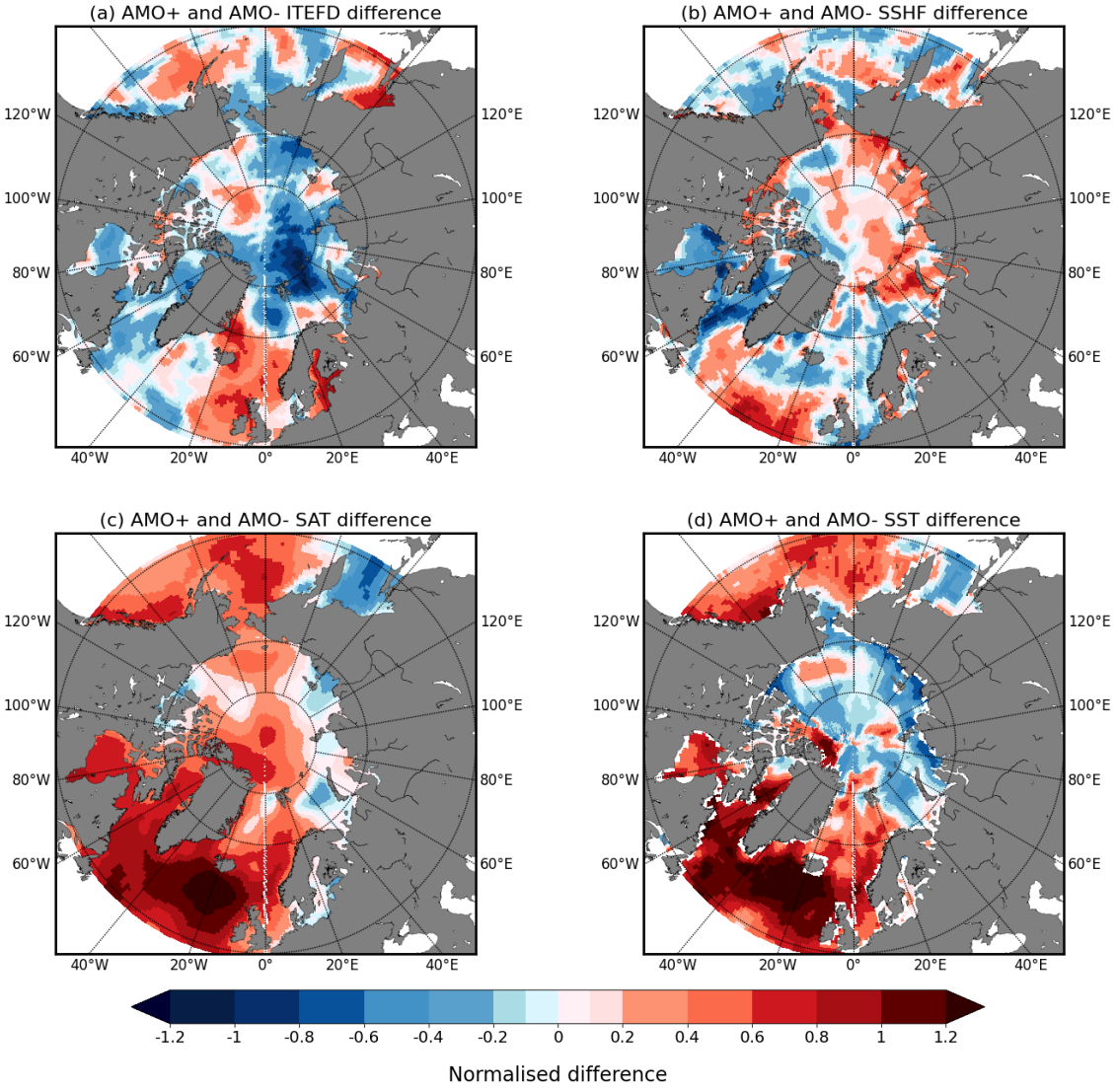


Fig. 4.9 – Difference between AMO+ and AMO-, from mid-1902 to mid-2009, in the mean of the ERA-20C normalised (a) ITEFD, (b) SSHF, (c) SAT and (d) SST. The various time series of all grid-cells employed are normalised by their own standard deviation as to represent the relative impacts.

Table 4.13 summarises the previous results. The regional fluctuations in the SST and SAT are especially prominent over the Greenland Sea, Hudson Bay and Baffin Bay/Labrador Sea, therefore explaining the important SIV decrease in these regions during AMO+ [Fig. 4.7]. The significant SAT and SST increase over the Bering Sea leads to an SIV decline as well. On the other hand, the SAT and SST reduction over the Sea of Okhotsk results in an SIV growth in this region. The SAT increase over the Beaufort Sea partially explains the SIV reduction, although dynamic impacts are observed in this region as well [Fig. 4.8e]. While a pronounced increase of SATs and SSTs is noticeable over the northern coast of the Greenland Sea, the SIM divergence decrease along this coast leads to an overall SIV growth. The increase in SIV in parts of the Barents Sea are driven by a decrease in SATs and SSTs during AMO+. Finally, the SIV growth in the East Siberian Sea is mainly driven by a combination of lower SSTs and SIM divergence. Because of the AMO definition, the impacts observed in the Arctic Ocean and North Pacific Ocean are not necessarily caused by this MOV. Nevertheless, possible teleconnections could uncover existing causal links between the AMO and the dynamic and thermodynamic processes occurring across these regions.

Table 4.13 – Mean SAT/SST absolute difference between the AMO phases (AMO+ - AMO- SAT/SST), mean SAT/SST difference between the AMO phases relative to the mean regional SAT/SST variability and the area-weighted mean Pearson correlation coefficient (r) between the ERA-20C SAT/SST anomalies and the AMO index for each region. The relative SAT/SST difference is computed by dividing the absolute value of the SAT/SST difference with the 2 standard deviation of the mean regional SAT/SST time series. Values on the left are associated with the SAT and values on the right with the SST. Significant correlations (p-value ≤ 0.01) are highlighted in bold. Only the grid-cells where sea ice is present (SIC > 0) are used for the computation of the means. Thus, only the SATs and SSTs directly affecting the sea ice are taken into account.

Region	**Difference [K]** **SAT; SST**	**Relative difference [%]** **SAT; SST**	r **SAT; SST**
Beaufort Sea	0.04; -0.01	7.7; 2.79	**0.16**; -0.04
Chukchi Sea	0.12; -0.02	20.11; 2.69	**0.2**; -0.01
East Siberian Sea	0.05; -0.02	10.49; 3.32	**0.18**; **-0.1**
Laptev Sea	-0.01; -0.01	3.73; 3.65	-0.02; **-0.15**
Kara Sea	0.01; -0.01	2.99; 2.98	0.03; **-0.14**
Barents Sea	0.02; -0.01	2.42; 1.42	-0.01; **-0.11**
Greenland Sea	0.18; 0.1	34.75; 19.41	**0.31**; **0.32**
Baffin Bay/Labrador Sea	0.32; 0.14	43.79; 18.84	**0.47**; **0.49**
Canadian Archipelago	0.02; $\lessapprox$ 0	8.82; 1.22	**0.2**; **0.08**
Hudson Bay	0.16; 0.04	34.63; 8.62	**0.43**; **0.38**
Central Arctic	0.16; $\gtrapprox$ 0	25.36; 0.04	**0.19**; 0.01
Bering Sea	0.11; 0.04	28.39; 9.98	**0.18**; **0.17**
Sea of Okhotsk	-0.08; -0.01	23.92; 3.49	**-0.2**; **-0.09**

4.2 Temporal analysis

In the following sections, we use wavelet analysis to identify the time frames and frequencies corresponding to the most important RSIV variabilities and how these can be explained by the MOVs. To do so, we first employ the previously provided quantified regional results to identify the regions that are the most affected by the MOV-related dynamic processes. The RSIV and RSIMF WPSs of the dynamically driven regions are then compared with the corresponding MOV index WPS to find similarities and possible connections between the variability of the 3 indices. Similarly, the SAT and SST quantified regional results are utilised to determine the most thermodynamically influenced regions, and thereafter uncover their temporal relationship with the MOV at hand. Finally, lag-tests are performed to deduce the delay between the various MOVs and their most important regional impacts. The response-times corresponding to the most affected regions are especially highlighted.

4.2.1 Arctic Oscillation and North Atlantic Oscillation

The AO index WPS displays 2 important variabilities of a period of 20 and 13.2 years spanning from 1955 to 1980 and 1925 to 1945, respectively [Fig. 4.10a]. An intense signal of a period of approximately 17 years is also visible around the end of the century. Weaker, yet still significant wavelet powers are noticed at periods of roughly 5 and 8.5 years lasting from 1935 to 1950 and 1960 to 1995, respectively. Because of the strong relationship between the NAO and AO, their corresponding WPSs are similar. Indeed, the NAO index WPS depicts 2 distinct 8.5- and 17-year period peaks around the same time frame as the corresponding signals in the AO index WPS [Fig. 4.10b]. A relatively less intense 12.5-year period peak is present from 1920 to 1940, whereas the 8.5-year period variability is relatively more pronounced for the NAO. Finally, unlike the AO, a significant 7-year period variability takes place around the beginning of the century.

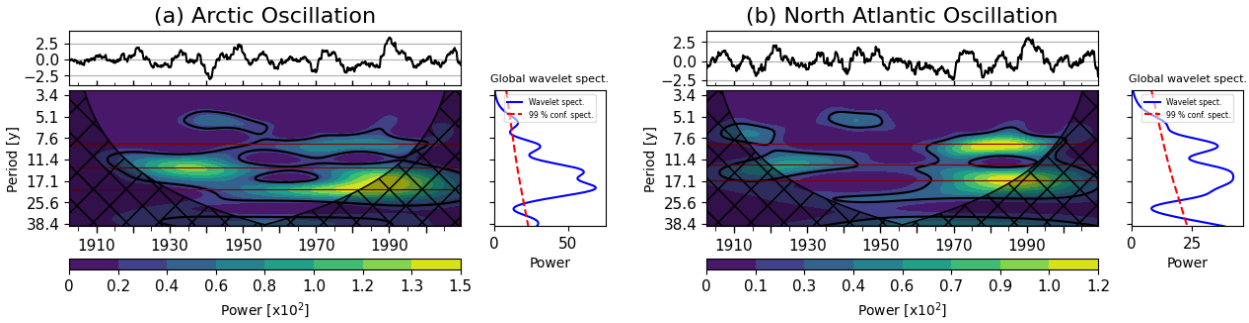


Fig. 4.10 – Wavelet analysis spanning from mid-1902 to mid-2009 of the (a) AO index and (b) NAO index. Top plot represents the index time series. Bottom plot represents the WPS of the time series. Bottom right plot represents the mean power spectrum. The thick black contours and red dashed lines represent the 99% significance level using a red noise background power spectrum, whereas the crosshatched areas represent the cone of influence where edge effects become important. Horizontal solid red lines represent the 8.5-, 13.2- and 20-year periods for the AO and 8.5-, 12.5- and 17-year periods for the NAO. The Morlet function was used for the wavelet analysis.

Dynamic influence

As shown in Figs. 4.11a, 4.11b, 4.11c and 4.11d, the Beaufort Sea, Chukchi Sea, East Siberian Sea and Laptev Sea RSIV WPSs display similarities to the RSIMF and AO/NAO index WPSs. Actually, these regions are significantly impacted by the dynamic processes related to the AO/NAO [Tables 4.1, 4.2 and 4.3]. The AO-associated processes are especially influential in the Chukchi Sea and East Siberian Sea, while the effects of the NAO are greatly felt in the Beaufort Sea, East Siberian Sea and Laptev Sea. The presence of the 8.5-year period signal in the Beaufort Sea RSIV, RSIMF and NAO index WPSs suggests a link between

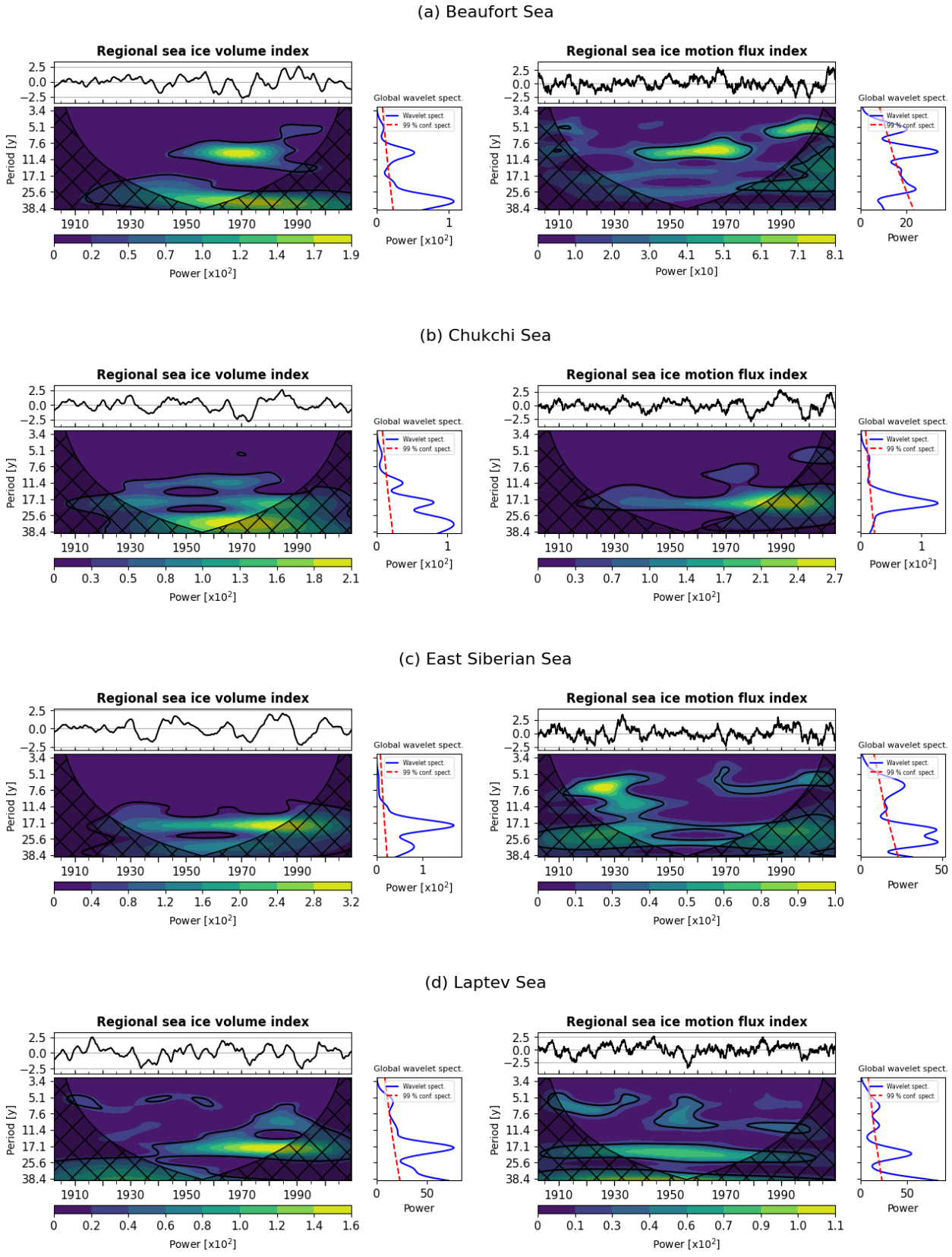


Fig. 4.11 – Wavelet analysis spanning from mid-1902 to mid-2009 of the RSIV and RSIMF for the (a) Beaufort Sea, (b) Chukchi Sea, (c) East Siberian Sea and (d) Laptev Sea. Top plot represents the index time series. Bottom plot represents the WPS of the time series. Bottom right plot represents the mean power spectrum. The thick black contours and red dashed lines represent the 99% significance level using a red noise background power spectrum, while the crosshatched areas represent the cone of influence where edge effects become important. The Morlet function was used for the wavelet analysis. Figures on the left represent the RSIV WPS and figures on the right represent the RSIMF WPS.

the dynamic processes associated with the NAO and the Beaufort Sea 8.5-year period RSIV variability. Similarly, given the important dynamic impact of the AO in the Chukchi Sea, the intense 17.5-year period signal corresponding to the RSIV is likely driven by the RSIMF variations related to the AO, although the NAO could play a role around the end of the century as well. An important 17.5-year period variability takes place in the East Siberian Sea RSIV, RSIMF and in the AO/NAO index WPSs. This indicates a relationship between the AO/NAO and the East Siberian Sea RSIV signal. It is also interesting to point out the pronounced 13-year period wavelet powers observed in the Chukchi Sea and East Siberian Sea RSIV and RSIMF WPSs, thus suggesting a relatively weak AO/NAO impact. The Laptev Sea, on the other hand, is mainly affected by the NAO. The 17.5-year period Laptev Sea RSIV variability seems to be partially driven by the NAO-induced RSIMF changes. A link, although weak, between the 8.5-year period peak in the Laptev Sea RSIV WPS and the NAO 8.5-year period signal could exist as well, since such a significant variability, although dim, takes place in the RSIMF.

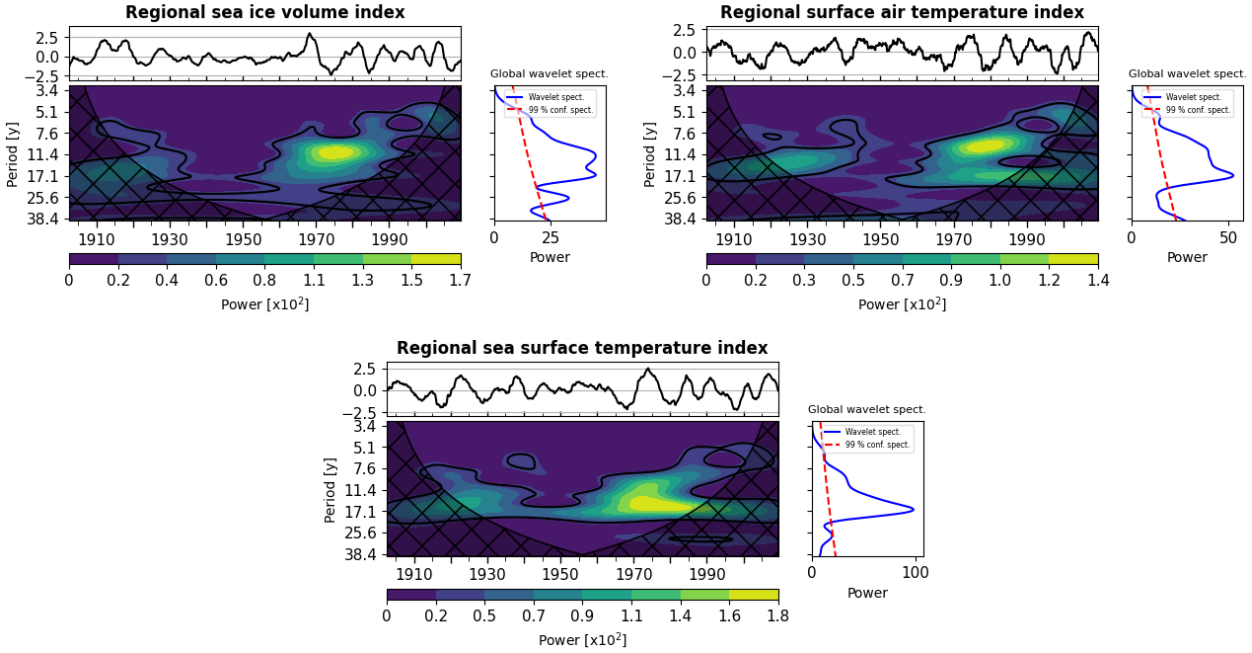
Overall, the dynamic influence driven by the AO is especially felt in the Chukchi Sea and East Siberian Sea as a 17.5-year period RSIV variability spanning most of the century, but with a more pronounced impact around the end of the century. For the NAO, such an influence is present in the Beaufort Sea as an 8.5-year RSIV signal from 1965 to 1975, and in the East Siberian Sea and Laptev Sea as a 17.5-year period RSIV peak from 1965 onwards.

Thermodynamic influence

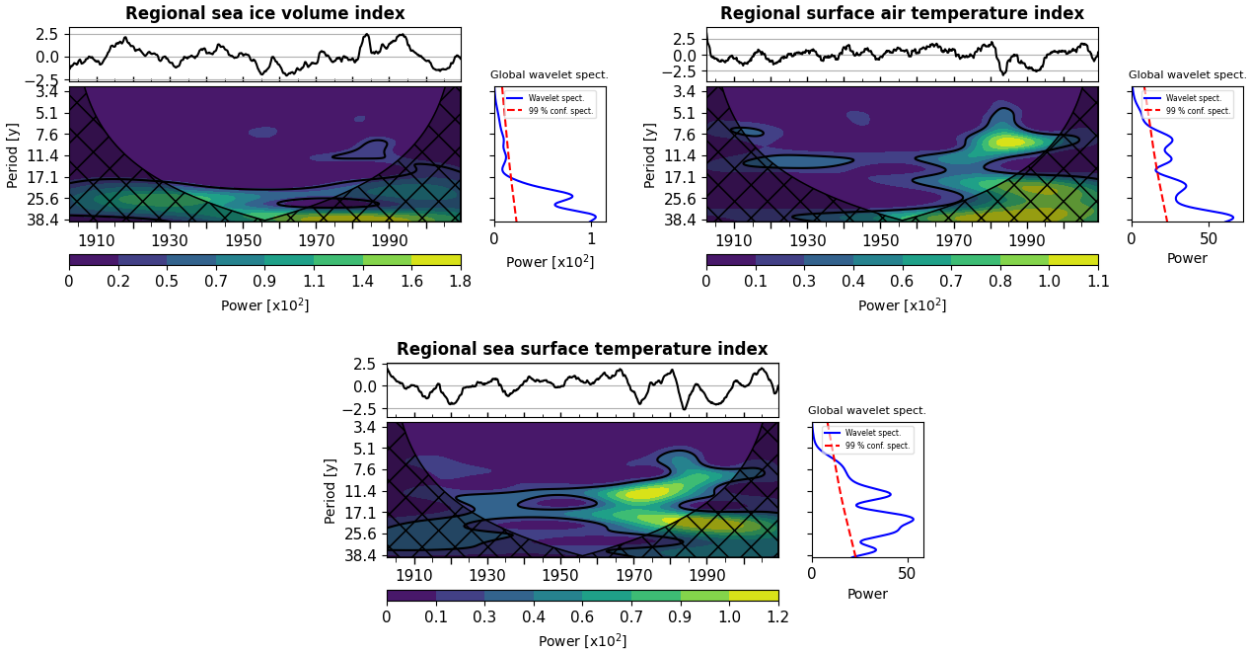
The SAT and SST spatial patterns corresponding to the AO and NAO [Figs. 4.3c, 4.3d, A.7c and A.7d], lead to prevalent thermodynamic impacts over many regions [Tables 4.1, 4.4 and 4.5]. The Bering Sea and Sea of Okhotsk RSIV, RSAT and RSST WPSs are shown in Figs. 4.13c and 4.13d. These regions are greatly affected thermodynamically by the AO and display similarities in their WPSs. In fact, these regions exhibit a noticeable 8.5 and 17-year period signal in their RSIV, RSAT and RSST WPSs, especially around the end of the century, similarly to the AO. The Barents Sea RSIV WPS [Fig. 4.13a] exhibits a weak, yet still significant, 13-year period signal in part driven by the AO. The NAO also drives the Barents Sea and Sea of Okhotsk RSIV evolutions through the thermodynamic processes associated with this MOV. Therefore, the 8.5-, 13- and 17-year period peaks present in the Barents Sea and Sea of Okhotsk RSIV, RSAT and RSST WPSs can be explained to some extent by the NAO. The 8.5-year signal is especially pronounced in the Barents Sea, thus indicating an important impact related to the NAO. Notable results are also found in other regions. As a matter of fact, the Chukchi Sea, East Siberian Sea, Laptev Sea, Kara Sea and Baffin Bay/Labrador Sea [Fig. 4.13b] are significantly influenced by the AO/NAO, and display similarities between their RSIV, RSAT, RSST and the AO/NAO index WPSs as shown in Figs. A.10, A.11 and A.12. The 17-year period variability present in the RSIV WPS of the Chukchi Sea, East Siberian Sea, Laptev Sea, Kara Sea and Baffin Bay/Labrador Sea is driven, to some extent, by the thermodynamic processes associated with the AO/NAO. Finally, the 8.5-year period variability found in the RSIV WPS of the Chukchi Sea and Laptev Sea is partially driven by the AO/NAO as well.

Overall, the thermodynamic influence driven by the AO is especially felt in the East Siberian Sea, Laptev Sea, Bering Sea and Sea of Okhotsk, where the 8.5- and 17-year period signals are partially caused by the AO. For the NAO, the important 8.5-year period variability found in the Beaufort Sea and Barents Sea can be explained in part by the intense thermodynamical influence related with the NAO, but the 17-year period signals noticed in the East Siberian Sea and Laptev Sea are also driven by this MOV. The Sea of Okhotsk shows similarities for the 8.5- and 17-year period peaks as well, thus suggesting a link between these signals and the NAO. The important influence of the NAO in the Baffin Bay/Labrador Sea and the similarities found for the 9- and 18.5-year signals suggest a relationship between the NAO-associated thermodynamic processes and the Baffin Bay/Labrador Sea RSIV variability. Because of the important resemblance between the AO and NAO index WPSs, differentiating the RSIV variabilities driven by either of the two MOVs remains a challenging task.

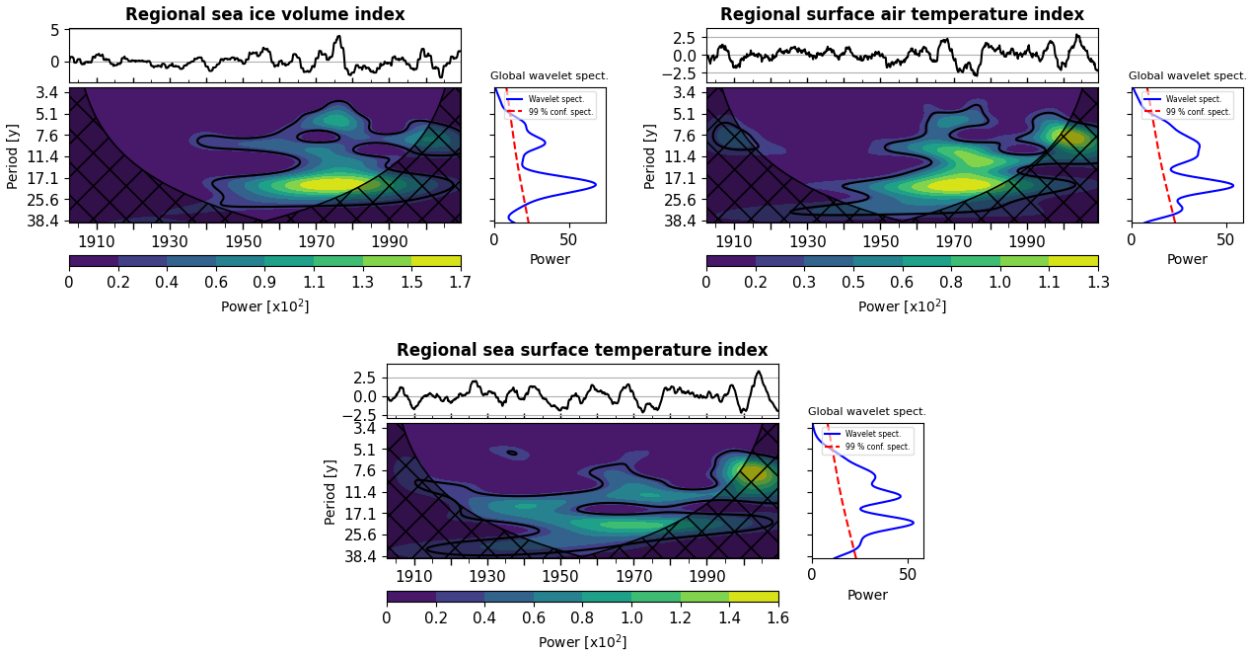
(a) Barents Sea



(b) Baffin Bay/Labrador Sea



(c) Bering Sea



(d) Sea of Okhotsk

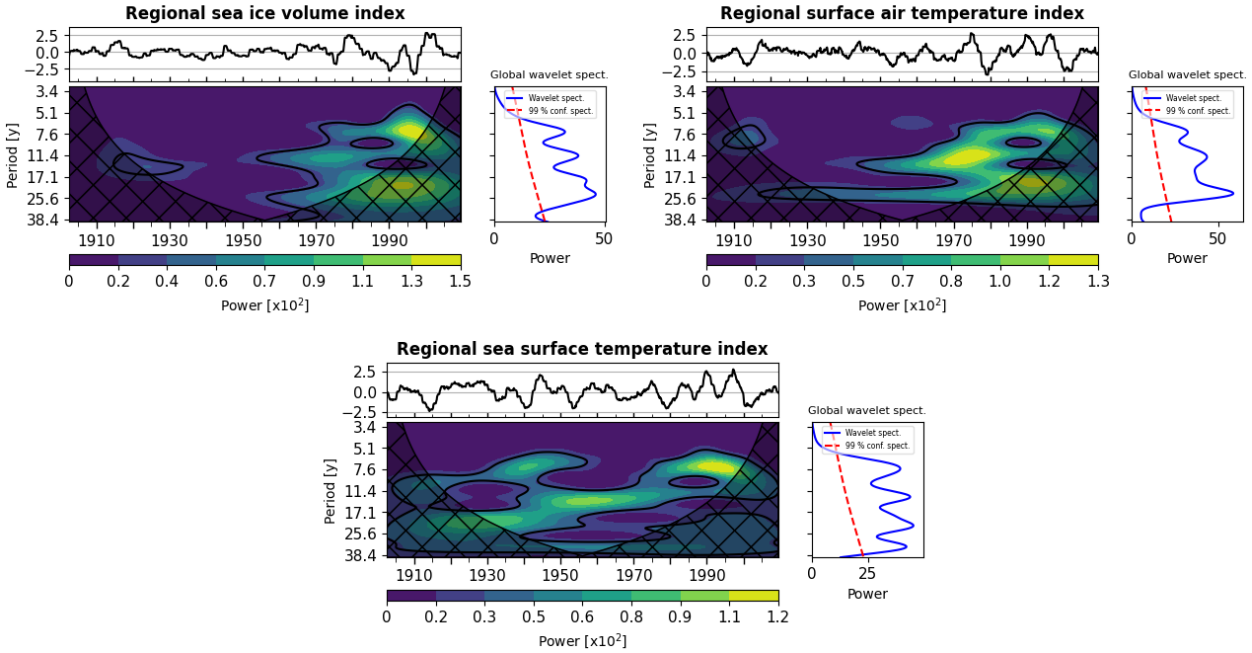


Fig. 4.13 – Wavelet analysis spanning from mid-1902 to mid-2009 of the RSIV, RSAT and RSST for the (a) Barents Sea, (b) Baffin Bay/Labrador Sea, (c) Bering Sea and (d) Sea of Okhotsk. Top plot represents the index time series. Bottom plot represents the WPS of the time series. Bottom right plot represents the mean power spectrum. The thick black contours and red dashed lines represent the 99% significance level using a red noise background power spectrum, while the crosshatched areas represent the cone of influence where edge effects become important. The Morlet function was used for the wavelet analysis. Figures on the top left represent the RSIV WPS, figures on the top right depict the RSAT WPS and figures on the bottom center represent the RSST WPS.

4.2.2 North Pacific Oscillation and Pacific Decadal Oscillation

The NPO index WPS exhibits an intense signal of a 15-year period from 1925 to 1950 [Fig. 4.14a]. Weaker variabilities of 6.5- and 20-year periods around the beginning of the 20th century and lasting the entire century, respectively, are also present. The PDO WPS is rather different from the NPO [Fig. 4.14b]. It has its most prominent peak at a period of about 21 years spanning from 1930 to 1975 and is especially broad in the time and frequency space. The existence of a significant 9-year period peak from the 1990s onwards, is noticeable as well. Finally, the PDO exhibits significant wavelet powers at a period of roughly 15 years, similarly to the NPO.

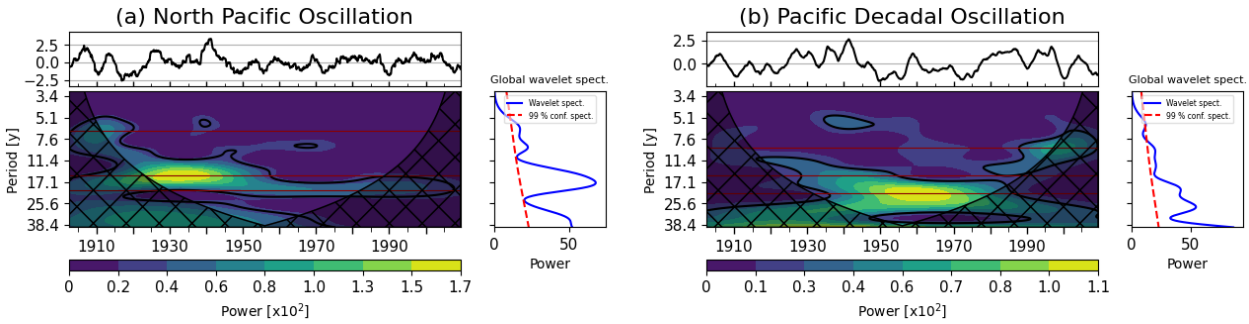


Fig. 4.14 – Wavelet analysis spanning from mid-1902 to mid-2009 of the (a) NPO index and (b) PDO index. Top plot represents the index time series. Bottom plot represents the WPS of the time series. Bottom right plot represents the mean power spectrum. The thick black contours and red dashed lines represent the 99% significance level using a red noise background power spectrum, while the crosshatched areas represent the cone of influence where edge effects become important. Horizontal solid red lines represent the 6.5-, 15- and 20-year periods for the NPO and 9-, 15- and 21-year periods for the PDO. The Morlet function was used for the wavelet analysis.

Dynamic influence

A significant dynamic impact associated with the NPO takes place in the Chukchi Sea [Tables 4.6 and 4.7]. The 17-year period signal in the RSIV and RSIMF WPSs [Fig. 4.11b] is observed in the NPO index WPS as well, thus suggesting a link between this MOV and the dynamic processes affecting the RSIV. The NPO also partially drives the 15-year period signal found in the Chukchi Sea and East Siberian Sea, although these variabilities remain dim. The PDO mainly influences the Chukchi Sea and Laptev Sea [Tables 4.6 and 4.8]. However, few similarities exist between their RSIV, RSIMF and the PDO index WPSs.

Given the importance of the dynamic impacts driven by the NPO and the resemblance between the Chukchi Sea RSIV, RSIMF and NPO index WPSs, we conclude that the 15- and 17-year period variabilities are partially caused by the NPO. Differentiating the signals driven by the NPO, AO and NAO remain nonetheless complicated because of the similarities in their WPSs, especially around the 17-year period.

Thermodynamic influence

The Beaufort Sea, Laptev Sea, Bering Sea and Sea of Okhotsk are especially impacted by the SAT and SST patterns associated with the NPO [Tables 4.6 and 4.9]. Having said that, few similarities between their RSIV, RSAT, RSST WPSs and the NPO index WPS exist, as displayed in Figs. 4.13c, 4.13d, A.10, A.11, A.12 and 4.14a. However, the thermodynamic processes related to the PDO are especially noticeable in the Bering Sea [Tables 4.6 and 4.10]. Indeed, the 9-year period signal taking place from 1990s onwards, is also present in the Bering Sea RSIV, RSAT and RSST WPSs. On top of this, the 16- to 25-year period broad peak is prevalent in these WPSs as well. Given the importance of the thermodynamic impact of the PDO in

the Bering Sea, this suggests that these signals are mainly driven by the PDO. Although the Greenland Sea is not as significantly impacted, similarities between its WPSs and the PDO index WPS are observed. This suggests a connection between the thermodynamic processes associated with the PDO and the Greenland Sea RSIV shifts. The Hudson Bay and Kara Sea WPSs also show similarities for the 9-year period and lower frequency signals, although the Hudson Bay low frequency variabilities are mainly present around the end of the century. The importance of the PDO-associated thermodynamic processes over these regions suggests a link between these processes and the RSIV variations. Because of the prominent influence of the PDO in the Bering Sea and similarities found in the WPSs, the connection between this MOV and the Bering Sea remain the most convincing. In particular, the 9-year period variability from 1990s onwards and the broad 16- to 25-year period signals can be largely attributed to the PDO-induced thermodynamic impacts.

4.2.3 Atlantic Multidecadal Oscillation

The AMO index WPS displays an important peak lasting from 1975 to 1995, with a corresponding period of 9 years [Fig. 4.15]. 27- and 18.5-year period variabilities spanning from 1940 to 1960 and 1965 to 1985, respectively, can also be seen. As previously discussed, the dynamic impacts associated with the AMO are not regionally significant [Tables 4.11 and 4.12]. Therefore, only an analysis of the thermodynamic influence is provided for this MOV.

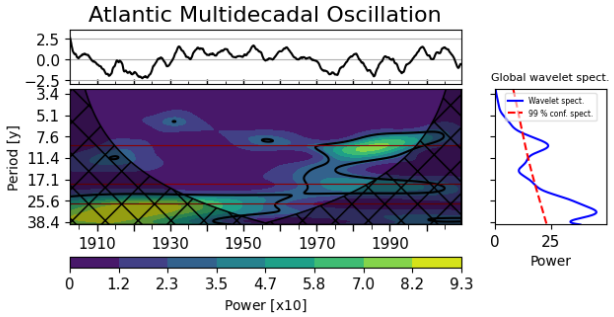


Fig. 4.15 – Wavelet analysis spanning from mid-1902 to mid-2009 of the AMO index. Top plot represents the index time series. Bottom plot represents the WPS of the time series. Bottom right plot represents the mean power spectrum. The thick black contours and red dashed line represent the 99% significance level using a red noise background power spectrum, while the crosshatched areas represent the cone of influence where edge effects become important. Horizontal solid red lines represent the 9-, 18.5- and 27-year periods. The Morlet function was used for the wavelet analysis.

Thermodynamic influence

The Baffin Bay/Labrador Sea and Hudson Bay are particularly affected thermodynamically by the AMO [Tables 4.11 and 4.13]. As a matter of fact, the RSIV, RSAT and RSST WPSs associated with these regions, exhibit similarities to the AMO index WPS [Figs. 4.13b, A.10j, A.11j, A.12j and 4.15]. The 9- and 18.5-year period peaks present in the Baffin Bay/Labrador Sea and Hudson Bay WPSs are noticeable in the AMO index WPS as well, thus suggesting the existence of a causal factor between these signals and the AMO-driven RSAT and RSST temporal shifts. Surprisingly, the 27-year period variability taking place in the AMO index and Baffin Bay/Labrador Sea RSIV WPSs is not significant in the RSAT and RSST WPSs. Nevertheless, the thermodynamic impacts related to the AMO are also felt in other regions RSIV fluctuations. The Beaufort Sea, Greenland Sea and Laptev Sea are all significantly impacted thermodynamically by the processes related to the AMO, and all display 27-year period variabilities in their respective RSIV WPS. These signals can be partially explained by the AMO because of their presence in the RSAT and RSST WPSs. Overall, the results found in the Hudson Bay and Baffin Bay/Labrador Sea remain the most convincing. Given the prominent

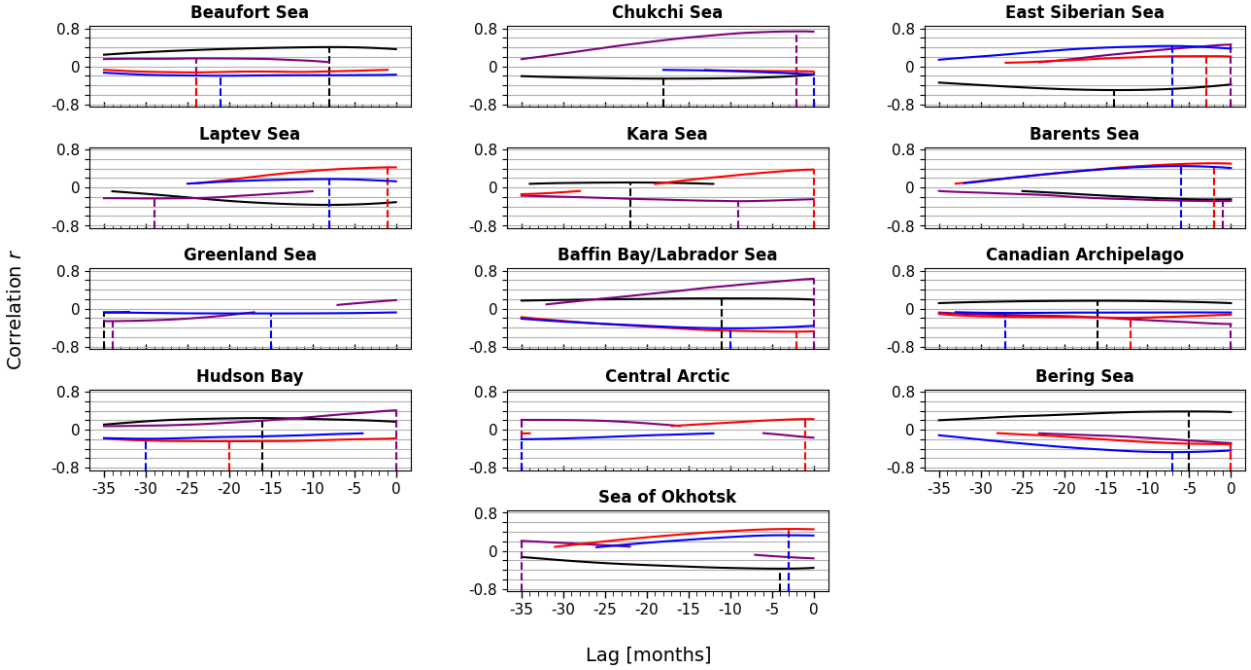
influence of the thermodynamic processes related to the AMO in these regions, the 18.5- and 9-year period signals are greatly driven by this MOV.

4.2.4 Lag-tests

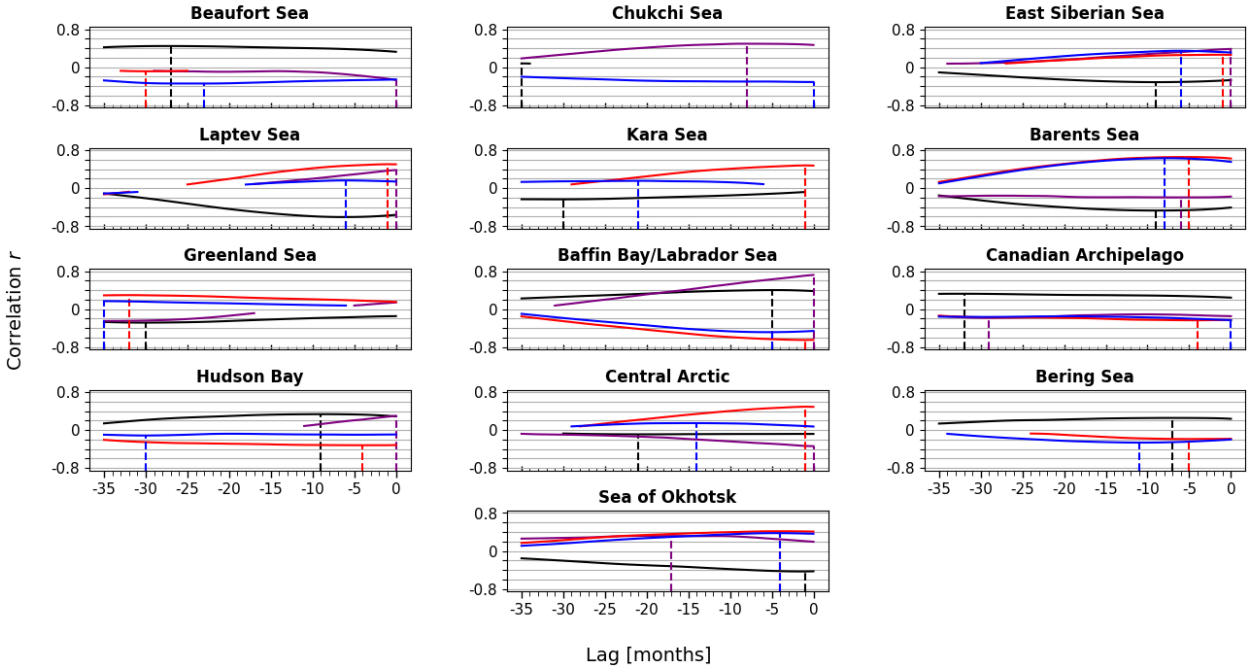
In most regions, the highest impact caused by the various MOVs is not felt immediately, but rather months following the shifts in the spatial patterns associated with these MOVs. As shown in Fig. 4.18, the most significant correlations are reached when the combined effect of the RSIMF, RSAT and RSST on the RSIV is maximised. The delays of the dynamic and thermodynamic processes, that in turn lead to the observed RSIV lags, are a result of the time it takes for the changes in the SIM, SAT and SST distributions to occur as a response to a change in the MOVs.

The lag in months between the various MOVs and their most important influence on the RSIV of each region are shown in Table 4.14. For the AO, a gradual decline in the lag-times associated with the Chukchi Sea, East Siberian Sea and Laptev Sea RSIVs is visible. A similar delay between the AO and NPO is observed in the Chuckhi Sea. Instead, the Bering Sea and Sea of Okhotsk RSIVs delays are smaller, thus indicating a faster response to the AO shifts. The Bering Sea RSIV delay is one month later than the Sea of Okhotsk due to the delayed SST response as revealed by Fig. 4.18a. Similarly, the NAO displays a gradual decline in the lag-times corresponding to the Beaufort Sea, East Siberian Sea and Laptev Sea RSIVs. The Beaufort Sea RSIV response-time is especially large and is greatly due to the long RSST delay [Fig. 4.18b]. On the other hand, the Sea of Okhotsk RSIV delay is particularly low, as a result of the quick thermodynamic processes response-time, but a causal link between the NAO and Sea of Okhotsk RSIV variability remains to be established. However, the Barents Sea and Baffin Bay/Labrador Sea RSIVs are directly impacted by the NAO-induced surface wind shifts and display a 9- and 5-month lag-time, respectively, largely because of the SST and SAT delays. The PDO quickly influences the Bering Sea RSIV as it is directly influenced by the SST anomalies, that define the MOV, and SAT fluctuations that are closely linked with the MOV as well [Fig. 4.18d]. Similarly, the Hudson Bay and Baffin Bay/Labrador Sea RSIVs exhibit a near immediate response to the changes in the AMO for the same reason [Fig. 4.18e]. The Baffin Bay/Labrador Sea RSIV is significantly influenced by the AO as well and depicts a relatively quick response-time. Finally, we should mention that the lag-time results can indicate which RSIV fluctuations are not caused by the MOVs. Indeed, the 0 lag-times found in Table 4.14, mean that the highest regional impact is felt instantaneously, or prior to the MOVs shifts. While this would suggest a non-causal relationship between the regions RSIV variability and the respective MOV, these results remain not conclusive enough to assert such a statement.

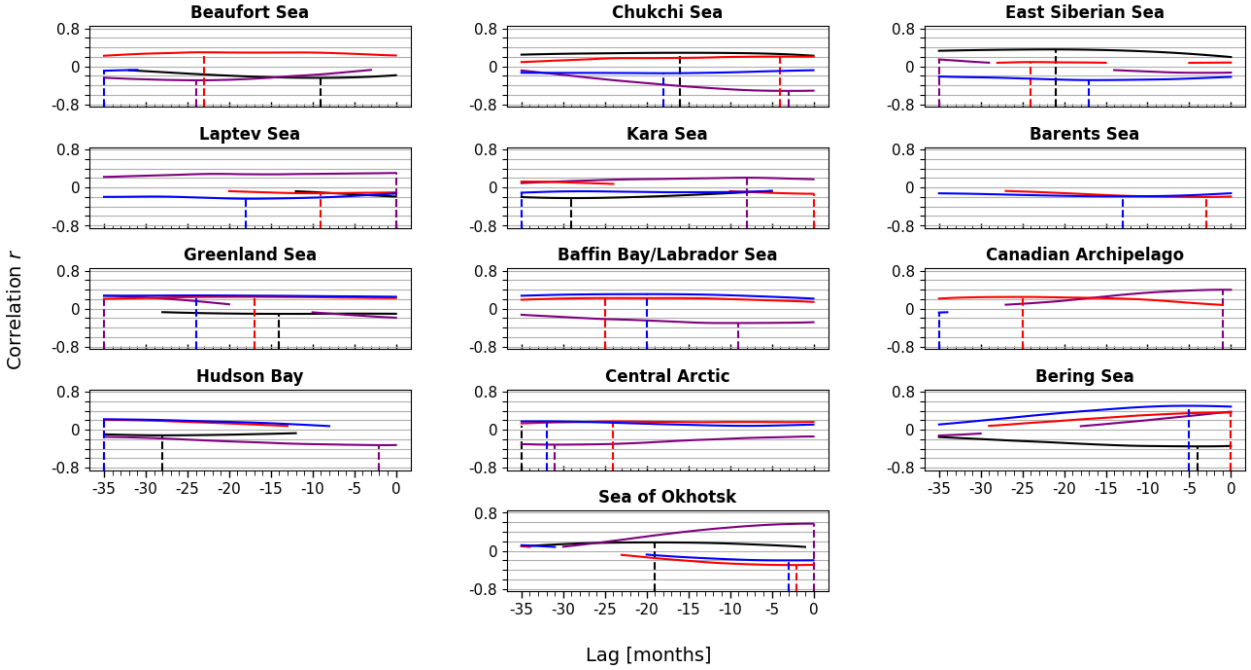
(a) Arctic Oscillation



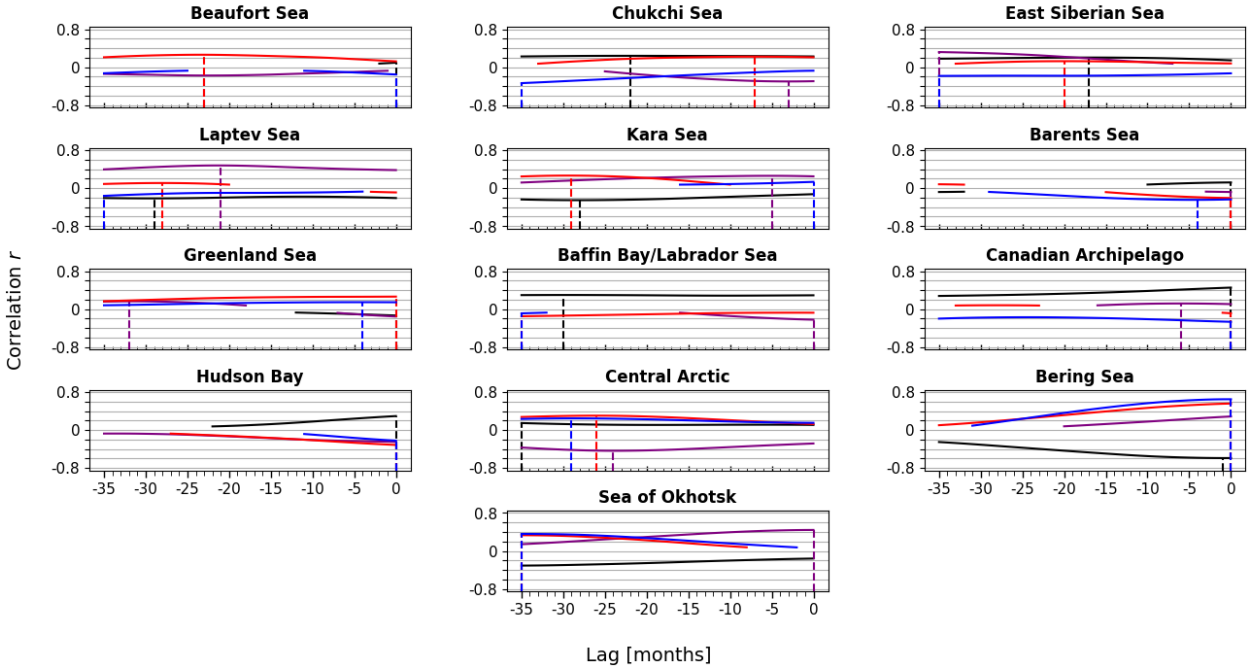
(b) North Atlantic Oscillation



(c) North Pacific Oscillation



(d) Pacific Decadal Oscillation



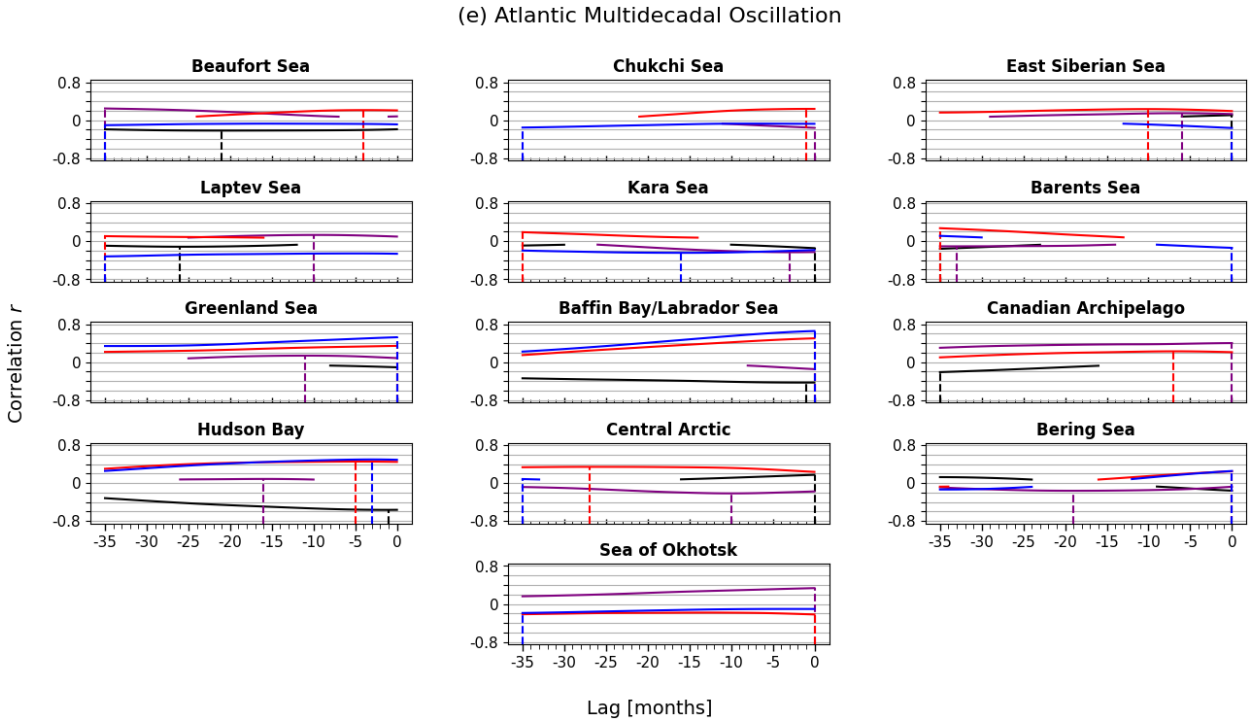


Fig. 4.18 – Monthly lag-time correlations between the RSIV (**black**), RSIMF (**purple**), RSAT (**red**), RSST (**blue**) and the (a) AO index, (b) NAO index, (c) NPO index, (d) PDO index and (e) AMO index. A time frame spanning from mid-1905 to mid-2009 is chosen for the RSIV, RSIMF, RSAT and RSST indices. The MOVs are then shifted accordingly to calculate the lag correlations. Solid lines represent the correlations as a function of the lag in months. Vertical dashed lines depict the month-lag leading to the most important correlation corresponding to the RSIV, RSIMF, RSAT and RSST. Only the significant correlations to a confidence level greater than 99% (p-value ≤ 0.01) are displayed. Note that for certain MOVs and regions, no results are represented for the RSIV, RSIMF, RSAT or RSST because of the non-existence of significant correlations for any lag-time.

Table 4.14 – Lag-time in months when the most important correlations are found between the RSIV index and the various MOVs indices, using the results of Fig. 4.18. A value of 0 indicates no delay, while a value of 35 is the upper limit and depicts a delay of 35 months between the RSIV and MOV. The regions for which the RSIV is greatly impacted by the MOV (as concluded from the temporal analysis) are highlighted in red. Missing values imply no significant correlations (p-value ≤ 0.01) exist.

Region	**AO**	**NAO**	**NPO**	**PDO**	**AMO**
Beaufort Sea	8	27	9	0	21
Chukchi Sea	18	35	16	22	-
East Siberian Sea	14	9	21	17	0
Laptev Sea	8	6	0	29	26
Kara Sea	22	30	29	28	0
Barents Sea	2	9	-	0	35
Greenland Sea	35	30	14	0	0
Baffin Bay/Labrador Sea	11	5	-	30	1
Canadian Archipelago	16	32	0	0	5
Hudson Bay	16	9	28	0	1
Central Arctic	-	21	35	35	0
Bering Sea	5	7	4	1	0
Sea of Okhotsk	4	1	19	35	-

Chapter 5

Conclusions

In this study, we have analysed the impact of the AO, NAO, NPO, PDO and AMO on the Arctic SIV variability of various regions from the PIOMAS-20C reconstructed data. A spatial and temporal analysis was performed to answer the three questions set as an objective in section 1.5. The former uncovers the dynamic and thermodynamic impacts of the various MOVs in each region, but also explains the underlying mechanisms leading to such processes. In particular, the shifts in the BH and AL pressure systems, associated with the AO/NAO, lead to important changes in the SIM vector field. As a result, significant AO/NAO-related dynamic impacts are felt across the Arctic Ocean, and especially in the Beaufort Sea, Chukchi Sea, East Siberian Sea and Laptev Sea. These results are akin to the findings of Rigor et al. [2002] and Van Achter et al. [2020], where similar dynamic changes across the Arctic Ocean are shown to be triggered by the AO. The Wavelet analysis reveals a dynamically induced multidecadal 17.5-year period RSIV variability related to the AO/NAO, in the Chukchi Sea, East Siberian Sea and Laptev Sea. In the Beaufort Sea, an RSIV signal corresponding to a period of 8.5 years and spanning from 1965 to 1975 is partially driven by NAO-associated dynamic processes. The surface wind changes linked to the AO/NAO phase fluctuations generate new SAT and SST spatial patterns through SSHF and atmospheric heat transport shifts. The North Atlantic Ocean and North Pacific Ocean regions are revealed to be particularly influenced by these alterations. Indeed, the Barents Sea and Sea of Okhotsk 8.5- and 17-year period signals are shown to be influenced by the AO/NAO-induced thermodynamic processes to some extent, with an especially pronounced impact of the NAO in the Barents Sea. Having said that, the effects triggered by these processes are also prevalent over the Arctic Ocean. The 1965 to 1975 8.5-year period variability found in the Beaufort Sea RSIV is thermodynamically driven by the NAO as well, whereas the 8.5- and 17-year period peaks in the East Siberian Sea and Laptev Sea are partially caused by the AO/NAO-related thermodynamic processes. The lag-tests indicate a significant delay between the AO and the Chukchi Sea, East Siberian Sea and Laptev Sea RSIVs response, spanning from 8 months for the Laptev Sea to 18 months for the Chukchi Sea RSIVs, whereas much shorter lag-times of 5 and 4 months are found for the Bering Sea and Sea of Okhotsk RSIVs, respectively. The lag-times between the NAO and the East Siberian Sea, Laptev Sea and Sea of Okhotsk RSIVs are lower than for the AO and vary from 1 month for the Sea of Okhotsk, to 9 months for the East Siberian Sea RSIVs. However, a causal link between the NAO and Sea of Okhotsk RSIV fluctuations remains to be proven. Instead, response-times of 9 and 5 months are revealed for the Barents Sea and Baffin Bay/Labrador Sea RSIVs, respectively. Interestingly, a particularly long delay of 27 months between the NAO and Beaufort Sea RSIV is found and is mainly due to the long RSST delay.

The intense fluctuations in the depth of the AL defining the NPO lead to pronounced surface wind modifications over the Beaufort Sea and Chukchi Sea. The resulting SIM field adjustments give rise to significant dynamic impacts in the Chukchi Sea, although important changes in the SATs and SSTs in the Bering Sea and Sea of Okhotsk are also observed. Our results are in agreement with the findings of Linkin and Nigam [2008], setting forth the existence of warm southerly air masses especially over the eastern Bering Sea during a more intense AL phase. Although no SAT decrease is found over the western Bering Sea in our study, the SAT increase exhibited is mostly weak or non-existent. Also, while an SIM divergence from the

Russian coast driven by westerly-northwesterly winds is suggested by Linkin and Nigam [2008], in our case, such a divergence is mostly induced by northerly winds. The wavelet analysis reveals similarities between the Chukchi Sea RSIV, RSIM and NPO index WPSs at a 17-year period, although a resemblance at a period of around 15 years is also found from 1930-1945. We find that the delay between the NPO index and the Chukchi Sea RSIV is of around 16 months, similarly to the 18-month lag-time observed for the AO in the same region. Whilst thermodynamic impacts induced by the NPO are apparent in the Bering Sea and Sea of Okhotsk, the footprint of the NPO index in the temporal variability of the RSIV is not as pronounced and non-significant. The PDO and AMO are found to lead to important thermodynamic impacts over the North Pacific Ocean and North Atlantic Ocean, respectively. The 9-year period signal from the 1990s onwards and the broad peak spanning from a period of 16 to 25 years associated with the Bering Sea RSIV variability are greatly driven by the PDO. Instead, the Hudson Bay and Baffin Bay/Labrador Sea 9- and 18.5-year period variabilities are strongly influenced by the AMO, although links between the Baffin Bay/Labrador Sea RSIV signals and the NAO are convincing as well. As shown by Mahajan et al. [2011], we also obtain an increase in SATs over the Baffin Bay/Labrador Sea and Hudson Bay, although in our study, the SAT increase over the Hudson Bay is more significant. Unlike Castruccio et al. [2019], we observed no negative correlation between the AMO and PDO. Nevertheless, a lag-time of 1 month is found between the PDO and Bering Sea RSIV, and between the AMO and Baffin Bay/Labrador Sea, Hudson Bay RSIVs. Such short delays are explained by the direct relationship between the SATs and SSTs over these regions and the PDO/AMO definition.

Overall, the spatial patterns associated with each MOVs are relatively similar. Such results are for the most part generated by the SP distributions. In particular, the AL and BH pressure systems are shown to be more intense in one phase of the AO, NAO, NPO and PDO, whereas the IL is deeper in the opposite phase. The impacts driven by the AO are important and widespread across the Arctic Ocean, whereas the NAO/AMO and NPO/PDO mostly display significant effects in the North Atlantic Ocean and North Pacific Ocean, respectively. Having said that, the NAO does display an intense dynamic influence in the Beaufort Sea, Chukchi Sea, East Siberian Sea and Laptev Sea due to its associated SP patterns over the Arctic Ocean. The causal links between the NAO/AMO, NPO/PDO and the North Pacific Ocean, North Atlantic Ocean patterns, respectively, remain challenging to unveil. Nevertheless, further examination of the possible existence of teleconnections relating these patterns could prove such MOVs-driven causal relationships. It is important to recall that only the most impacted regions for the respective MOV are highlighted in this study. Nonetheless, significant results are found in the spatio-temporal analysis for the other regions, although links with the various MOVs are more complicated to assert owing to the relatively small regional impacts. Finally, a quantification of the percentage of the RSIV variability induced by the MOVs is not provided in this thesis, but could be investigated in future studies with, for example, the employment of EOF methods.

References

Appenzeller, C., Schwander, J., Sommer, S., and Stocker, T. (1998). The north atlantic oscillation and its imprint on precipitation and ice accumulation in greenland. *Geophysical Research Letters*, 25(11):1939–1942.

Ballinger, T. J., Hanna, E., Hall, R. J., Miller, J., Ribergaard, M. H., and Høyer, J. L. (2018). Greenland coastal air temperatures linked to baffin bay and greenland sea ice conditions during autumn through regional blocking patterns. *Climate Dynamics*, 50(1):83–100.

Boyin Huang, Peter W. Thorne, V. F. B. T. B. G. C. J. H. L. M. J. M. T. M. S. R. S. V. and Zhang, H.-M. (2017). Noaa extended reconstructed sea surface temperature (ersst), version 5. https://www.ncei.noaa.gov/access/metadata/landing-page/bin/iso?id=gov.noaa.ncdc:C00927.

Castruccio, F. S., Ruprich-Robert, Y., Yeager, S. G., Danabasoglu, G., Msadek, R., and Delworth, T. L. (2019). Modulation of arctic sea ice loss by atmospheric teleconnections from atlantic multidecadal variability. *Journal of Climate*, 32(5):1419–1441.

Copernicus (2020a). Sea ice concentration daily gridded data from 1979 to present derived from satellite observations. https://cds.climate.copernicus.eu/cdsapp#!/dataset/satellite-sea-ice-concentration?tab=overview.

Copernicus (2020b). Sea ice thickness monthly gridded data for the arctic from 2002 to present derived from satellite observations. https://cds.climate.copernicus.eu/cdsapp#!/dataset/satellite-sea-ice-thickness?tab=overview.

Dawson, A. (2016). eofs: A library for eof analysis of meteorological, oceanographic, and climate data. *Journal of Open Research Software*, 4(1).

Delworth, T. L. and Zeng, F. (2016). The impact of the north atlantic oscillation on climate through its influence on the atlantic meridional overturning circulation. *Journal of Climate*, 29(3):941–962.

Deser, Clara, T. K. and NCARS (2016). The climate data guide: Pacific decadal oscillation (pdo): Definition and indices. https://climatedataguide.ucar.edu/climate-data/pacific-decadal-oscillation-pdo-definition-and-indices.

Dickson, R., Osborn, T., Hurrell, J., Meincke, J., Blindheim, J., Adlandsvik, B., Vinje, T., Alekseev, G., and Maslowski, W. (2000). The arctic ocean response to the north atlantic oscillation. *Journal of Climate*, 13(15):2671–2696.

Ding, Q., Schweiger, A., L'Heureux, M., Steig, E. J., Battisti, D. S., Johnson, N. C., Blanchard-Wrigglesworth, E., Po-Chedley, S., Zhang, Q., Harnos, K., et al. (2019). Fingerprints of internal drivers of arctic sea ice loss in observations and model simulations. *Nature Geoscience*, 12(1):28–33.

ECMWF (2016). Era-20c. https://www.ecmwf.int/en/forecasts/datasets/reanalysis-datasets/era-20c.

ECMWF (2018a). Parameter details: 2-m temperature. https://apps.ecmwf.int/codes/grib/param-db/?id=167.

ECMWF (2018b). Parameter details: sea surface temperature. https://apps.ecmwf.int/codes/grib/param-db/?id=34.

ECMWF (2018c). Parameter details: surface pressure. https://apps.ecmwf.int/codes/grib/param-db/?id=134.

ECMWF (2018d). Parameter details: u-10m wind component. https://apps.ecmwf.int/codes/grib/param-db/?id=165.

ECMWF (2018e). Parameter details: v-10m wind component. https://apps.ecmwf.int/codes/grib/param-db/?id=166.

ECMWF (2018f). Parameter details: vertical integral of divergence of thermal heat flux. https://apps.ecmwf.int/codes/grib/param-db/?id=162083.

ECMWF (2019). Parameter details: instanteneous surface sensible heat flux. https://apps.ecmwf.int/codes/grib/param-db/?id=231.

Enfield, D.B., A. M.-N. and Trimble, P. (2001). Amo (atlantic multidecadal oscillation) index. https://psl.noaa.gov/data/timeseries/AMO/.

Enfield, D. B., Mestas-Nuñez, A. M., and Trimble, P. J. (2001). The atlantic multidecadal oscillation and its relation to rainfall and river flows in the continental us. *Geophysical Research Letters*, 28(10):2077–2080.

François, M. (2021). Forecast, prediction and projection in climate science. Unpublished. Chapter 2: Predictability 2: sources and mechanisms.

Goosse, H., Arzel, O., Bitz, C. M., de Montety, A., and Vancoppenolle, M. (2009). Increased variability of the arctic summer ice extent in a warmer climate. *Geophysical Research Letters*, 36(23).

Goosse, H., Kay, J. E., Armour, K. C., Bodas-Salcedo, A., Chepfer, H., Docquier, D., Jonko, A., Kushner, P. J., Lecomte, O., Massonnet, F., et al. (2018). Quantifying climate feedbacks in polar regions. *Nature communications*, 9(1):1–13.

Hamouda, M. E., Pasquero, C., and Tziperman, E. (2021). Decoupling of the arctic oscillation and north atlantic oscillation in a warmer climate. *Nature Climate Change*, 11(2):137–142.

Henley, B. J., Gergis, J., Karoly, D. J., Power, S., Kennedy, J., and Folland, C. K. (2015). A tripole index for the interdecadal pacific oscillation. *Climate Dynamics*, 45(11):3077–3090.

Henley, B.J., G. J.-K. D. P. S. K. J. F. C. (2015). Tpi (ipo) tripole index for the interdecadal pacific oscillation. https://psl.noaa.gov/data/timeseries/IPOTPI/.

Hurrell, J. and NCARS (2022). The climate data guide: North pacific (np) index by trenberth and hurrell; monthly and winter. https://climatedataguide.ucar.edu/climate-data/north-pacific-np-index-trenberth-and-hurrell-monthly-and-winter.

Hurrell, J. W. and Loon, H. V. (1997). Decadal variations in climate associated with the north atlantic oscillation. pages 69–94.

Kim, B.-M., Son, S.-W., Min, S.-K., Jeong, J.-H., Kim, S.-J., Zhang, X., Shim, T., and Yoon, J.-H. (2014). Weakening of the stratospheric polar vortex by arctic sea-ice loss. *Nature communications*, 5(1):1–8.

Kretschmer, M., Coumou, D., Donges, J. F., and Runge, J. (2016). Using causal effect networks to analyze different arctic drivers of midlatitude winter circulation. *Journal of climate*, 29(11):4069–4081.

Kug, J.-S., Jeong, J.-H., Jang, Y.-S., Kim, B.-M., Folland, C. K., Min, S.-K., and Son, S.-W. (2015). Two distinct influences of arctic warming on cold winters over north america and east asia. *Nature Geoscience*, 8(10):759–762.

Kwok, R. (2005). Variability of nares strait ice flux. *Geophysical Research Letters*, 32(24).

Limoges, A., Weckström, K., Ribeiro, S., Georgiadis, E., Hansen, K. E., Martinez, P., Seidenkrantz, M.-S., Giraudeau, J., Crosta, X., and Massé, G. (2020). Learning from the past: Impact of the arctic oscillation on sea ice and marine productivity off northwest greenland over the last 9,000 years. *Global change biology*, 26(12):6767–6786.

Lindsay, R. (2010). New unified sea ice thickness climate data record. *Eos, Transactions American Geophysical Union*, 91(44):405–406.

Linkin, M. E. and Nigam, S. (2008). The north pacific oscillation–west pacific teleconnection pattern: Mature-phase structure and winter impacts. *Journal of Climate*, 21(9):1979–1997.

Mahajan, S., Zhang, R., and Delworth, T. L. (2011). Impact of the atlantic meridional overturning circulation (amoc) on arctic surface air temperature and sea ice variability. *Journal of Climate*, 24(24):6573–6581.

Mantua, N. (2017). The pacific decadal oscillation (pdo). http://research.jisao.washington.edu/pdo/.

Meredith, M., Sommerkorn, M., Cassotta, S., Derksen, C., Ekaykin, A., Hollowed, A., Kofinas, G., Mackintosh, A., Melbourne-Thomas, J., Muelbert, M., et al. (2019). Polar regions. chapter 3, ipcc special report on the ocean and cryosphere in a changing climate.

Millero, F. (1978). Freezing point of sea water. *eighth report of the Joint Panel of Oceanographic Tables and Standards, appendix*, 6:29–31.

Morales, M., Miguel, A., Fichefet, T., and Holland, D. (1997). Physics and climatology of sea ice. *Unpublished*.

Mysak, L. A. and Manak, D. K. (1989). Arctic sea-ice extent and anomalies, 1953–1984. *Atmosphere-Ocean*, 27(2):376–405.

NCEI (2022a). North atlantic oscillation (nao). https://www.ncei.noaa.gov/access/monitoring/nao/.

NCEI (2022b). Pacific decadal oscillation (pdo). https://www.ncdc.noaa.gov/teleconnections/pdo/.

Newman, M., Alexander, M. A., Ault, T. R., Cobb, K. M., Deser, C., Di Lorenzo, E., Mantua, N. J., Miller, A. J., Minobe, S., Nakamura, H., et al. (2016). The pacific decadal oscillation, revisited. *Journal of Climate*, 29(12):4399–4427.

NSIDC (2020). All about sea ice. https://rb.gy/8habgp.

NSIDC (2022). Masie: Multisensor analyzed sea ice extent - northern hemisphere (masie-nh). https://nsidc.org/data/masie/browse_regions.

NWS (2022). Arctic oscillation (ao). https://www.cpc.ncep.noaa.gov/products/precip/CWlink/daily_ao_index/ao.shtml#publication.

of Canada, G. (2013). Sea ice: types and forms. http://tiny.cc/4vuruz.

Overland, J., Dunlea, E., Box, J. E., Corell, R., Forsius, M., Kattsov, V., Olsen, M. S., Pawlak, J., Reiersen, L.-O., and Wang, M. (2019). The urgency of arctic change. *Polar Science*, 21:6–13.

Park, H.-J. and Ahn, J.-B. (2016). Combined effect of the arctic oscillation and the western pacific pattern on east asia winter temperature. *Climate Dynamics*, 46(9):3205–3221.

Parkinson, C. L. (1990). The impact of the siberian high and aleutian low on the sea-ice cover of the sea of okhotsk. *Annals of Glaciology*, 14:226–229.

Poli, P., Hersbach, H., Dee, D. P., Berrisford, P., Simmons, A. J., Vitart, F., Laloyaux, P., Tan, D. G., Peubey, C., Thépaut, J.-N., et al. (2016). Era-20c: An atmospheric reanalysis of the twentieth century. *Journal of Climate*, 29(11):4083–4097.

Predybaylo, E. (2020). Python wavelet software. http://atoc.colorado.edu/research/wavelets/. Based on Torrence and Compo (1998).

PSC (2019). Piomas-20c sea ice thickness reconstruction. http://psc.apl.uw.edu/research/projects/piomas-20c/.

PSL (2022a). 20cr climate indices:np. https://psl.noaa.gov/data/20thC_Rean/timeseries/monthly/NP/.

PSL (2022b). Kaplan sst v2 data. https://psl.noaa.gov/data/gridded/data.kaplan_sst.html.

PSL (2022c). Noaa-cires twentieth century reanalysis (v2c): Summary. https://psl.noaa.gov/data/gridded/data.20thC_ReanV2c.html.

PyCWT (2022). Pycwt: spectral analysis using wavelets in python. https://pycwt.readthedocs.io/en/latest/.

Rahmstorf, S., Crucifix, M., Ganopolski, A., Goosse, H., Kamenkovich, I., Knutti, R., Lohmann, G., Marsh, R., Mysak, L. A., Wang, Z., et al. (2005). Thermohaline circulation hysteresis: A model intercomparison. *Geophysical Research Letters*, 32(23).

Rebecca, L. (2009). Climate variability: Arctic oscillation. https://www.climate.gov/news-features/understanding-climate/climate-variability-arctic-oscillation.

Rebecca Lindsey, L. D. (2009). Climate variability: North atlantic oscillation. https://www.climate.gov/news-features/understanding-climate/climate-variability-north-atlantic-oscillation.

Reconstruction, P.-C. S. I. T. (2019). Piomas-20c sea ice thickness reconstruction. https://psc.apl.uw.edu/research/projects/piomas-20c/.

Rigor, I. G., Wallace, J. M., and Colony, R. L. (2002). Response of sea ice to the arctic oscillation. *Journal of Climate*, 15(18):2648–2663.

Schweiger, A. J., Wood, K. R., and Zhang, J. (2019). Arctic sea ice volume variability over 1901–2010: A model-based reconstruction. *Journal of Climate*, 32(15):4731–4752.

Scipy (2022). scipy.stats.pearsonr. https://docs.scipy.org/doc/scipy/reference/generated/scipy.stats.pearsonr.html.

Screen, J. A. and Francis, J. A. (2016). Contribution of sea-ice loss to arctic amplification is regulated by pacific ocean decadal variability. *Nature Climate Change*, 6(9):856–860.

Titchner, H. A. and Rayner, N. A. (2014). The met office hadley centre sea ice and sea surface temperature data set, version 2: 1. sea ice concentrations. *Journal of Geophysical Research: Atmospheres*, 119(6):2864–2889.

Torrence, C. and Compo, G. P. (1998). A practical guide to wavelet analysis. *Bulletin of the American Meteorological society*, 79(1):61–78.

Trenberth, K., Zhang, R., and NCARS (2021). The climate data guide: Atlantic multi-decadal oscillation (amo). https://climatedataguide.ucar.edu/climate-data/atlantic-multi-decadal-oscillation-amo.

Van Achter, G., Ponsoni, L., Massonnet, F., Fichefet, T., and Legat, V. (2020). Brief communication: Arctic sea ice thickness internal variability and its changes under historical and anthropogenic forcing. *The Cryosphere*, 14(10):3479–3486.

Vancoppenolle, M., Fichefet, T., Goosse, H., Bouillon, S., Madec, G., and Maqueda, M. A. M. (2009). Simulating the mass balance and salinity of arctic and antarctic sea ice. 1. model description and validation. *Ocean Modelling*, 27(1-2):33–53.

Vomero, M., Kimura, N., Milz, M., Barabash, V., and Yamaguchi, H. (2021). Large-scale sea ice divergence and convergence monitoringin the arctic ocean during spring 2018. *Okhotsk Sea and Polar Oceans Research*, 5:31–35.

Wilks, D. S. (2011). *Statistical methods in the atmospheric sciences*, volume 100. Academic press.

Zhang, J., Lindsay, R., Schweiger, A., and Rigor, I. (2012). Recent changes in the dynamic properties of declining arctic sea ice: A model study. *Geophysical Research Letters*, 39(20).

Zhang, J. and Rothrock, D. A. (2003). Modeling global sea ice with a thickness and enthalpy distribution model in generalized curvilinear coordinates. *Monthly Weather Review*, 131(5):845–861.

Zhang, J., Thomas, D., Rothrock, D., Lindsay, R., Yu, Y., and Kwok, R. (2003). Assimilation of ice motion observations and comparisons with submarine ice thickness data. *Journal of Geophysical Research: Oceans*, 108(C6).

Zheng, Z., Ban, J., and Li, Y. (2021). The effect of the arctic oscillation on the predictability of mid-high latitude circulation in december. *Frontiers in Physics*, 9:553.

Appendix A

Supplementary materials

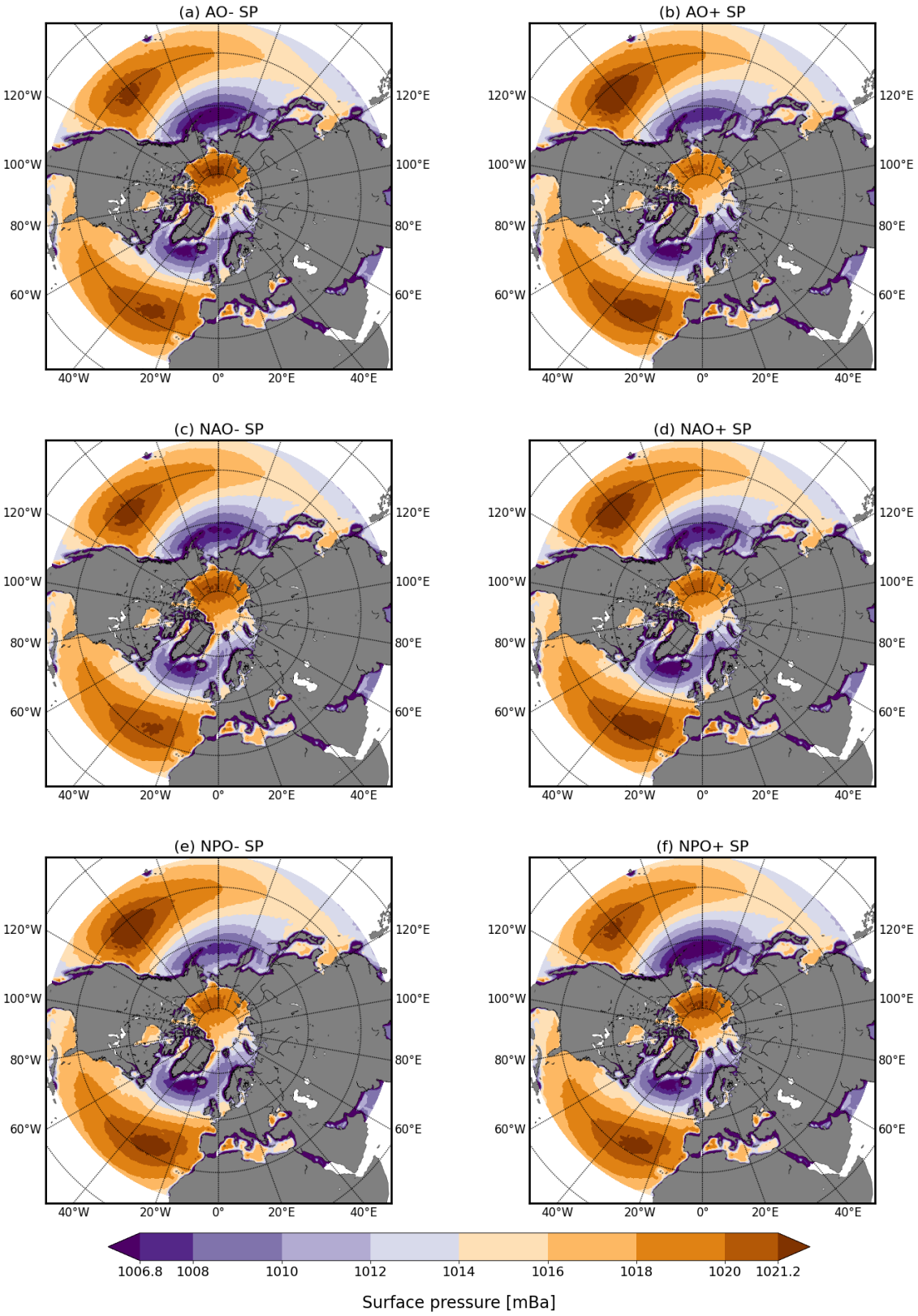


Fig. A.1 – Mean SP for the mid-1902 to mid-2009 period during (a) AO-, (b) AO+, (c) NAO-, (d) NAO+, (e) NPO-, and (f) NPO+. The SP dataset is provided by the ERA-20C reanalysis [Poli et al., 2016] and is detrended and smoothed using the methodology introduced in section 3.2.

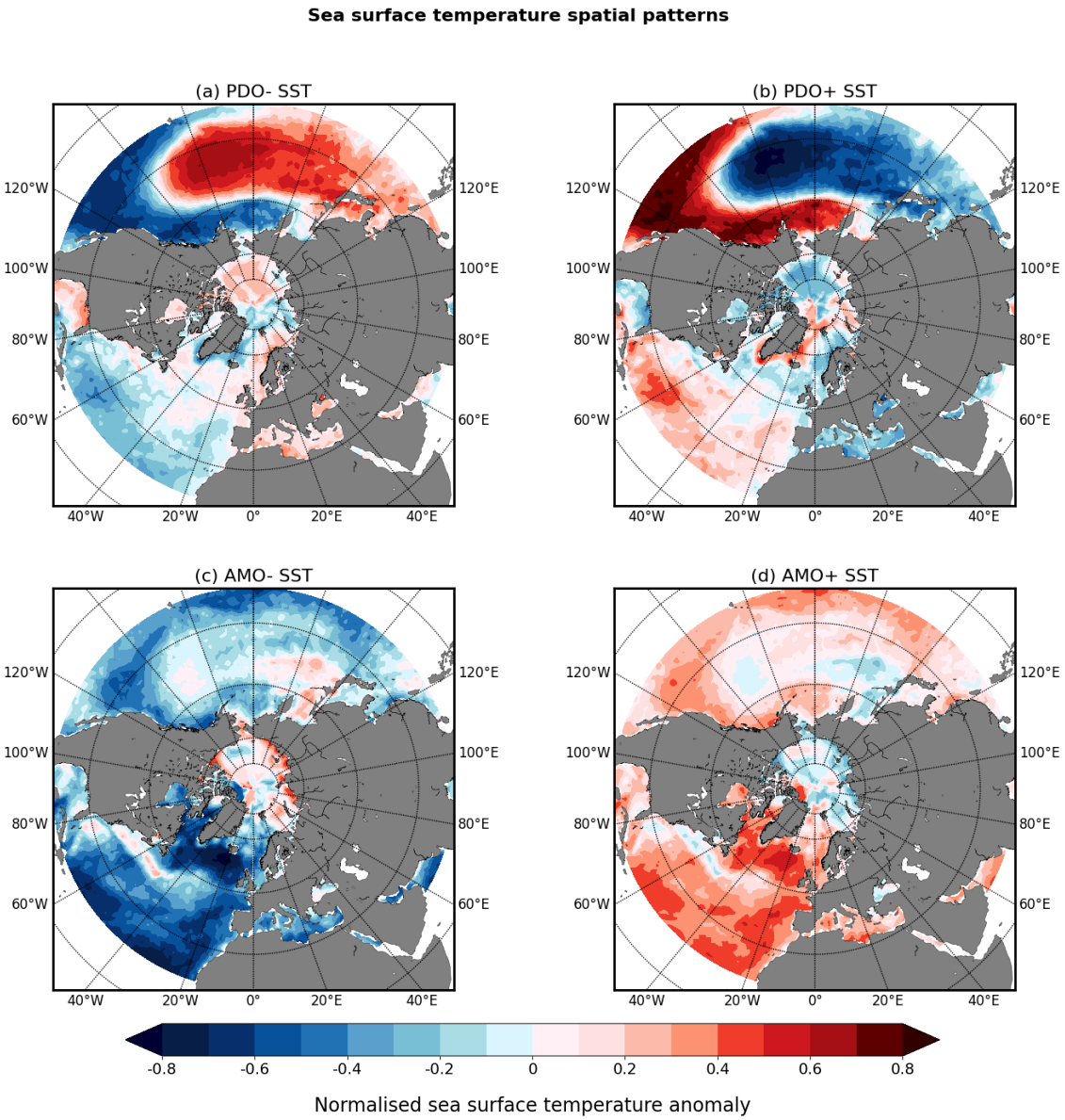


Fig. A.2 – Mean SST anomaly for the mid-1902 to mid-2009 period during (a) PDO-, (b) PDO+, (c) AMO-, and (d) AMO+. The SST dataset is provided by the HadISST2 analysis [Titchner and Rayner, 2014] and is detrended and smoothed using the methodology introduced in section 3.2.

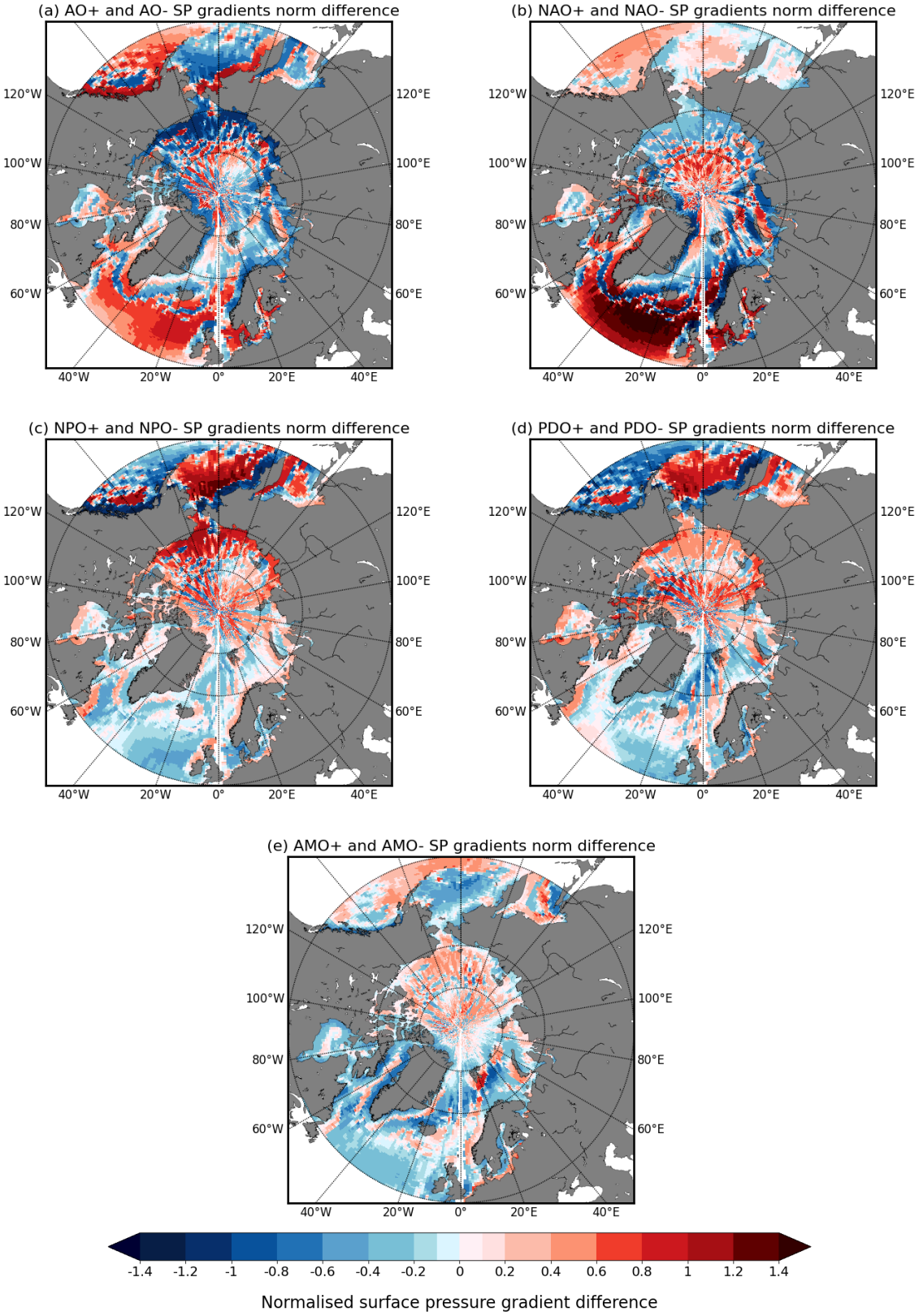


Fig. A.3 – Difference in the norm of the mean normalised SP gradients, from mid-1902 to mid-2009, between (a) AO+ and AO-, (b) NAO+ and NAO-, (c) NPO+ and NPO-, (d) PDO+ and PDO-, (e) AMO+ and AMO-. The SP gradients norm time series of all grid-cells employed are normalised by their own standard deviation as to represent the relative impacts.

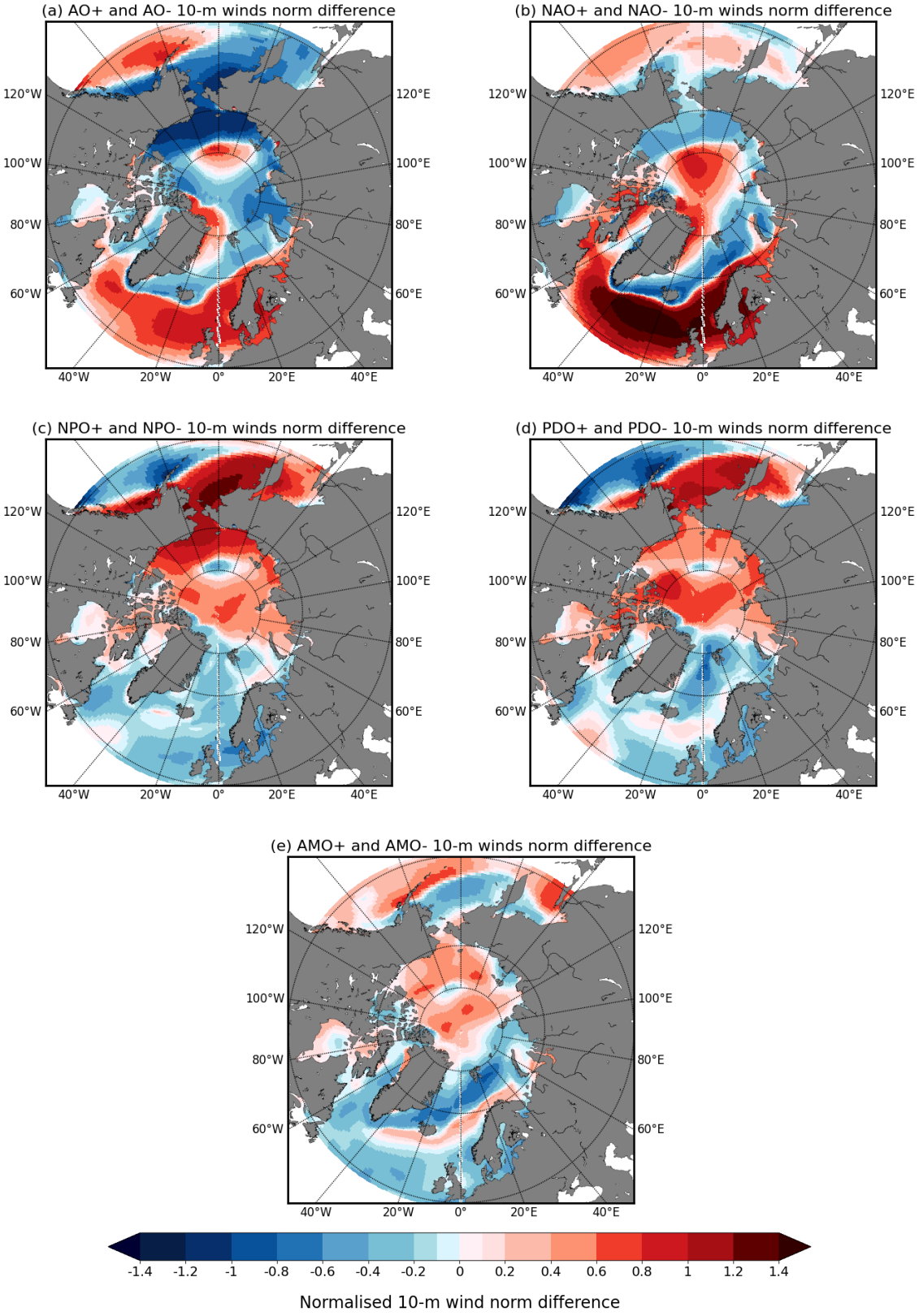


Fig. A.4 – Difference in the norm of the mean normalised ERA-20C 10-m winds, from mid-1902 to mid-2009, between (a) AO+ and AO-, (b) NAO+ and NAO-, (c) NPO+ and NPO-, (d) PDO+ and PDO-, (e) AMO+ and AMO-. The 10-m winds norm time series of all grid-cells employed are normalised by their own standard deviation as to represent the relative impacts.

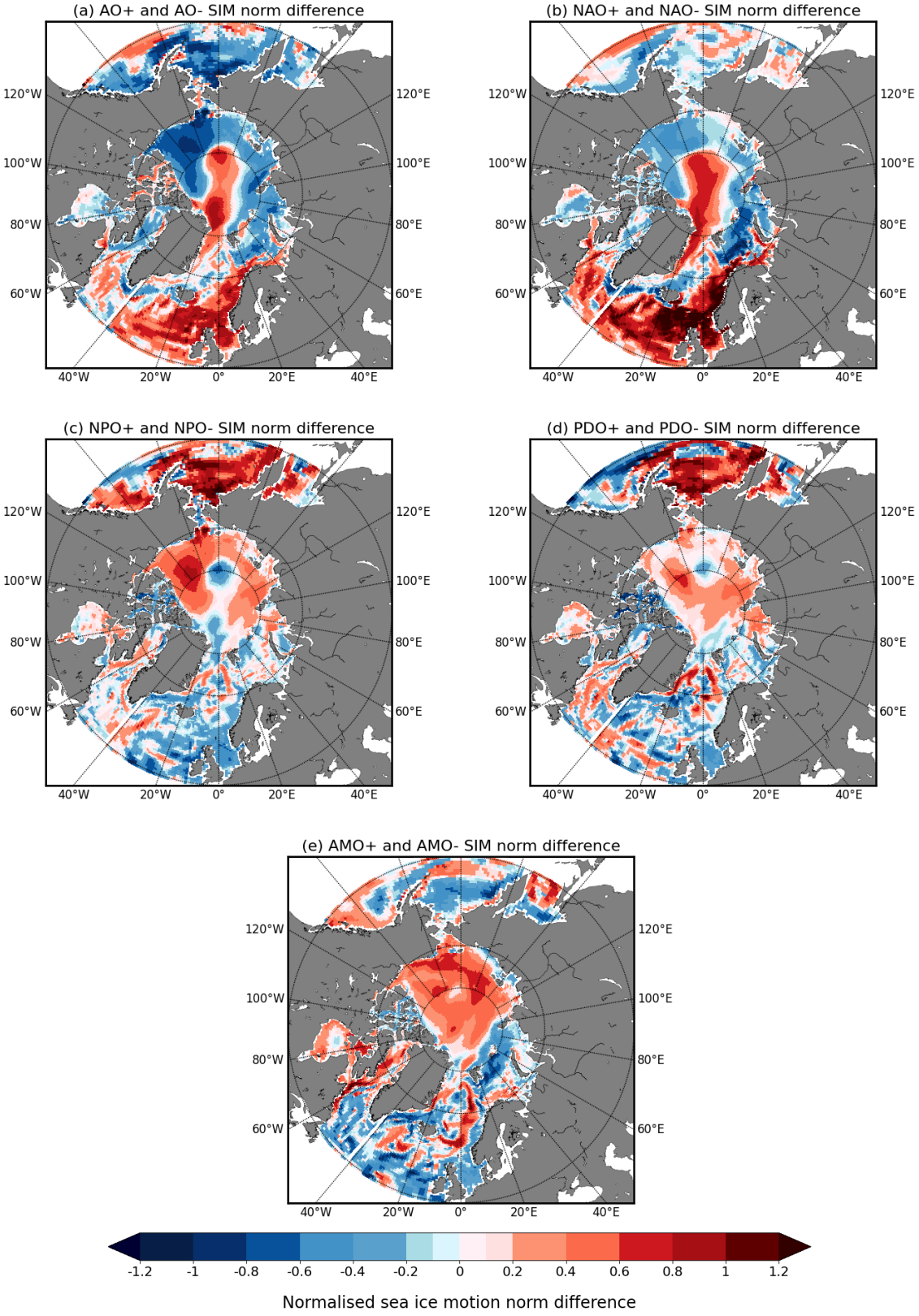


Fig. A.5 – Difference in the norm of the mean normalised PIOMAS-20C SIM, from mid-1902 to mid-2009, between (a) AO+ and AO-, (b) NAO+ and NAO-, (c) NPO+ and NPO-, (d) PDO+ and PDO-, (e) AMO+ and AMO-. The SIM norm time series of all grid-cells employed are normalised by their own standard deviation as to represent the relative impacts.

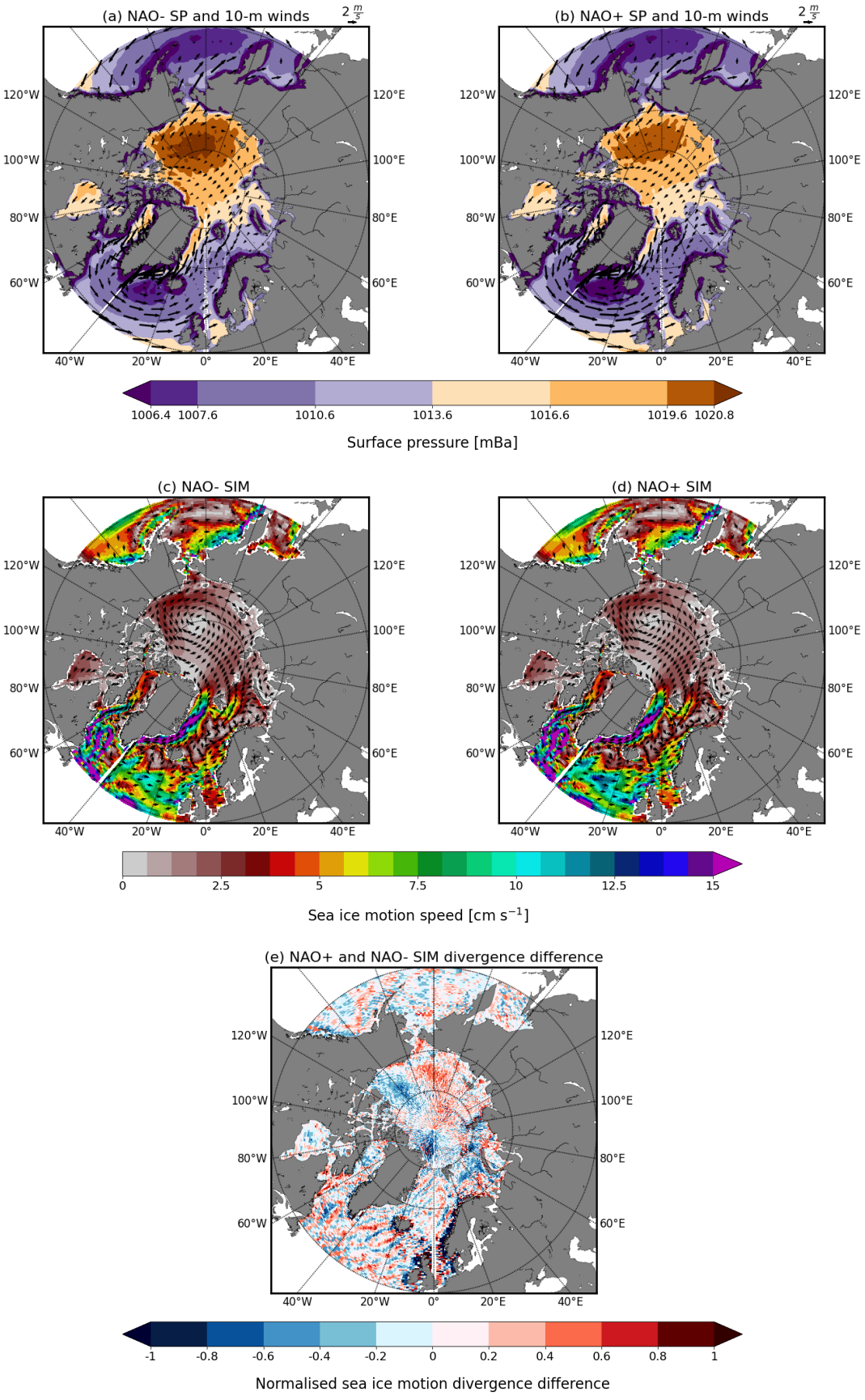


Fig. A.6 – Dynamic processes spatial patterns associated with the NAO spanning from mid-1902 to mid-2009. The ERA-20C mean SP and 10-m wind distributions during (a) NAO- and (b) NAO+. The PIOMAS-20C mean SIM distributions during (c) NAO- and (d) NAO+. (e) The difference in the mean of the computed normalised SIM divergence between NAO+ and NAO-. The SIM divergence time series of all grid-cells are normalised by their own standard deviation as to represent the relative impacts.

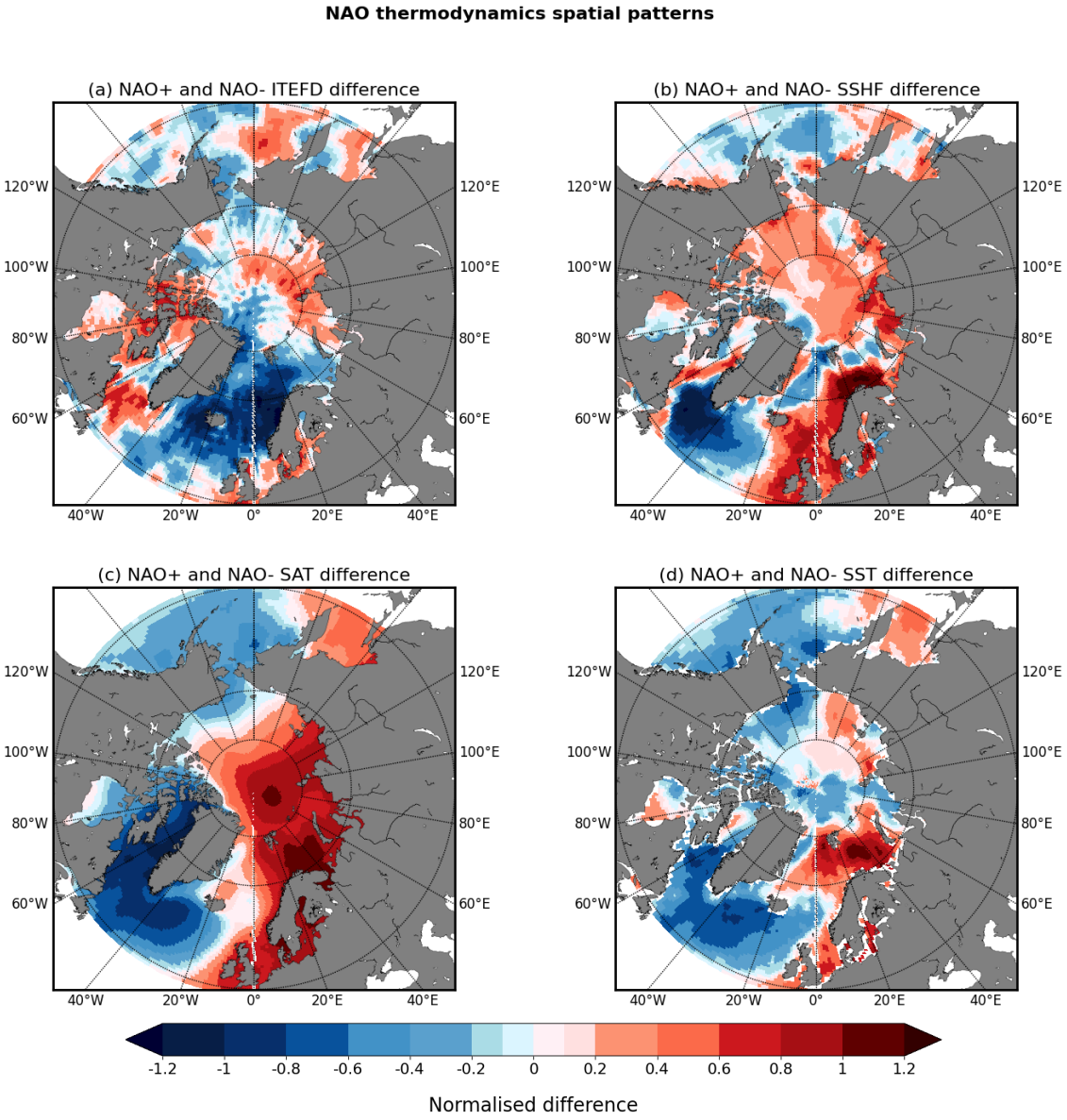


Fig. A.7 – Difference between NAO+ and NAO-, from mid-1902 to mid-2009, in the mean of the ERA-20C normalised (a) ITEFD, (b) SSHF, (c) SAT and (d) SST. The various time series of all grid-cells employed are normalised by their own standard deviation as to represent the relative impacts.

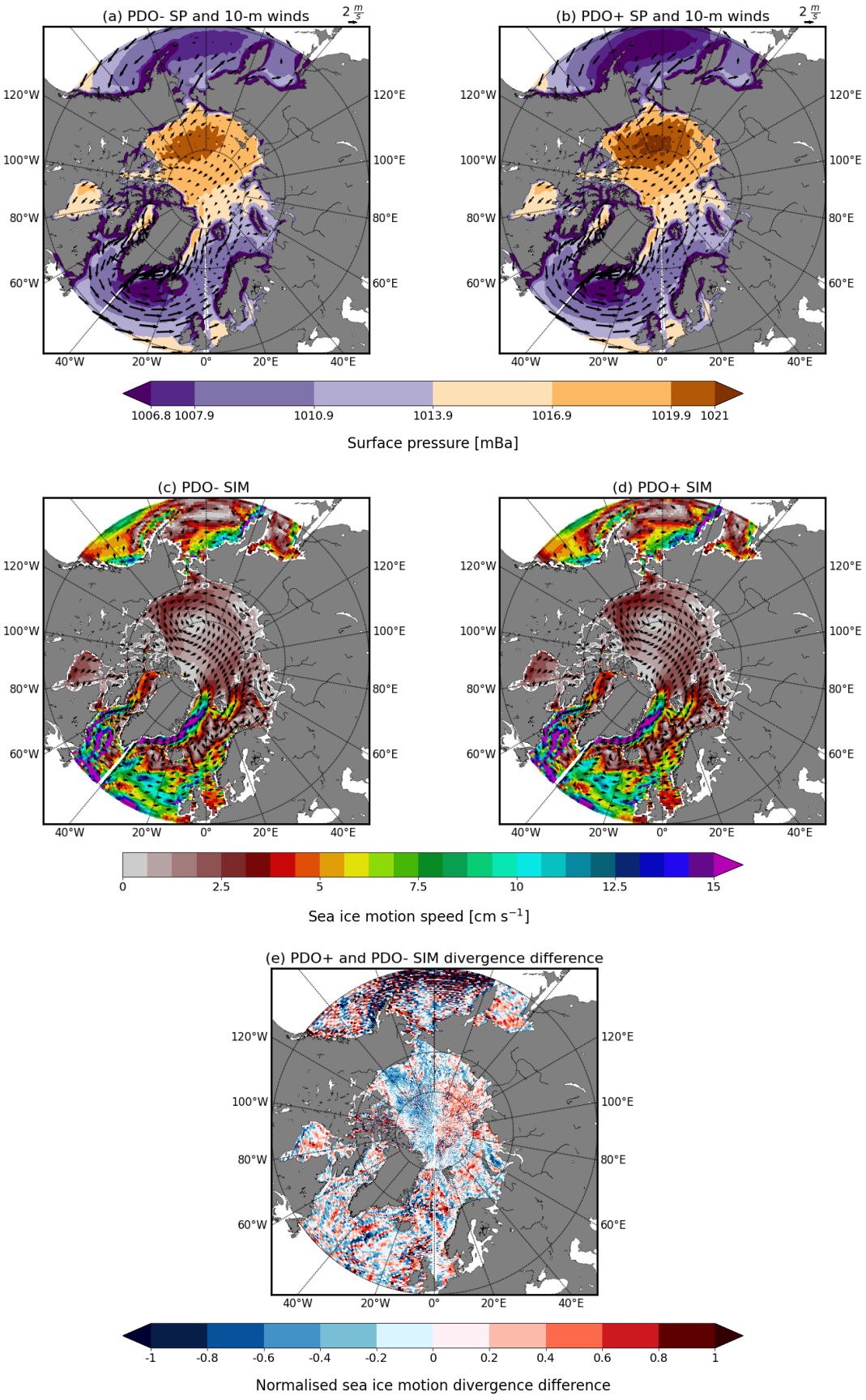


Fig. A.8 – Dynamic processes spatial patterns associated with the PDO spanning from mid-1902 to mid-2009. The ERA-20C mean SP and 10-m wind distributions during (a) PDO- and (b) PDO+. The PIOMAS-20C mean SIM distributions during (c) PDO- and (d) PDO+. (e) The difference in the mean of the computed normalised SIM divergence between AO+ and AO-. The SIM divergence time series of all grid-cells are normalised by their own standard deviation as to represent the relative impacts.

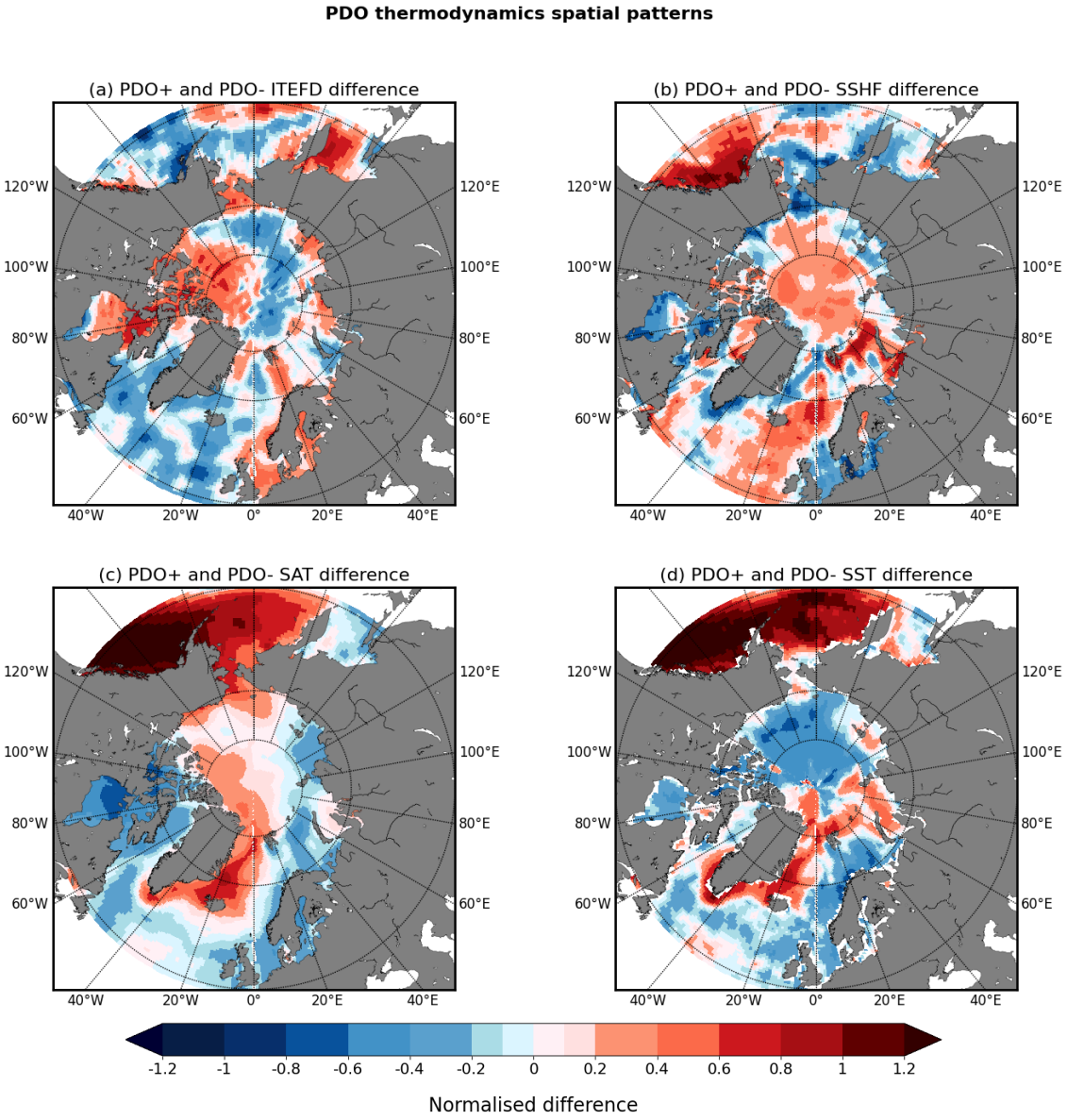
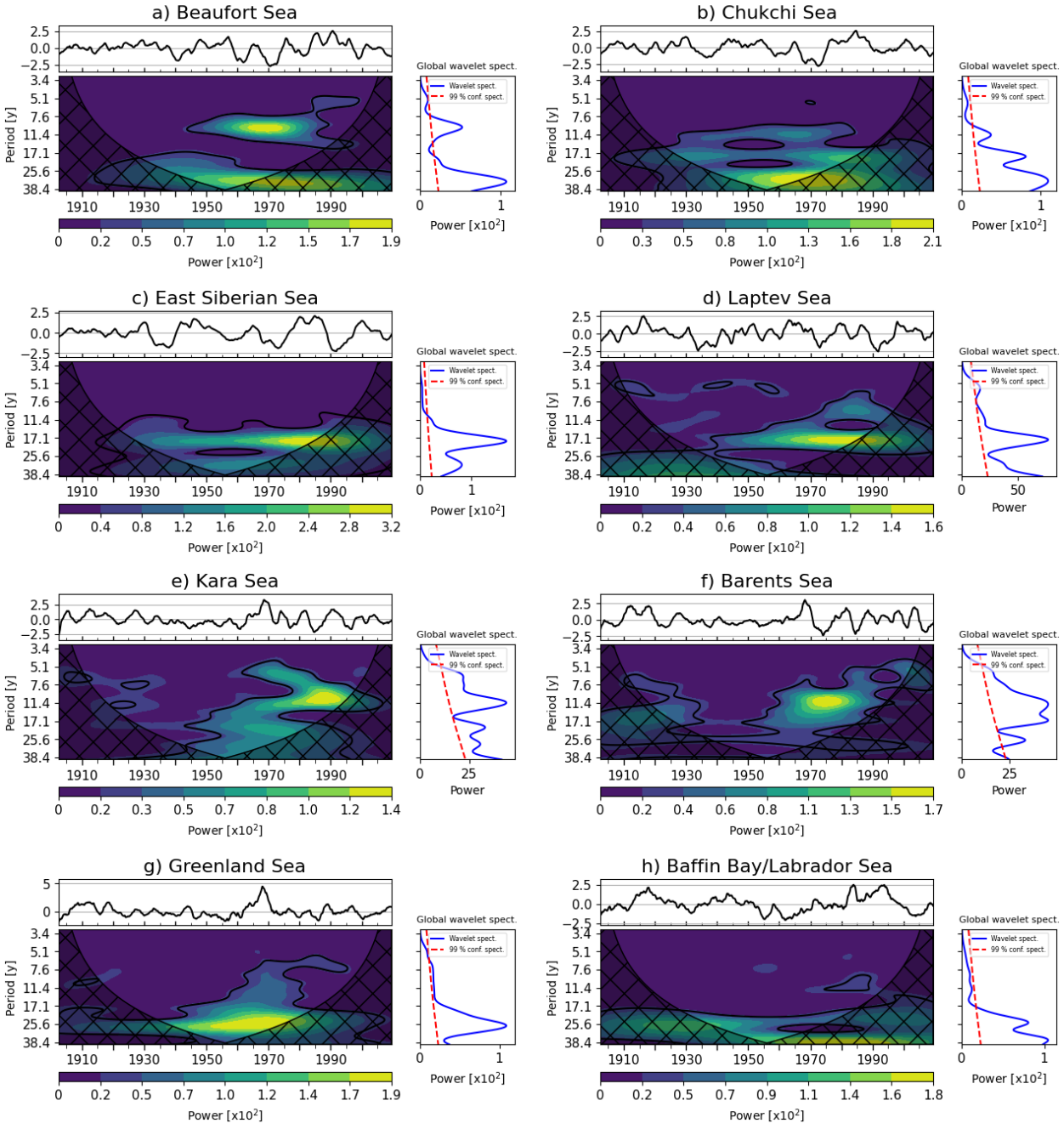


Fig. A.9 – Difference between PDO+ and PDO-, from mid-1902 to mid-2009, in the mean of the ERA-20C normalised (a) ITEFD, (b) SSHF, (c) SAT and (d) SST. The various time series of all grid-cells employed are normalised by their own standard deviation as to represent the relative impacts.

Regional sea ice volume index



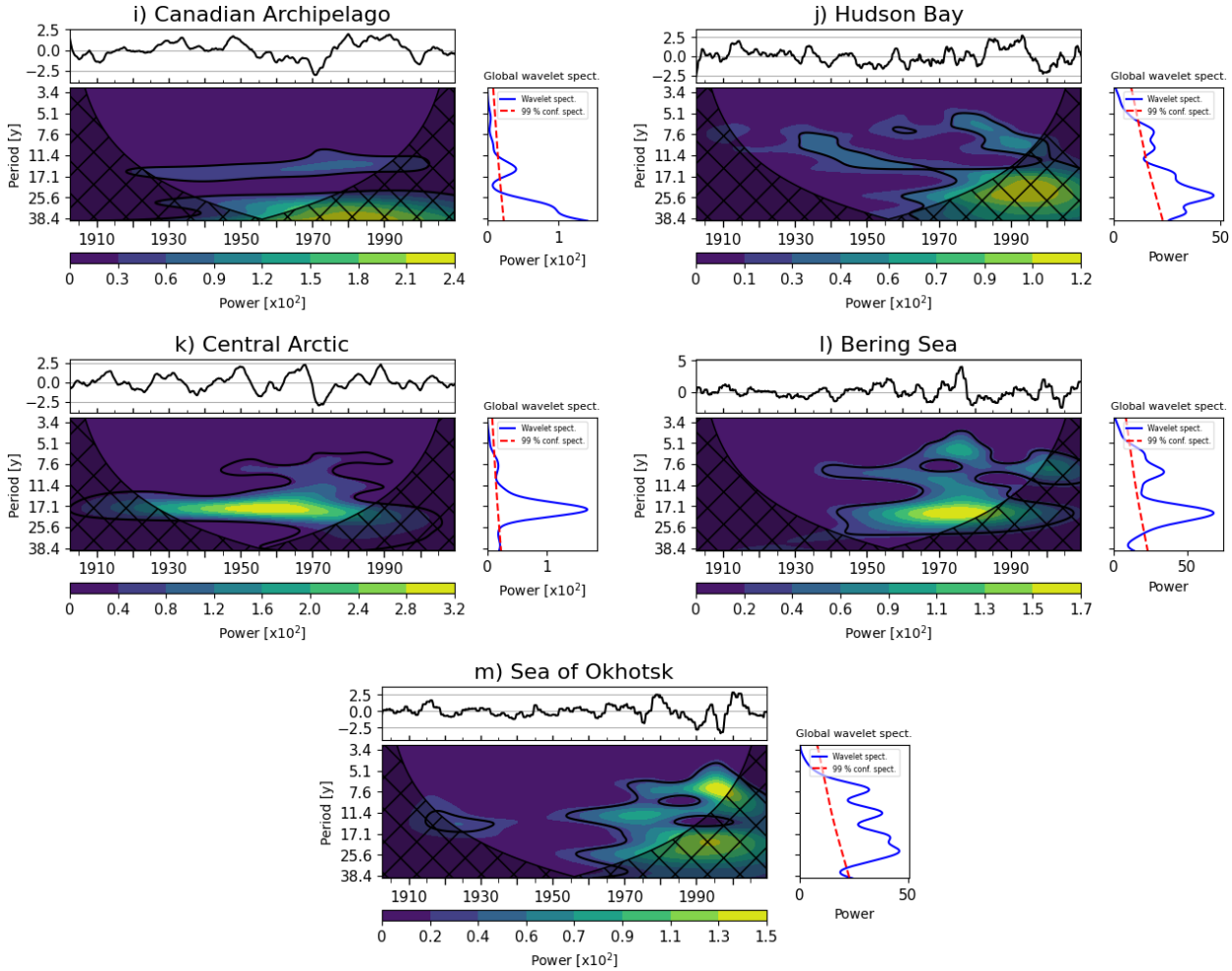
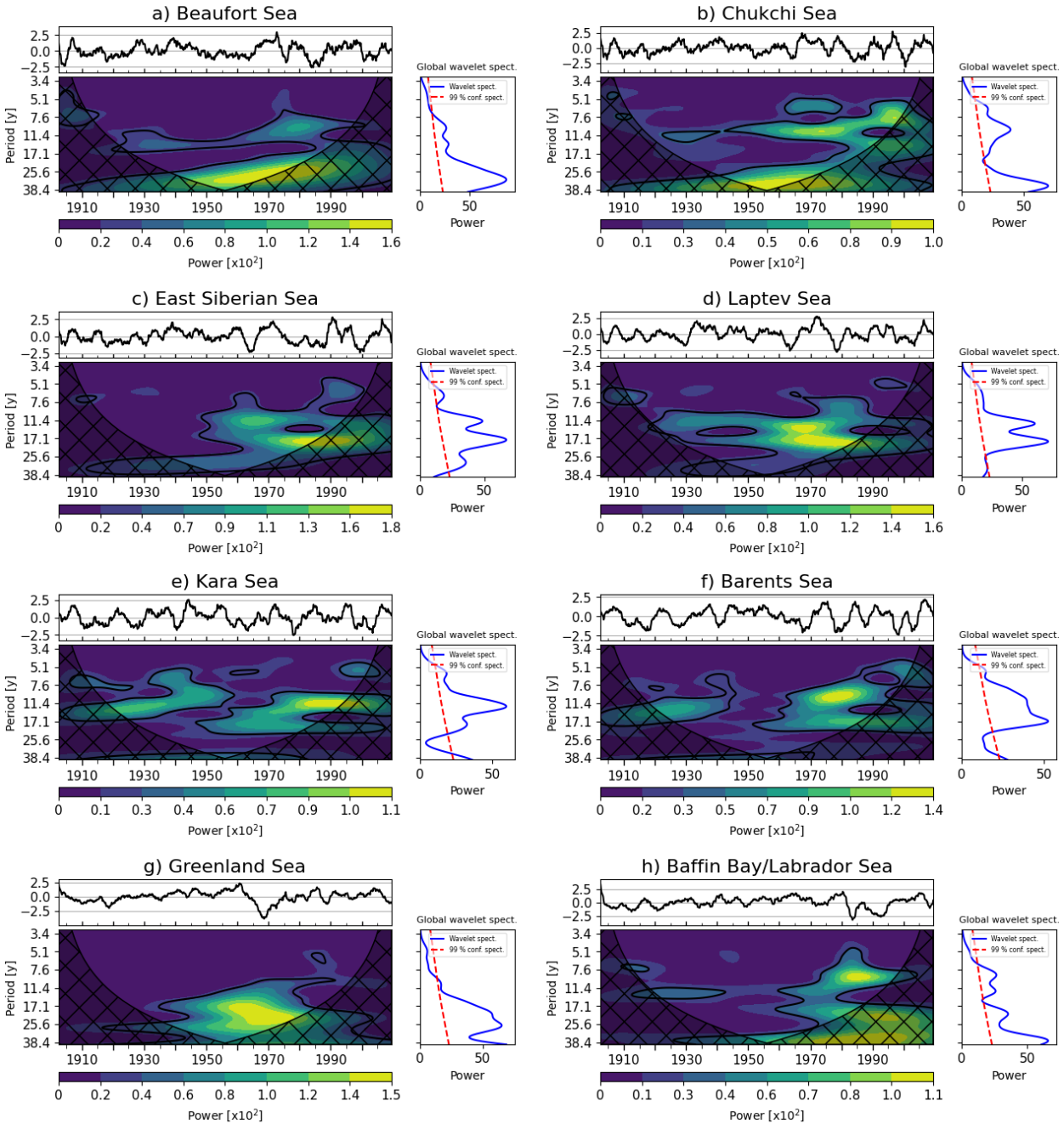


Fig. A.10 – Wavelet analysis spanning from mid-1902 to mid-2009 of the RSIV for each region. Top plot represents the index time series. Bottom plot represents the WPS of the time series. Bottom right plot represents the mean power spectrum. The thick black contours and red dashed lines represent the 99% significance level using a red noise background power spectrum, while the crosshatched areas represent the cone of influence where edge effects become important. The Morlet function was used for the wavelet analysis.

Regional surface air temperature index



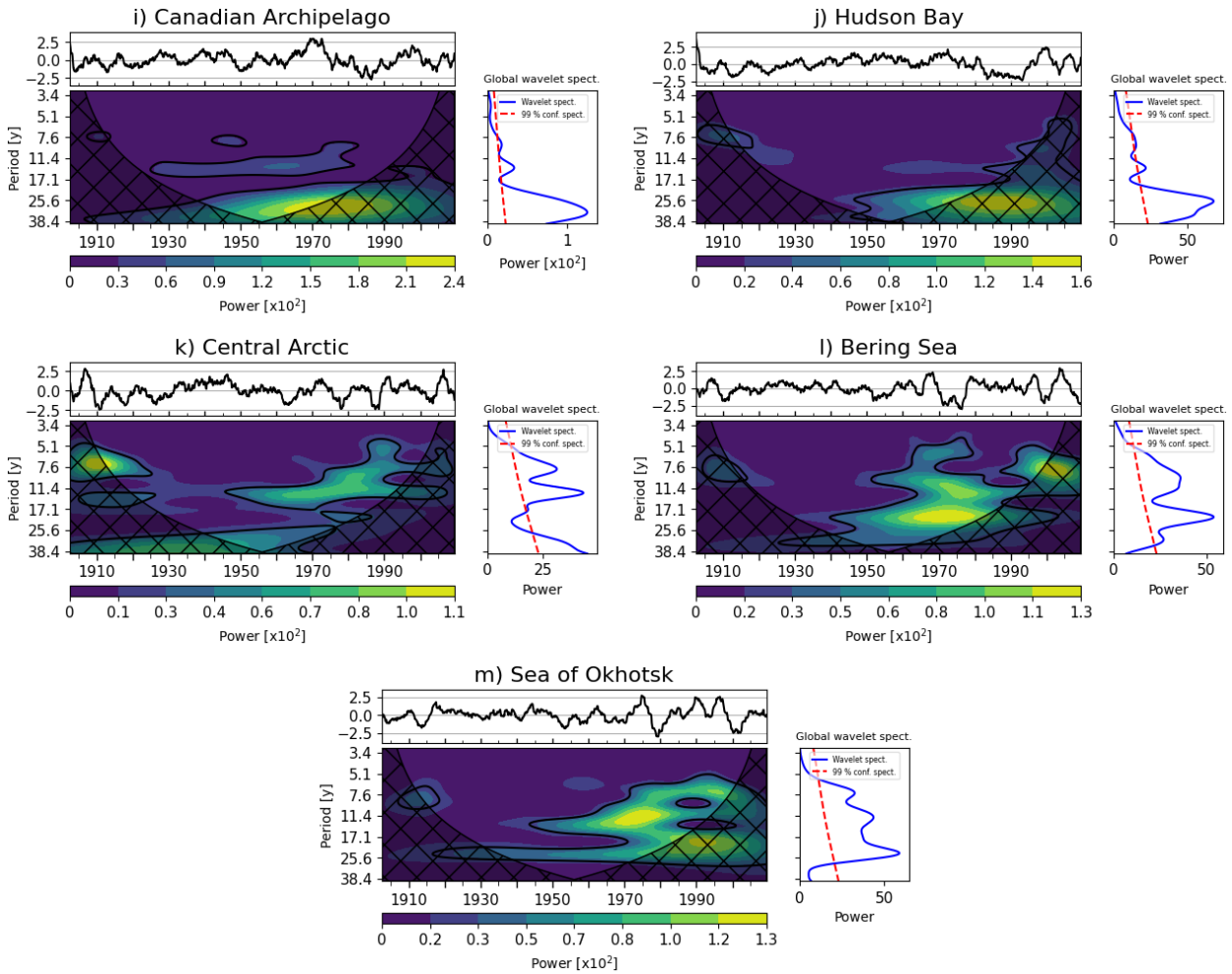
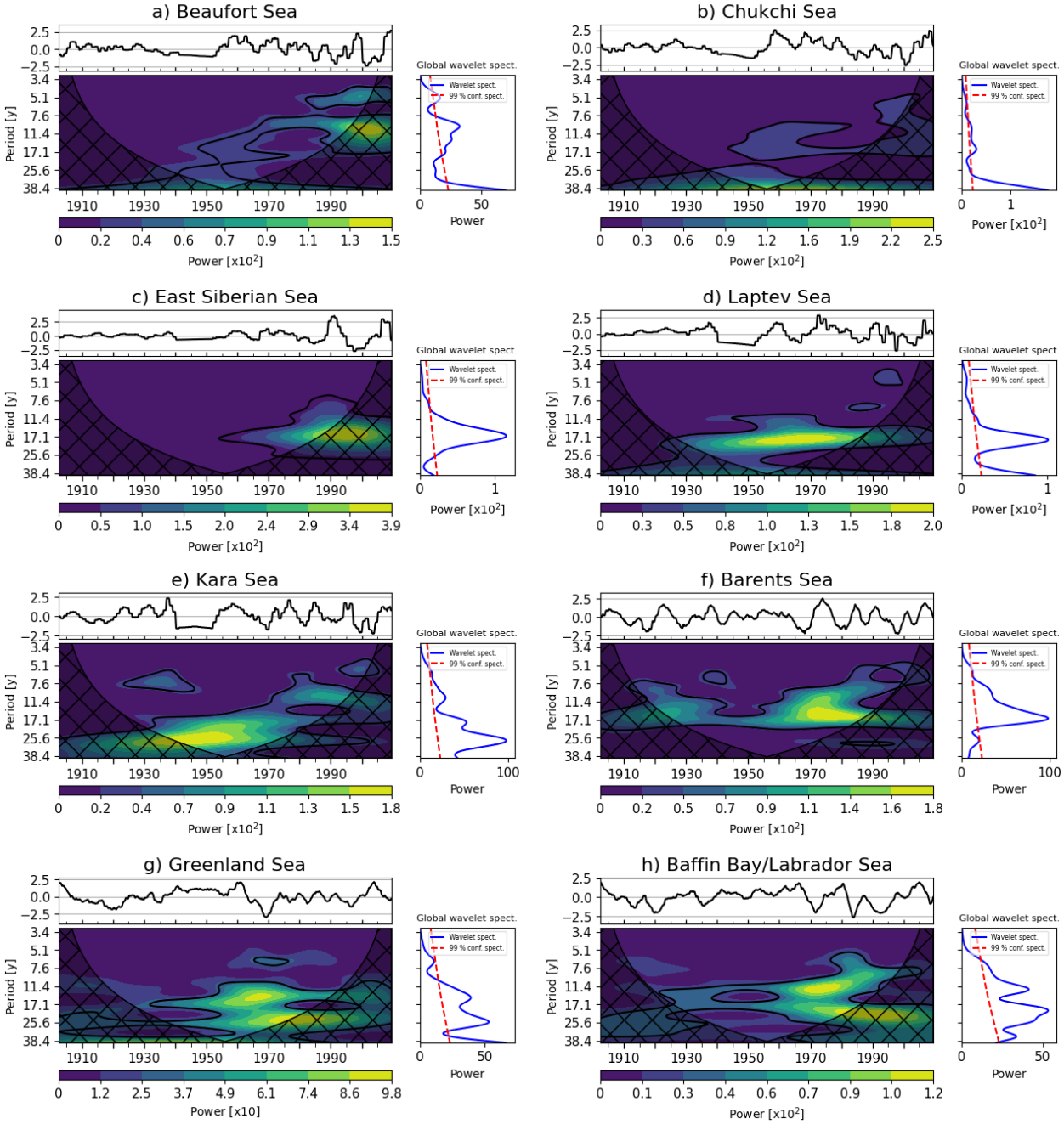


Fig. A.11 – Wavelet analysis spanning from mid-1902 to mid-2009 of the RSAT for each region. Top plot represents the index time series. Bottom plot represents the WPS of the time series. Bottom right plot represents the mean power spectrum. The thick black contours and red dashed lines represent the 99% significance level using a red noise background power spectrum, while the crosshatched areas represent the cone of influence where edge effects become important. The Morlet function was used for the wavelet analysis.

Regional sea surface temperature index



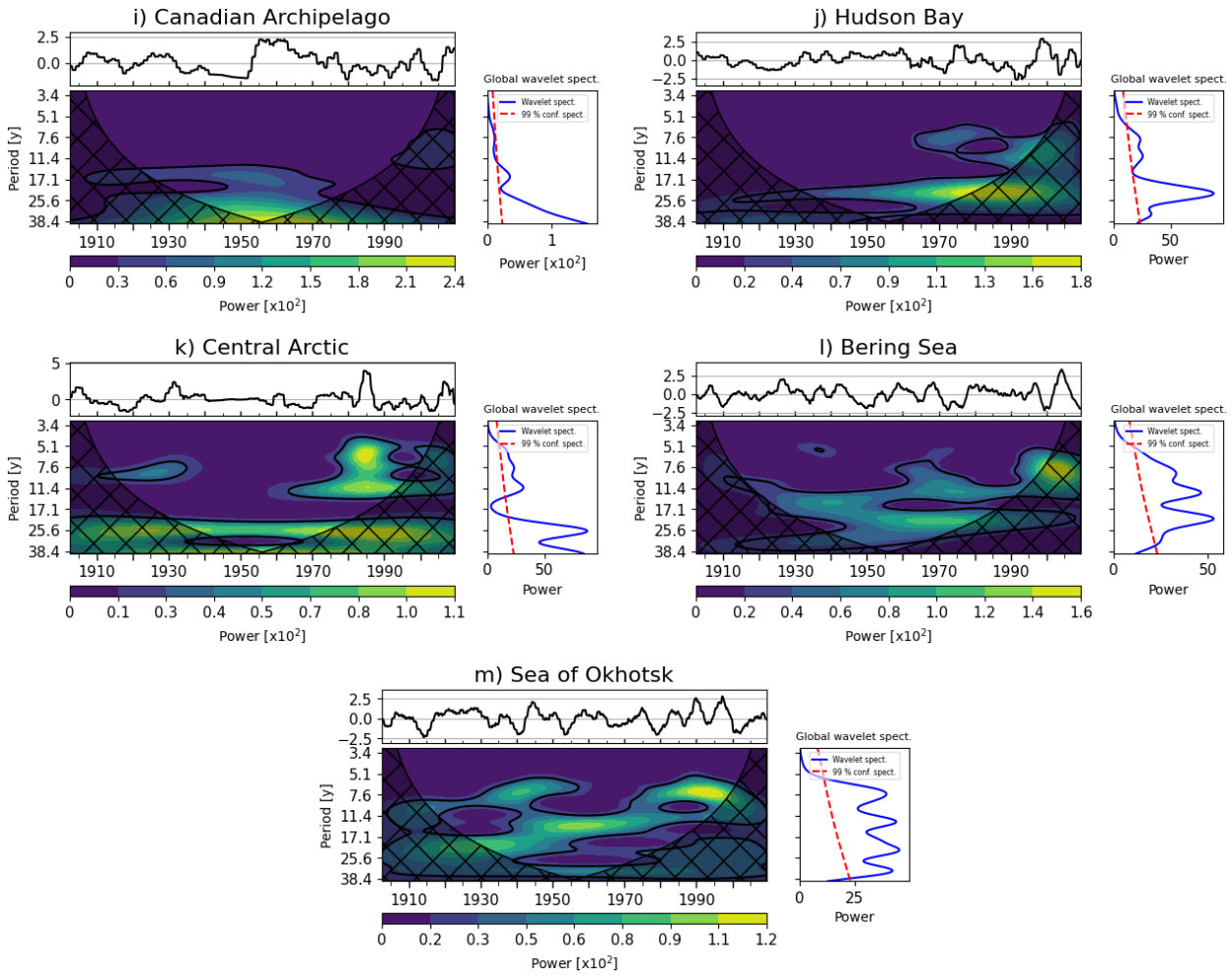


Fig. A.12 – Wavelet analysis spanning from mid-1902 to mid-2009 of the RSST for each region. Top plot represents the index time series. Bottom plot represents the WPS of the time series. Bottom right plot represents the mean power spectrum. The thick black contours and red dashed lines represent the 99% significance level using a red noise background power spectrum, while the crosshatched areas represent the cone of influence where edge effects become important. The Morlet function was used for the wavelet analysis.

Table A.1 – List of the full names of acronyms employed in this thesis.

Acronym	Full name
AO	Arctic Oscillation
NAO	North Atlantic Oscillation
NPO	North Pacific Oscillation
PDO	Pacific Decadal Oscillation
AMO	Atlantic Multidecadal Oscillation
SIV	Sea ice volume
RSIV	Regional sea ice volume
SIM	Sea ice motion
RSIM	Regional sea ice motion
SIT	Sea ice thickness
SIC	Sea ice concentration
SIA	Sea ice area
SIE	Sea ice extent
SAT	Surface air temperature
RSAT	Regional surface air temperature
SST	Sea surface temperature
RSST	Regional sea surface temperature
SSHF	Sensible surface heat flux
ITEFD	Integrated thermal energy flux divergence
MOV	Mode of variability
SLP	Sea level pressure
SP	Surface pressure
AO+	AO positive phase
AO-	AO negative phase
NAO+	NAO positive phase
NAO-	NAO negative phase
NPO+	NPO positive phase
NPO-	NPO negative phase
PDO+	PDO positive phase
PDO-	PDO negative phase
AMO+	AMO positive phase
AMO-	AMO negative phase
BH	Beaufort High
IL	Icelandic Low
AL	Aleutian Low
AH	Azores High
NPH	North Pacific High
TDS	Transpolar Drift Stream
EOF	Empirical orthogonal function
PC	Principal component
WPS	Wavelet power spectrum
WT	Wavelet transform
FPS	Fourier power spectrum

UNIVERSITÉ CATHOLIQUE DE LOUVAIN
Faculté des sciences
Place des Sciences, 2 bte L6.06.01, 1348 Louvain-la-Neuve, Belgique | www.uclouvain.be/sc